Aus dem Institut für Kardiovaskuläre Physiologie und Pathophysiologie
(im Walter-Brendel-Zentrum für Experimentelle Medizin, WBex)
der Ludwig-Maximilians-Universität München
Kommissarischer Direktor: Prof. Dr. med. Markus Sperandio
Ehemaliger Direktor: Prof. Dr. med. Ulrich Pohl

The non-muscle myosin heavy chain Myh9 is essential for neutrophil migration during acute inflammation

Dissertation

zum Erwerb des Doktorgrades der Naturwissenschaften
an der Medizinischen Fakultät der
Ludwig-Maximilians-Universität München

vorgelegt von

Annette Zehrer

aus München

Jahr

2019

Mit Genehmigung der Medizinischen Fakultät

der Universität München

Betreuer:	Prof. Dr. rer. nat. Barbara Walzog
Zweitgutachter (in):	Priv. Doz. Dr. Reinhard Obst
Dekan:	Prof. Dr. med. dent. Reinhard Hickel
Tag der mündlichen Prüfung:	20.02.2020

Table of content

I Abstract

During acute inflammation, polymorphonuclear neutrophils (PMN) are the first leukocytes to arrive at sites of injury. To maintain the polarised morphology during migration, molecules of the class II non-muscle myosins (NMII) are essential. In PMN, only one of the three in mammalian cells existing myosin heavy chains (Myh), namely Myh9, the heavy chain of NMIIA, is expressed. This study set out to unravel the functional impact of Myh9 on PMN trafficking *in vitro* and *in vivo* using genetic downregulation of Myh9 in mice.

Treatment of murine bone marrow-derived PMN with pn-blebbistatin, a pharmacological inhibitor of NMII activity, revealed a dose-dependent impairment of migration velocity under flow conditions, accompanied by a change in morphology as well as reduced transmigratory capacity *in vitro*. As the complete knock-out of *Myh9* in the hematopoietic system was lethal, *Vav-iCre*$^{+}$*/Myh9*$^{wt/fl}$ (*Myh9-cHet*) mice with a significant reduction of Myh9 expression in PMN were used in the following experiments. During *in vitro* migration under flow conditions in 2D environment, reduction of Myh9 expression in *Myh9-cHet* PMN significantly diminished migration velocity and Euclidean distance compared to *Vav-iCre*$^{-}$*/Myh9*$^{wt/fl}$ (*control)* PMN. Similarly, *in vitro* transmigration of *Myh9-cHet* PMN was reduced compared to *control* PMN. In addition, downregulation of Myh9 decreased PMN migration in confined 3D environment *in vitro*. Using STED nanoscopy, the underlying mechanisms causing the migration defect was evaluated and a dysregulation of F-actin dynamics upon Myh9 downregulation was discovered. In a model of acute peritonitis, reduced Myh9 expression in the hematopoietic system resulted in significantly diminished PMN recruitment *in vivo*. The induction of a sterile injury in the ear dermis of *Myh9-cHet* and *control* mice revealed a diminished extravasation as well as decreased interstitial migration velocity and Euclidean distance for PMN of *Myh9-cHet* mice compared to PMN of *control* mice. Three different models of bone marrow chimeric mice, namely wildtype mice carrying a wildtype hematopoietic system, wildtype mice carrying a *Myh9-cHet* hematopoietic system and wildtype mice carrying a hematopoietic system consisting of a 50:50 mixture of wildtype and *Myh9-cHet* cells, were generated. The induced peritonitis in these three models revealed a cell-intrinsic mechanism causing migration defects in PMN with reduced Myh9 expression. Next, Hoxb8-SCF cell-derived neutrophils were examined as a potential tool to study the molecular mechanism of PMN trafficking. *In vitro* assays comparing undifferentiated and differentiated Hoxb8-SCF cells with PMN demonstrated the typical segmentation of nuclei during differentiation towards PMN in Hoxb8-SCF cells, as well as the downregulation of progenitor markers and upregulation of PMN surface markers to similar levels found on

mature PMN. In functional *in vitro* assays reviewing integrin upregulation after stimulation, induction of adhesion as well as mechanotactic and chemotactic migration on 2D surfaces, Hoxb8-SCF cell-derived neutrophils demonstrated behaviour similar to murine bone marrow-derived PMN. Hoxb8-SCF cells were generated from *Vav-iCre*$^{+}$*/Myh9*$^{wt/fl}$, *Vav-iCre*$^{+}$*/Myh9*$^{fl/fl}$ and *Vav-iCre*$^{-}$*/Myh9*$^{fl/fl}$ fetal liver progenitor cells, and expression of Myh9-EGFP in Hoxb8-SCF cells with a Myh9 knock-down was able to rescue the Myh9-related migration defects in 2D and 3D environment. Live cell imaging provided evidence that Myh9 localised in branching lamellipodia and in the uropod where it may enable fast PMN migration. In summary, the severe migration defects *in vitro* and *in vivo* upon reduction of Myh9 expression indicated a fundamental role of Myh9 for PMN trafficking in innate immunity.

II Zusammenfassung

Während der akuten Entzündungsreaktion sind polymorphkernige neutrophile Granulozyten (PMN) die ersten Leukozyten, die in das entzündete Gewebe rekrutiert werden. Um während der Migration eine polarisierte Morphologie aufrecht zu erhalten, sind Moleküle der Nicht-Muskel-Myosine Klasse II (NMII) entscheidend. PMN besitzen nur eine der drei NMII-Isoformen, die in Säugerzellen exprimiert werden. Der NMII-Proteinkomplex in PMN basiert auf der schweren Kette 9 (Myh9). In dieser Studie sollte mit Hilfe von genetischer Herunterregulation der Myh9-Proteinmenge der funktionelle Einfluss von Myh9 auf das Migrationsverhalten von murinen PMN *in vitro* und *in vivo* aufgeklärt werden.

Zunächst wurde die Aktivität von NMII pharmakologisch mit dem Inhibitor pn-Blebbistatin gehemmt. Hierbei konnte nachgewiesen werden, dass die Migrationsgeschwindigkeit unter Flussbedingungen und die Morphologie während der Migration dosisabhängig beeinträchtigt wurden. Zusätzlich wurde eine verminderte Transmigrationsrate der pharmakologisch behandelten Zellen nachgewiesen. Im nächsten Schritt wurden *Vav-iCre*$^{+}$*/Myh9*$^{wt/fl}$ (*Myh9-cHet*) Mäuse generiert, da ein Knock-out im hämatopoetischen System letal war. Diese Tiere wiesen eine signifikante Reduktion der Myh9-Expression in PMN auf. Die Analyse der Migration unter Flussbedingungen auf einer 2D-Oberfläche ergab eine verminderte Migrationsgeschwindigkeit sowie eine Senkung der Euklidischen Distanz in *Myh9-cHet* PMN im Vergleich zu *Vav-iCre*$^{-}$*/Myh9*$^{wt/fl}$ (*Kontroll*)-PMN. Darüber hinaus waren die Transmigration und die Migration durch Engstellen im dreidimensionalen (3D) Raum i*n vitro* von *Myh9-cHet* PMN, im Vergleich zu *Kontroll*-PMN, erniedrigt. STED-Nanoskopie lieferte Hinweise darauf, dass eine Dysregulation des F-Aktin Netzwerks aufgrund der Reduktion von Myh9 der Mechanismus für die Migrationsdefekte sein könnte. In einem Model der akuten Peritonitis führte die reduzierte Myh9-Expression im hämatopoetischen System zu einer stark gesenkten Anzahl an extravasierten PMN in den intraperitonealen Raum. Ein weiteres *in vivo* Model, das auf einer Laser-induzierten Verletzung am Ohr der Maus beruhte, bestätigte die Verringerung der Extravasation von PMN in *Myh9-cHet* Mäusen im Vergleich zu *Kontroll*-Mäusen. Zusätzlich konnte dieses Model auch eine Herabsenkung der interstitiellen Migrationsfähigkeit der *Myh9-cHet* PMN im Vergleich zu *Kontroll*-PMN *in vivo* bestätigen. Unter Verwendung von drei verschiedenen Modellen von Knochenmarks-Chimären (1. Wildtyp-Mäuse mit einem hämatopoetischen System von Wildtyp-Tieren, 2. Wildtyp-Mäuse mit einem hämatopoetischen System von *Myh9-cHet*-Tieren und 3. Wildtyp-Mäuse mit einem hämatopoetischen System bestehend aus einer 50:50 Mischung aus Wildtyp- und *Myh9-cHet*-Tieren) konnte im akuten Peritonitis-Modell gezeigt werden, dass ein

zell-intrinsischer Mechanismus für die Migrationsdefekte von *Myh9-cHet* PMN verantwortlich war. Im weiteren Verlauf dieser Studie wurden aus Hoxb8-SCF-Zellen differenzierte PMN hinsichtlich ihres Migrationsverhaltens charakterisiert. Hierzu wurden *in vitro* Untersuchungen durchgeführt, in denen undifferenzierte und differenzierte Hoxb8-SCF-Zellen mit PMN aus dem murinen Knochenmark verglichen wurden. Es zeigte sich, dass Hoxb8-SCF-Zellen im Laufe der Differenzierung zu PMN ihren Zellkern, wie für PMN typisch, segmentierten. Auch erfolgte währenddessen, eine Herunterregulierung von Vorläuferzell-Oberflächenmarkern und eine Hochregulation von PMN-Markern bis zu einem Level, das für reife PMN typisch ist. In funktionellen Untersuchungen, welche die Integrin-Hochregulation nach Stimulation, die Induktion der Adhäsion, als auch die mechanotaktische und chemotaktische Migration auf 2D-Oberflächen überprüften, wurde ein Verhalten der differenzierten Hoxb8-SCF-Zellen sehr ähnlich zu PMN nachgewiesen. Hoxb8-SCF-Zellen wurden daraufhin aus den hämatopoetischen Vorläuferzellen der fötalen Leber von *Vav-iCre^{-}/Myh9$^{fl/fl}$*, *Vav-iCre^{+}/Myh9$^{wt/fl}$* und *Vav-iCre^{+}/Myh9$^{fl/fl}$* Embryos generiert. Die Myh9-abhängigen Migrationsdefekte in 2D und 3D konnten durch die Expression von EGFP-Myh9 in Hoxb8-SCF-Zellen mit einem Myh9 Knock-down, wieder aufgehoben werden. „Live Cell Imaging“ lieferte Hinweise darauf, dass Myh9 in verzweigten Lamellipodien und dem Uropod lokalisiert war, um möglicherweise eine schnelle Migration zu gewährleisten. Zusammenfassend weisen die schwerwiegenden Defekte in der Migration *in vitro* und *in vivo* bei verminderter Expression von Myh9 darauf hin, dass Myh9 für das Bewegungsverhalten von PMN in der angeborenen Immunreaktion eine fundamentale Bedeutung hat.

III Abbreviations

2D	2-dimensional
3D	3-dimensional
ADM	Adhesion medium
ANOVA	Analysis of variance
BDM	2,3 butanedione monoxine
bp	Base pair
BSA	Bovine serum albumin
cfu	Colony forming unit
cKO	Conditional knock-out
ctrl	Control
CXCL1	C-X-C motif chemokine
d	Days
DAMPs	Damage-associated molecular patterns
DFP	Diisopropyl phosphofluoridate
dHoxb8 cells	Hoxb8-SCF cell-derived neutrophils
DMEM	Dulbecco's modified Eagle's medium
DMSO	Dimethyl sulfoxid
DNA	Deoxyribonucleic acid
EDTA	Ethylenediamine-tetraacetic acid
EGFP	Enhanced green fluorescent
ELC	Essential light chain
ER	Estrogen responsive element
FACS	Fluorescence-activated cell sorting
FC	Flow cytometry
FITC	Fluorescein isothiocyanate
fwd	Forward
GEFs	Guanine exchange factors
GPCR	G-protein coupled receptor
h	Hours
HEPES	4-(2-hydroxyethyl)-1-piperazineethanesulfonic acid
het	Heterozygous
HL-60	Human promyelocytic leukemia cells
HPK1	Hematopoietic progenitor kinase-1
i.p.	Intraperitoneal
ICAM-1	Intercellular adhesion molecule-1
IF	Immune fluorescence
IgG	Immunoglobulin G
IL	Interleukin
LFA-1	Lymphocyte function-associated antigen-1
LPS	Lipopolysaccharide
m	Murine
mAbp1	Mammalian actin binding protein 1
Mac-1	Macrophage-1 antigen
min	Minutes

MLCK	Myosin light chain kinase
MLCP	Myosin light chain phosphatase
MPO	Myeloperoxidase
Myh	Myosin heavy chain
NADPH	Nicotinamide adenine
NETs	Neutrophil extracellular traps
NMII	Class II non-muscle myosin
o.n.	Over night
PAMP	Pathogen-associated molecular pattern
PBS	Phosphate buffered saline
PCR	Polymerase chain reaction
PE	Phycoerythrin
PECAM-1	Platelet/endothelial adhesion molecule-1
PFA	Paraformaldehyde
PI3K	Phosphatidylinositol 3-kinase
PIP3	Phosphatidylinositol (3,4,5)-triphosphate
PKC	Protein kinase
PMA	Phorbol myristate acetate
PMN	Polymorphonuclear neutrophils
pn-blebbistatin	Para-nitro blebbistatin
PSGL-1	P-selectin glycoprotein ligand-1
rev	Reverse
RLC	Regulatory light chain
rm	Recombinant murine
ROCK	Rho-associated protein kinase
ROS	Reactive oxygen species
RPMI	Roswell Park Memorial medium
RT	Room temperature
SCF	Stem cell factor
SEM	Standard error of the mean
Syk	Spleen tyrosine kinase
TAE	Tris base, acetic acid and EDTA
TBS	Tris buffered saline
TBST	Tris buffered saline with Tween®20
TNF-α	Tumor necrosis factors-α
VCAM-1	Vascular cell adhesion molecule-1
WB	Western blot
wt	Wildtype

1 Introduction

1.1 The acute inflammatory response

Acute inflammation is the rapid response of a tissue to injury. It is usually of short duration, lasting only minutes to hours. John Hunter, an English surgeon in the 18th century was the first to realise that this response was generally beneficial for the host and that inflammation can be regarded as the first line of defence against injury[1,2]. This injury, often accompanied by cell death, can be provoked by biological (e.g. bacteria), chemical (e.g. acid burn) or physical (e.g. surgical trauma) insults[3]. Acute inflammation is characterised by the cardinal signs redness (rubor), increased heat (calor), swelling (tumor), pain (dolor), identified by the roman physician A.C. Celsus, and loss of function (functio laesa), later described by Galen of Pergamon. Most of these symptoms are caused by the two main components of the acute inflammatory response: the microcirculatory response including dilatation of arterioles for increased blood supply to the affected area, increased permeability of capillaries to allow exudation of plasma proteins, and the cellular response, which is characterised by the emigration of leukocytes, predominantly polymorphonuclear neutrophils (PMN), from the vasculature into the inflamed tissue[4]. The inflammatory processes allow the removal of the injurious agent and necrotic tissue, as well as the preparation for healing, finally leading to a complete resolution[5]. Under these circumstances, the tissue injury is self-limited and only mild fibrosis occurs. However, if the inflammatory processes cause further injury, a self-perpetuating inflammatory loop can be induced leading to chronic inflammation[6,7].

1.1.1 The role of PMN

PMN are prominent members of the innate immune system and essential for an effective immune response [8,9]. The first to describe the relevance of these phagocytic cells for the elimination of foreign particles such as bacteria was the Russian zoologist E. Metschnikow in the late 19th century[10,11]. After release from the bone marrow, PMN circulate in the blood of mice with a half-life of approximately 12 hours[12]. In the human circulation, a similar life-span of PMN was identified using *ex vivo* labelling of PMN[13]. A more recent study using *in vivo* labelling, suggests a longer average circulation time of 5 days[12]. Under steady-state conditions, clearing of PMN occurs via apoptosis and engulfment by macrophages in the liver, spleen, and bone marrow [14,15] Very recent studies report homeostatic infiltration of PMN in naive tissues with the potential to support organ function[16] and describe a circadian rhythm protein as internal timer in PMN ensuring both, vascular protection and immune defence[17]. During acute inflammation, PMN are the first leukocytes to arrive at the site of

injury through rapid recruitment from the blood stream into the inflamed tissue[9]. This process is initiated by tissue resident macrophages or dendritic cells, which recognize components of bacteria or other pathogen associated molecular pattern (PAMPs) via specific pattern-recognition receptors such as members of the toll-like receptor family[18,19]. Damage associated molecular patterns (DAMPs) on the other hand, indicate tissue damage and can also be detected by these cell types[20]. DAMPs are mostly intracellular or nuclear proteins released during the cell death of damaged cells[21]. Subsequently, pro-inflammatory mediators like tumour necrosis factor α (TNFα) or interleukin-1β (IL-1β) are released, resulting in the activation of endothelial cells in the adjacent vessel[21-23]. As a consequence of their activation, endothelial cells upregulate adhesion molecules on the luminal side of the vessel, crucial for the recruitment and the extravasation of PMN[9,24,25]. Upon arrival in the interstitial tissue, PMN have been observed to swarm around a wounded area[26,27]. Initially, individual PMN, located close to the damage, migrate via chemotaxis towards the site of injury. The release of the lipid mediator leukotriene B4 amplifies the local signals and enhances the radius for PMN recruitment resulting in amplified chemotaxis of PMN, consequently leading to PMN clustering around the site of inflammation[27,28].

Once the PMN arrive at the site of inflammation, they can exert anti-microbial functions. The phagocytosis of C3b or immunoglobulin G (IgG) opsonised particles occurs via binding to CD11b or Fcγ receptors on the surface of PMN[29]. The PMN build a phagosome by enclosing the particle with the cell membrane. Subsequently, a phagolysosome develops by fusion of the phagosome with lysosomes which contain hydrolytic enzymes and calcium dependent NADPH-oxidase. NADPH-oxidases produces reactive oxygen species (ROS) through consumption of oxygen, a process known as respiratory burst[30]. Along with the oxidative active hypochlorous acid, built by the myeloperoxidase (MPO) catalysed process of chloride oxidation in the presence of hydrogen peroxide, ROS are crucial for the elimination of the engulfed pathogens[31,32]. Additionally, PMN store multiple proteases like neutrophil elastase, cathepsin G, or matrix metalloproteases and antimicrobial peptides like MPO, defensines and lysozyme in their granules[33,34]. These granules are either fused with the phagolysosomes or their content can be secreted into the extracellular space to eliminate pathogens[33]. Furthermore, PMN contribute to the elimination of pathogens through neutrophil extracellular traps (NET) formation. Specifically, PMN eject de-condensated chromatin decorated with proteins such as neutrophil elastase and MPO. The pathogens then become trapped and immobilised in the network and are potentially killed or damaged by the antimicrobial peptides and enzymes attached to the chromatin DNA[35,36]. The clearance of PMN from the

site of inflammation had been thought to occur by macrophages and monocytes in the tissue. However, recent studies have observed that PMN clear debris, perform essential repair functions, migrate away from the site of infection and are efficiently cleared from the tissue also in the absence of monocytes and macrophages[37-39]. Therefore, it is hypothesised that they may re-enter the blood stream. However, until today, no completely reverse-transmigrated PMN has been visualized and the physiological relevance remains unclear[40]. Despite their role as professional phagocytes, the presence of PMN at sites of inflammation is also crucial for effective recruitment of monocytes and immune cells from the adaptive immune system[41-44], along with the re-creation of new structures in the damaged tissue by collagen deposition, leading to healing[27,45].

1.1.2 The PMN recruitment cascade

The above introduced recruitment of PMN from the blood stream into the inflamed tissue follows a tightly regulated, consecutive multistep cascade. This includes capturing, fast and slow rolling, firm adhesion, adhesion strengthening, spreading, intraluminal crawling, transmigration, abluminal crawling, and interstitial migration to sites of inflammation[8,46] (Fig. 1).

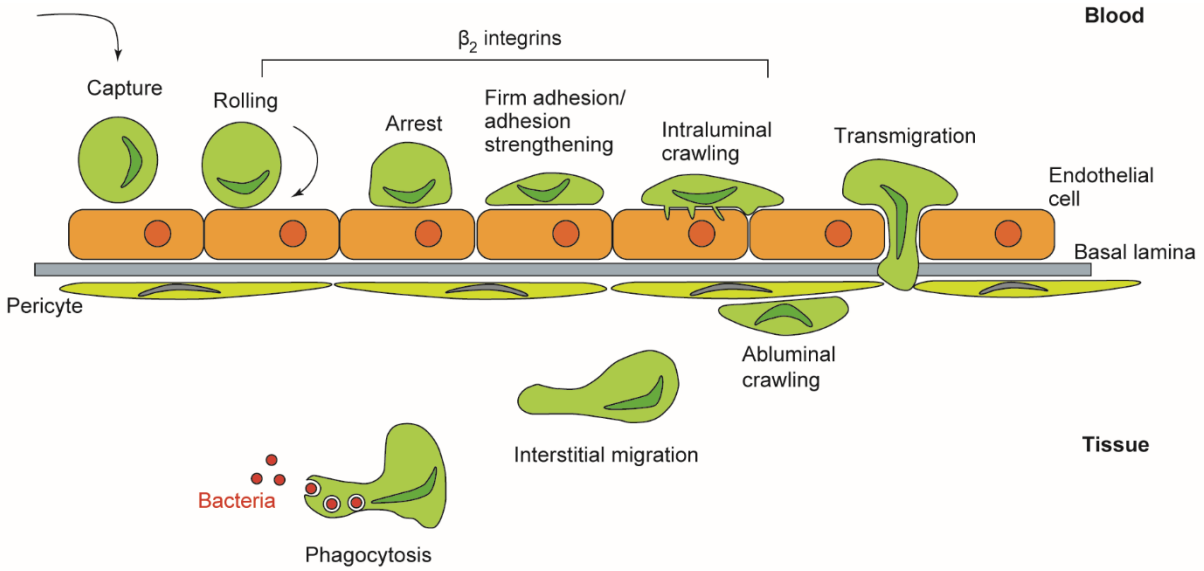

Figure 1. The PMN recruiting cascade. The recruiting of PMN during acute inflammation is arranged into consecutive steps. These steps are termed capturing, rolling, arrest, firm adhesion and adhesion strengthening, spreading, intraluminal crawling, transmigration, abluminal crawling and interstitial migration. At the site of inflammation PMN can fulfil their function as professional phagocytes to eliminate the source of inflammation. Despite the process of slow rolling, transmigration and interstitial migration, the other processes depend on the presence of β_2 integrins (modified from Schymeinsky et al. 2011[47]).

At first, freely circulating PMN in the blood get close to the inflamed vessel wall in a process called margination and are captured by the endothelial cells. The subsequent rolling is mediated by adhesion molecules of the selectin family presented by the endothelial cell and selectin ligands, such as the P-selectin glycoprotein ligand-1 (PSGL-1) on the PMN[48,49]. Endothelial cells express two different selectins, P-selectin and E-selectin. In contrast to P-selectin, E-selectin enables slower rolling velocities, facilitating the recruiting of PMN into the underlying tissue[50]. However, its availability on the endothelial cell surface is delayed due to de-novo synthesis upon stimulation. Conversely, P-selectin is stored in specific vesicles like the Weibel-Palade bodies in endothelial cells and can be presented on the endothelial cell surface within a few minutes after stimulation[51-53]. Importantly, the process of slow rolling requires additional support of β_2 integrins, presented by the PMN, and their interaction with the intercellular adhesion molecule-1 (ICAM-1), which is expressed on the cell surface of endothelial cells[54,55]. The interaction with PSGL-1 triggers a signalling cascade into the PMN resulting in a switch of the β_2 integrin from the bend, inactive E(-) H(-) conformation toward a partially activated β_2 integrin with intermediate affinity characterised by an extended (E+) conformation and a closed headpiece (H-), defined as E(+) H(-)[56-58]. For the transition into the high-affinity conformation, which is necessary for the firm adhesion of the PMN on the endothelium, further stimuli, originating from the endothelial cells, are required. The binding of the chemokine CXCL1 to its receptor, the G-protein coupled receptor (GPCR) CXCR2 is one example that leads to the full activation of the β_2 integrin characterised by an extended conformation and an open head domain, E(+) H(+)[59,60]. This process is termed inside-out signalling[61]. The extension of the head domain away from the plasma membrane requires the binding of the adapter protein Talin-1 on the cytoplasmic tail of the CD18 subunit of the β_2 integrin[62,63]. For the opening of the headpiece by dissociation of the two β_2 integrin subunits, the adaptor protein kindlin-3 is crucial[63,64]. PMN have been found to influence their activation state through an endogenous anti-inflammatory mechanism by binding their β_2 integrin to ICAM-1 in cis leading to stabilisation of the bend conformation with an open headpiece, E(-) H(+) and inhibition of adhesion[65]. Post-adhesion events like adhesion strengthening and spreading of the PMN are further promoted through outside-in signalling from the β_2 integrin into the cell upon binding to its ligand ICAM-1[66]. In the case of ligand binding in trans, signalling events lead to a reorganisation of the cytoskeleton, enabling spreading, and an increase in integrin-ligand interactions, strengthening the bond between the PMN and the endothelium[8]. Upon establishment of polarity, PMN migrate in an β_2 integrin-dependent fashion along the endothelium to find a suitable spot for extravasation into the inflamed

tissue[67,68]. The transmigration through the endothelium can occur via the paracellular or the transcellular route[69] and is dependent on the smooth and effective execution of the complex communication and interaction processes between endothelial cells and PMN[70]. In endothelial cells, the engagement by PMN triggers extensive dynamic modifications of the actin cytoskeleton, including the induction of membrane structures around adherent PMN, so called transmigratory cups, that support the transmigration of PMN[71,72]. Upon successful transmigration through the endothelial cell layer, PMN pass the basal membrane of the blood vessel and migrate along pericytes in an β_2 integrin-dependent fashion along the abluminal side of the blood vessel[73-76]. To finally reach the site of inflammation, PMN migrate in a directed fashion through the fibrillary network of the interstitial space[77-79]. With the recruitment completed, PMN can exert their defence functions in the tissue.

A proper operating PMN recruitment to the site of inflammation is crucial for humans and mice. Misfunctions in this process lead to insufficient immune responses and recurring infections as described in patients with leukocyte adhesion deficiency (LAD) I – IV, caused by mutations of CD18, malfunction of selectin ligands, a mutation of kindlin-3 preventing the E(+) (H+) β_2 integrin conformation, or a dominant-negative mutation in Rac2[80-83].

1.2 The mechanisms of PMN migration

The mobility of cells is fundamental for correct functioning of the body for any organism throughout its lifespan. During embryonic and postnatal development, various cell types need to migrate to their destination to organise organs and tissues for proper functionality. In the process of angiogenesis, cells need to migrate to form new vessels. In the case of inflammation, cells must be able to migrate to the lesion to eliminate the source of inflammation and to progress wound healing and tissue regeneration[84]. Two characteristic modes of migration can be distinguished: mesenchymal and amoeboid migration. Fibroblasts, smooth muscle cells, endothelial and epithelial cells have been described to perform mesenchymal migration, whereas most blood cells migrate in an amoeboid fashion[85]. Epithelial cancer cells, after epithelial-to-mesenchymal transition, can migrate with a mesenchymal phenotype and some even adopt amoeboid migration[86]. Cells migrating in the mesenchymal mode display an elongated spindle-like shape with one or often more leading pseudopods. The process is mainly driven by actin-rich protrusions promoted by the small GTPases Rac and Cdc42. The cells show strong adhesive interactions with the extracellular matrix via integrins. Stress fibres and focal adhesions are employed to generate traction force and to recruit extracellular matrix degrading proteolytic enzymes used to generate a path for

migration. In contrast, amoeboid migrating cells display a rounder morphology with usually one single protrusion at the leading edge. They are highly deformable and undergo constant shape changes. Their strong signalling via the Rho/ROCK pathway and their contractile actin cortex enables these cells to squeeze through gaps. Hence, the proteolytic activity in amoeboid migrating cells is low or absent. In combination with lower substrate adhesiveness compared to mesenchymal migrating cells, amoeboid migrating cells display a much higher migration speed and can react faster to changes in chemotactic stimuli in their environment[84-86].

PMN belong to the group of cells that employ amoeboid migration. Specifically, actin polymerization is essential for the protrusive formation of the leading edge of migrating cells, whereas contraction of the acto-myosin network assists movement by retracting the back of the cell[87,88]. For the cytoskeletal dynamics and directed migration, the sensing of chemoattractant gradients and the intrinsic ability of the cells to establish a polarised state are fundamental. Polarisation is induced by binding of chemoattractants to GPCRs, which are seven-transmembrane domain receptors and are evenly distributed throughout the cell membrane[89]. PMN can react to very shallow chemoattractant gradients in their environment by internal signalling amplification leading to a much higher intracellular asymmetry compared to the small extracellular asymmetry[90]. Upon activation, the GPCR-interacting heterotrimeric G-protein subunits Gα and Gβγ dissociate from the receptor resulting in downstream activation of effector proteins including Ras, RhoA, protein kinase Cβ (PKCβ), adenylyl cyclase or phospholipase C (Fig. 2)[91]. For the establishment of a leading edge, the phosphatidylinositol 3-kinase (PI3K) becomes directly activated by the Gβγ subunit. This results in activation of phosphatidylinositol (3,4,5) triphosphate (PIP3) and Rac-guanine exchange factors (GEFs), stimulating the activity of the small GTPase Rac. Together with Cdc42, another small GTPase, Rac is crucial for stabilisation of the leading edge and actin polymerization to push the cell forward[46,92,93]. For the formation of a trailing edge, the small GTPas RhoA becomes enriched and activated at the uropod upon release from its inhibitor moesin[94]. The PTEN phosphatase, which acts negatively on PI3K and PIP3 is simultaneously recruited to the rear of the cell in a RhoA dependent manner[95]. RhoA activates the myosin light chain kinase ROCK which drives contraction of the rear[96,97]. A regulatory feedback loop between the effector molecules acting at the leading and the trailing edge of the cell ultimately secures actin polymerization and acto-myosin contractility in a spatiotemporal manner[92,94].

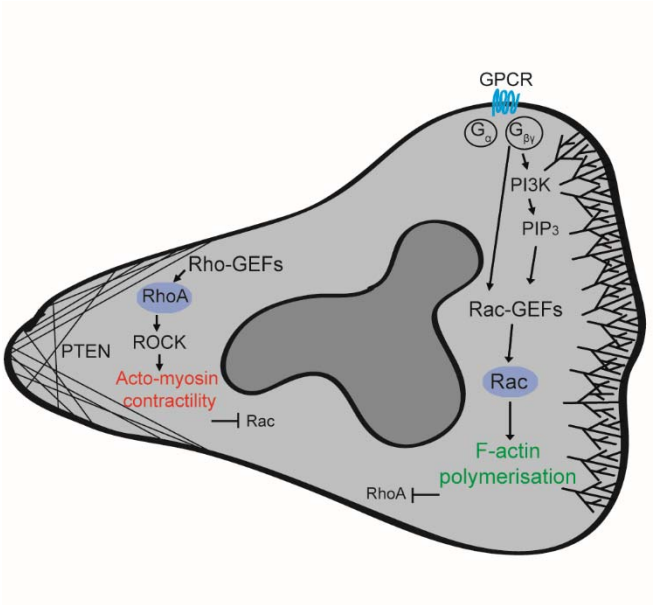

Figure 2. Signalling during PMN polarisation. Upon GPCR signalling, the dissociated subunit Gβγ activates Rac-GEFs or PI3K producing PIP_3. A positive feedback loop in the front of the cell activating Rac and inhibiting Rho signalling results in active actin polymerization that pushes the cell forward. The back of the cell is characterised by RhoA signalling and PTEN recruitment which results in acto-myosin contractile forces and inhibition of Rac signalling at the back of the cell (adapted from Gambardella et al. 2013[89]).

During their recruitment to sites of inflammation, PMN must migrate in environments with different requirements. To meet these requirements, PMN possess highly specialized molecular mechanisms. It has been demonstrated that integrins are crucial in mediating adhesion on surfaces and enabling force transmission in this two-dimensional (2D) environment[8,98]. For example, murine PMN lacking the β_2 integrin lymphocyte function-associated antigen-1 (LFA-1, CD11a/CD18) have severely impaired adhesion in inflamed postcapillary venules, whereas murine PMN with a deletion of macrophage-1 antigen (Mac-1, CD11b/CD18) are able to induce adhesion but are not able to migrate along the endothelial cells *in vivo*[67]. Also, abluminal crawling of PMN along the pericyte layer has been found to be β_2 integrin dependent in mice *in vivo*[75]. Locally applied blocking antibodies against β_2 integrins hinder the interaction of ICAM-1 expressing pericytes with LFA-1 and Mac-1 expressing PMN, resulting in reduced migration speed and track length of PMN migrating along pericytes in mice[75]. Recently, an unexpected role for integrin-mediated adhesion has been discovered using a mouse model of sterile injury in the ear skin dermis and PMN deficient for β_2 integrins or talin, resulting in PMN lacking the intermediate and high-affinity conformation of integrins. Here, the deficient PMN accumulate at the transition zone between three-dimensional (3D) fibrillar interstitium and the cell-rich collagen-free wound zone and fail in contrast to wildtype PMN to accumulate in the centre of the wound, suggesting that β_2 integrins are in involved in movement within cell clusters[27,77].

Analysis of murine PMN migration in 3D collagen gels *in vitro* and in the interstitium of the mouse ear *in vivo* demonstrate integrin-independent migration in this environment: Talin or

β2 integrin deficient PMN as well as PMNs treated with β2 integrin function-blocking antibodies migrate as efficiently as control PMN in fibrillar 3D environment[77,87,99]. Forward movement under these circumstances is solely based on the two force generating principles of plasma membrane expansion via actin polymerization at the front of the cell and acto-myosin based contraction at the rear of the cell[87,88,100]. Hence, the fibrillar environment of the intersitium or *in vitro* collagen networks provide sufficient traction force transmission from the PMN to the environment to ensure proper cell movement even without anchoring integrins.

In vivo, PMN need to adhere and migrate under shear stress provoked by the blood stream. PMN migrate in the direction of the blood flow, but also against and perpendicular to the direction of flow until they reach a suitable extravasation site[9,67]. Here, β2 integrins in their high affinity conformation are crucial for resistance against shear stress[59,101]. In addition, several other proteins have been identified with specific importance under flow conditions. This means that they are dispensable for migration under static conditions, yet crucial for effective migration under flow conditions. In this context, Vav1, a GEF for the Rho family GTPases Rac and Cdc42, is important for the organisation of the actin cytoskeleton during leukocyte polarisation and migration. Murine PMN which lack Vav1 have been shown to lose their ability to migrate against and perpendicular to the direction of flow[102]. The mammalian actin-binding protein 1 (mAbp1) becomes activated by the nonreceptor spleen tyrosine kinase Syk during the process of slow rolling[103,104]. *In vitro* and *in vivo* studies in mice have demonstrated impaired adhesion, intraluminal crawling and extravasation of mAbp1 deficient PMN and suggest a role for mAbp1 in stabilising the high affinity conformation of β2 integrins[104]. Additionally, the mAbp1 interacting protein hematopoietic progenitor kinase (HPK)1 has been found to be required for CXCL1-induced high-affinity LFA-1, but dispensable for Mac-1 affinity regulation. HPK1-deficient murine PMN fail to adhere and migrate properly under flow conditions *in vitro* and *in vivo*[105]. Furthermore, the RhoA-specific GEF-H1 has been demonstrated to be crucial for adhesion, spreading and migration exclusively under shear stress conditions. Shear stress promotes its activation through dissociation from the microtubules and its relocation to the uropod of the cell. Here, it exerts its function in regulating the activity of RhoA, presenting a link between mechanosensing and Rho signalling[106]. In summary, PMN adapt their highly specific molecular mechanisms and specialized signalling pathways to the requirements of a changing environment during their recruitment from the blood stream to the site of inflammation.

1.3 The myosin superfamily

Myosins are a large and diverse superfamily of actin-based molecular motors[107]. Due to their ability to convert chemical energy through ATP hydrolysis into mechanical energy they are classified as mechanochemical enzymes[108]. In contrast to kinesins and dyneins which utilise microtubules for transport, myosins move along actin filaments[108]. All myosins are composed of at least one heavy chain and several light chains. The heavy chain is organised into three domains with different structures and functions[109]. The most conserved domain is the globular head domain containing the ATP- and actin binding sites. The α-helical neck region lies adjacent to the head domain and associates with the light chains regulating the activity of the head domain. The tail domain contains binding sites that determine the specific activities of that particular myosin and displays the most sequence divergence enabling the discrimination between myosin subgroups or isoforms[110]. The class II myosin subfamily has the most members and includes the first described myosin, the skeletal muscle myosin. In vertebrates there are over 15 different isoforms known, each identified by a different heavy chain[107]. The skeletal muscle myosin, along with cardiac and smooth muscle myosin as well as non-muscle myosin are also known as conventional myosins[111]. All other classes are termed unconventional. Along these over 17 classes, class I myosins are the most abundant group[112]. The structure of class I and II myosin is strikingly different and is reflecting their specific functions. Class II myosin is known to be involved in generating force for contraction, whereas class I myosin is proposed to play various cellular roles related to membrane dynamics and trafficking[111]. Class II myosin molecules are hexamers composed of a heavy chain dimer and two pairs of myosin light chains[113]. The α-helical sequences in the tails of the heavy chains allow the association of the two monomers to a rod-like coiled-coil structure. Due to the lack of this α-helical sequence in class I myosin, these molecules exist as monomers. Between class I and II myosin, the type and number of light chains bound to the neck region differs, with one calmodulin light chain for class I myosin and two different light chains, termed essential and regulatory light chain, for class II myosin[108]. Importantly, all eukaryotic cells contain class II non-muscle myosin molecules resembling their muscle counter-parts with respect to structure and function. However, their regulation is fundamentally different to skeletal and cardiac muscle myosin. The latter are primary regulated through a set of actin-associated proteins named troponin and tropomyosin, whereas class II non-muscle myosin is regulated by phosphorylation of one of the light chains, termed regulatory light chain (RLC), allowing them to respond to numerous signals from outside and inside the cell[114,115].

1.3.1 Class II non-muscle myosin

In mammalian cells, there are three different genes for class II non-muscle myosin (NMII), located at three different chromosomes in humans and mice. These genes encode for the heavy chain of NMII determining the NMII isoform. Deletion of the specific heavy chain results in the loss of that NMII isoform. The heavy chain gene Myh9 encodes for NMIIA, Myh10 for NMIIB and Myh14 for NMIIC. Myh10 and Myh14 have been shown to undergo alternative splicing whereas for Myh9 only one mRNA variant has been reported[116]. The three heavy chain isoforms display around 64–89% sequence similarity but have different actin-activated Mg^{2+}-ATPase activities and duty ratios, meaning the fraction of time that the myosin motor is bound to an actin filament[116].

The most unique characteristic of class II myosin and therefore also of NMII, is the ability to form filaments via self-association of the rod-like coiled-coil α-helical tail of two or multiple heavy chains. These myosin filaments can link actin filaments together into thick bundles forming cellular structures such as stress fibres[117,118]. The formation of an acto-myosin filament occurs in consecutive steps[119]: In the absence of regulatory light chain (RLC) phosphorylation, head-to-tail interaction of the heavy chain stabilises a compact, auto-inhibitory, and assembly incompetent conformation (Fig. 3A). Upon RLC phosphorylation, unfolding of the tail promotes the assembly competent, extended conformation (Fig. 3B). This conversion to the extended conformation also triggers the Mg^{2+}-ATPase activity of the motor and enables the assembly into bipolar filaments (Fig. 3C). This filament assembly relies on the presence of C-terminal structures of the heavy chain tail which contain assembly-competent domains and the non-helical tail and can be controlled by phosphorylation[119]. For the formation of these bipolar filaments, class II myosin monomers have to interact both parallel and anti-parallel resulting in a central bare zone which is not populated by motor domains and is designed to pull actin filaments towards the centre[120]. Interestingly, NMIIC has been found to have a longer bare zone and narrower filaments than NMIIA and B, indicating that NMIIC filaments incorporate less molecules[121]. The composition of these myosin filaments can be homotypic and, at least between NMIIA and B, heterotypic. In cell regions with predominantly NMIIA or NMIIB, homotypic filaments are dominant, in cell regions with colocalisation of NMIIA and NMIIB heterotypic filaments prevail[122]. In the final step during the generation of an acto-myosin filament, the bipolar NMII filaments link F-actin together enabling the cell to generate force (Fig. 3D). Force generation for contraction occurs through the sliding movement of the motor domains of the myosin filaments along and within the actin filaments.

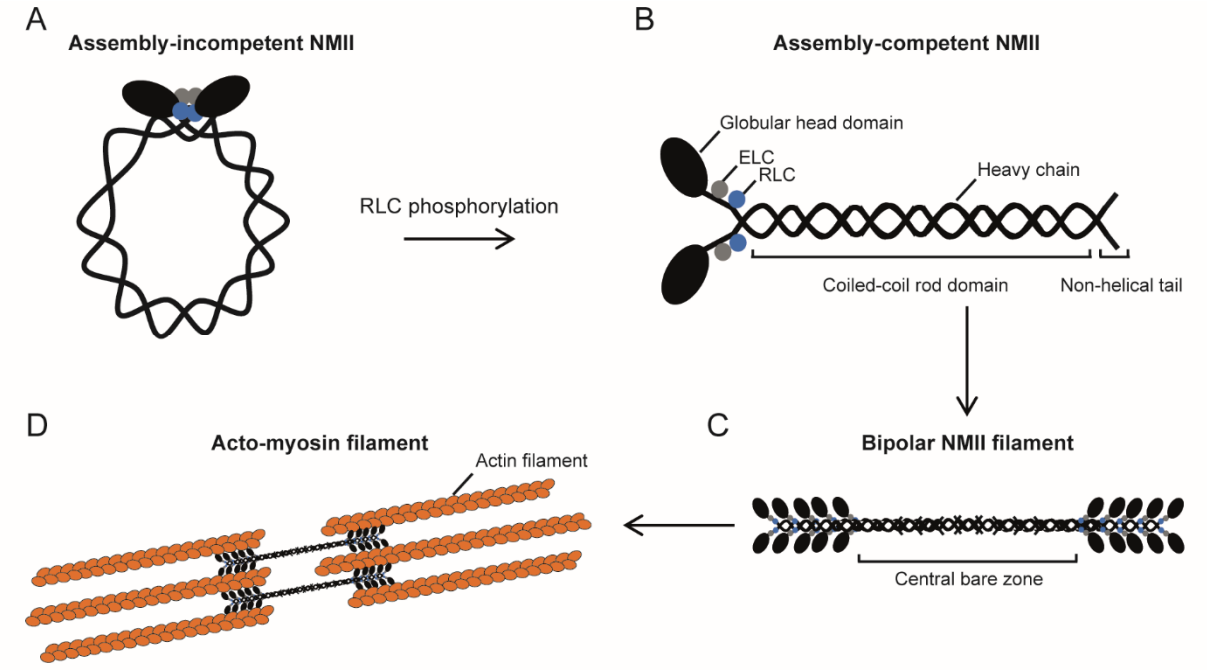

Figure 3. Assembly of class II non-muscle myosin (NMII) and acto-myosin filaments. The NMII heavy chain is shown in black, the associated essential and regulalatory light chains (ELC and RLC) are shown in grey and blue. The globular head domain contains actin-binding regions and the enzymatic Mg^{2+}-ATPase motor domain. **(A)** In the absence of RLC phosphorylation, NMII forms a compact molecule through a head-to-tail interaction that is unable to associate with other NM II dimers. **(B)** Phosphorylation of the RLC promotes unfolding of the tail to the assembly competent, extended conformation. **(C)** The conversion to the extended conformation triggers the Mg^{2+}-ATPase activity and NMII assembly into bipolar filaments through both parallel and anti-parallel interactions between the coiled-coil tail domains of NMII monomeres. **(D)** The bipolar NMII filaments bind to F-actin through their head domains, linking actin filaments together into thick bundles (lower left side). The ATPase activity of the NMII head enables a conformational change that can move the actin filaments in an anti-parallel manner (adapted from Dulyaninova et al. 2013[119]).

For decades, researches have tried to identify the specific expression pattern, subcellular localisations and functions of the three NMII isoforms NMIIA, B and C. Immunofluorescence staining, protein expression analysis by western blot and mass spectrometry, quantification of mRNA levels and several mouse models have provided valuable insights, however, it also has become clear that the functions of the NMII isoforms differ between cell types, depending on the combination, distribution and amount of the particular isoforms[116,123-127]: Mice ablated for Myh9 fail to develop a proper visceral endoderm and die by E7.5. These mice show defects in cell-cell adhesion by loss of proper E-cadherin and E-catenin localisation within cells[126]. Interestingly, the expression of Myh10 or Myh14 under the Myh9 promotor rescues survival beyond organogenesis but mice show major defects in placental development through lack of

foetal blood vessels in the labyrinthine layer, the interface for gas and nutrient exchange between the embryo and the mother[124,128]. These observations fit together with the widespread expression of Myh9 in embryonic tissues and the specific expression of Myh9 in the vasculature of the brain and the inner ear, in epithelial cells in the developing intestine and in non-myocytes in the heart. In adult organs, Myh9 is still absent in mature cardiac myocytes, expressed at low levels in the heart, and is the most abundant isoform in the spleen[116,123,124]. The knock-out of Myh10 in mice causes embryonic lethality by E14.5 due to abnormalities in the heart, with defects in cardiac myocyte cytokinesis and karyokinesis[120,122]. Moreover, the embryos show malformations in the hippocampus, which can be partly explained by defects in neuron migration in reaching their destination in the developing brain[127,129,130]. Myh9 expression under the Myh10 promotor can partly rescue the defects in brain development, however the cardiac defects remain[124,131]. The expression pattern of Myh10 during embryonic development and in adult organs corresponds well with these findings in Myh10 knock-out mice: Myh10 is the abundant isoform expressed in neuroepithelial cells and neurons, mesenchymal epithelial cells in the inner ear, serosal cells in the intestine, the parenchymal cells in the lung and in ventricular cardiac myocytes. In the adult murine and human organism, Myh10, is most strongly expressed in the brain and mature cardiac myocytes[116,124,132,133]. The generation of Myh14 knock-out mice has revealed no obvious phenotype. Only in combination with reduced Myh10, defects have been identified, including impaired cell division of ventricular myocytes. This defect causes a marked reduction in the number of cardiac myocytes in the hearts of the embryo, as well as embryonic lethality at E14.5. A compensatory interaction between Myh10 and Myh14 in cardiac myocytes has therefore been suggested[111,116,123]. The observations in these mice are in line with the expression pattern of Myh14 in embryonic and adult tissues. Here, no Myh14 has been found in the embryo before E11.5. During later embryonic development, Myh14 is detectable in the pituitary of the brain, in the sensory cells of the cochlea in the inner ear, at the apical boarders of epithelial cells in the intestine, in airway epithelial cells in the lung, and in ventricular cardiac myocytes[116,124,134]. In adult tissue, only in the lung Myh14 can be found in a measurable amount. Here, a third of the total NMII protein is Myh14[123].

In summary, these findings suggest overlapping functions, as well as specific, non-compensable functional roles of the three NMII isoforms. In most cell types the distinct roles of the single isoforms is not completely understood, but a fundamental role for NMII for cytokinesis in cell division, substrate adhesion and cell-cell adhesion, as well as mediating cell shape change, polarisation, and migration is indisputable[107,118,135-141]. Several examples

for the role of NMII in cell division have been described. For instance, in HeLa cells and other dividing epithelial cells Myh9 and Myh10 locates to the cleavage furrow[122,125]. In addition, downregulation of Myh10 in COS-7 cells leads to reduced proliferation and enhanced percentage of poly-nucleated cells[142]. Downregulation of Myh10 in megakaryocytes also leads to polyploid cells as only Myh10 but not Myh9 locates to the cleavage furrow during cell division[143]. Finally, in hematopoietic progenitor cells, inhibition of NMII causes cytokinesis-associated cell death[144].

1.3.2 Myh9 - a class II non-muscle myosin heavy chain

In most mammalian cell types all three isoforms, Myh9, Myh10 and Myh14, are simultaneously expressed. In hematopoietic cells, Myh9 is the dominant heavy chain for NMII[125,145]. For proper function of the NMIIA, with Myh9 as its heavy chain, the phosphorylation of the RLC is required. Several kinases have been reported to phosphorylate the RLC of NMIIA. In PMN, one of the few cell types in the body solely expressing Myh9 and the leukocytes with the highest expression of Myh9[125], three kinases involved in RLC phosphorylation have been described. The Ca^{2+}-calmodulin activated myosin light chain (MLC) kinase (MLCK) and the RhoA controlled Rho-associated, coiled coil-containing kinase (ROCK), phosphorylate the RLC at Ser19 and Thr18, whereas the protein kinase C (PKC) targets Ser1 and 2 and Thr9[93,146,147]. On the other site, myosin light chain phosphatase (MLCP) has been found to dephosphorylate the RLC[119] and it plays a role in breaking symmetry in the process of polarisation in PMN by attractant-induced local inactivation of moesin, resolving the inhibition of the small GTPases Rac, Rho, and Cdc42[94]. In migrating T cells, MLCK and ROCK have been found to be spatially segregated, with MLCK mainly to the leading edge and ROCK enriched at the trailing edge. Here, inhibition of calmodulin leads to the retraction of the front of the cell, whereas inhibition of ROCK prevents the detachment of the trailing edge[96]. This supports the concept that cycling activity levels of MLCK and MLCP at the leading edge, and ROCK and MLCP at the sides and the trailing edge of the cell, result in locally controlled phosphorylated MLC levels, enabling the cell to orchestrate the building of protrusions, new and transient adhesion sites as well as directional migration[148]. The role of the RLC kinase PKC is not completely understood and seems to vary between cell types and environments. For instance, inhibition of PKCβII in PMN responding to chemoattractant stimulation causes severe tail retraction defects. Non-inhibited PKCβII translocates transiently to the plasma membrane, where it activates adenylyl cyclase 9 to induce cAMP production which results in downstream RLC phosphorylation[91]. In fibroblasts,

direct phosphorylation of the RLC by PKC decreases myosin activity through access restriction of MLCK to the RLC, resulting in a reorganisation of acto-myosin filaments[149]. Furthermore, PKCβ has been found to phosphorylate the heavy chain Myh9 at Ser1916 near the C-terminal end of the coiled-coil region in human platelets and T cells[119,150,151].

In line with this, there is emerging evidence for a pivotal role of the tail domain of the heavy chain, for controlling subcellular distribution of Myh9 and NMII filament formation[119]. Deletion studies involving the uncoiled tailpiece of the coiled-coil rod domain of the heavy chain have demonstrated its importance for functional relocation of the molecule: In COS-7 cells, tailpiece deleted Myh9 is not able to colocalise with the cortical F-actin and remains homogenously distributed in the cytoplasm[152]. In natural killer cells, tailpiece deleted Myh9 fails to associate with cytotoxic granules and prevents the secretion of perforin containing cytotoxic granules. Moreover, the phosphorylation at Ser1943 of Myh9 is crucial for the association between Myh9 and the cytotoxic granules[153]. In mast cells, the onset of degranulation has been demonstrated to be associated with phosphorylation of Myh9 at Ser1916[154]. In a human epithelial cell line, swapping of the C-terminal amino acids 179–190 between Myh9 and Myh10 inverts the distinct distribution pattern of these two isoforms during migration[136]. Moreover, in U2O3 epithelial cells, the Myh9 tail is phosphorylated at Ser1916 by PKCβII upon integrin binding and subsequent Rac-1 activation. This has been described to be essential for recruitment of Myh9 to focal adhesions and their maturation[155].

The mammalian α-kinase transient receptor potential melastatin 7 (TRPM7) has been identified to phosphorylate human and murine Myh9 at Thr1800, Ser1803 and Ser1808[152]. In COS-7 fibroblasts, mutation of TRPM7 phosphorylation sites to phospho-mimetics reduces its incorporation into the acto-myosin cytoskeleton and results in its relocalisation away from the cell cortex[152]. In MDA-MB-231 breast cancer cells, casein kinase II (CKII) has been found to phosphorylate Myh9 at Ser1943[119]. This phosphorylation is associated with reduced NMIIA filament assembly[156]. A S1943 phospho-mimetic mutant increased migration, whereas a S1943 non-phosphorylable mutation caused over-assembly of NMIIA during spreading inhibiting cell migration[157].

Cell specific genetic approaches using mouse models have enabled the elucidation of NMII isotype specific functions such as the migration of immune cells. Cell specific Myh9 knock-outs have been reported for T cells, dendritic cells, and platelets. In T cells, Myh9 is accumulated at the rear of transmigrating T cells which is crucial to squeeze the nucleus through sites of constriction[158]. *In vivo,* Myh9 conditional knock-out in T cells impairs the turnover of adhesion sites, resulting in increased adhesion and impaired interstitial

migration[159]. In addition, Myh9 has been found to be important for the disassembly of binding between LFA-1 and the ICAM-1, and retraction of the membrane at the rear of the T cell[160]. Using mass spectrometry, immunoprecipitation and confocal microscopy, an association between the C-terminal end of chemokine receptor CXCR4 and Myh9 has been described in T cells, suggesting a mechano-signalling mechanism with a biochemical association between chemokine receptors and motor proteins[161]. Other studies have implied that Myh9 serves as a mechanical link between LFA-1 and the cytoskeleton potentially influencing the activation state of LFA-1 in T cells[162,163]. For the functionality of the adaptive immune response, T cells interact with antigen-presenting cells via the immunological synapse. Myh9 has been found to be recruited to the immunological synapse and to be an essential participant in the formation and persistence of the immunological synapse and TCR signalling[164,165]. In dendritic cells, tight spatiotemporal regulation of Myh9 has been demonstrated to be crucial for migration and antigen capture[166]. Mice with an ablation of Myh9 in megakaryocytes display macrothrombocytopenia with a strong increase in bleeding time[167]. Thrombus growth, organisation, and stability is impaired, because of the important role of Myh9 for platelet contractility and outside-in signalling. Recently, it has been reported that Myh9 is crucial for platelet migration to fulfil their role as mechano-scavengers, binding and collecting bacteria as well as fibrinogen[168]. Knock-down studies targeting Myh9 by RNA interference provide evidence that Myh9 is required in B cells for B cell receptor (BCR)-driven antigen presentation by participating in the formation of MHC II-peptide complexes from antigens uptaken by the BCR[169]. In natural killer cells, knock-down of Myh9 impairs cytotoxicity through defective degranulation[170]. Another study has revealed that Myh9 binds natural killer cell granules via its tail domain and therefore enables the integration into the F-actin network as well as the transport to the immunological synapse to ensure exocytosis[153,171].

During the process of differentiation, Myh9 is highly upregulated in PMN resulting in the highest expression of Myh9 amongst the immune cells and suggesting a particular functional importance for this molecule in this cell type, especially, as Myh9 has to execute all functions that are elsewhere divided between two or three isoforms[144,172]. Previous studies analysing the role of Myh9 for PMN migration have been restricted to the use of the pharmacological inhibitors 2,3-butanedione monoxime (BDM) and blebbistatin. BDM operates as ATPase and therefore affects the activity of myosins and many non-myosin proteins. Blebbistatin blocks NMII activity by binding in a cleft in the motor domain. At this position it blocks the conformational change of the motor domain which is necessary to pull F-actin bundles together.[173-176] Treatment of human PMN-like differentiated HL-60 cells with blebbistatin

suggests a role of NMIIA in the maintenance of membrane tension during establishment of the leading-edge protrusion and in the prevention of secondary pseudopods in 2D environments[177]. Treatment of human PMN with blebbistatin compromises tail retraction during transmigration through a TNFα-activated endothelial monolayer[146]. Similarly, studies with murine PMN using the inhibitor BDM as well as blebbistatin have revealed a tail retraction defect during 2D migration under static conditions[92,93,178]. Furthermore, in confined 3D environment, blebbistatin studies in murine PMN suggest that uropod contractility relies on NMIIA to squeeze the nucleus through sites of constrictions[87].

These studies point to an important role of Myh9 for PMN migration. However, all these studies rely solely on the pharmacological inhibition of NMII. The employment of these inhibitors bears limitations, which obliges to take the results of the conducted studies with caution and reveals the necessity of genetic studies to delineate the specific function of Myh9 in PMN.

1.4 Aims of the study

NMII molecules are important molecular motors in multiple mammalian cell types. The distinct role of Myh9, the heavy chain of NMIIA, in the PMN recruiting cascade has been only unsatisfactory investigated using pharmacological inhibitors and genetic studies are lacking. Therefore, this study sets out to decipher the functional impact of Myh9 for PMN migration using genetic downregulation of Myh9 in the hematopoietic system.

In the first part of the study, the impact of pharmacological inhibition of NMII activity on different steps of the PMN recruiting cascade will be analysed *in vitro*. In contrast to earlier studies, this work will focus on experiments under flow conditions to mimic the *in vivo* environment during PMN trafficking to sites of inflammation. This data will be compared to previous findings under static conditions to evaluate differences and similarities.

The second part of the study will investigate the consequences of genetic downregulation of Myh9 on PMN trafficking. Therefore, a mouse line with a knock-down of Myh9 in the hematopoietic system will be generated, by employing the Vav-iCre system and $Myh9^{fl/fl}$ mice generating $Vav\text{-}iCre^{+}/Myh9^{wt/fl}$ (*Myh9-cHet*) mice. PMN isolated from the bone marrow of these mice and littermate $Vav\text{-}iCre^{-}/Myh9^{wt/fl}$ (*control*) mice, will be examined for their potential to migrate under flow conditions and in confined 3D collagen matrixes as well as for their capacity to sense and orientate towards a chemoattractant. Immunofluorescence staining will be employed to analyse the subcellular localisation of Myh9 and Actin in *Myh9-cHet* and *control* PMN. To evaluate the *in vitro* findings *in vivo*, a CXCL1-induced peritonitis model as well as a laser-induced ear injury model will be conducted. Furthermore, three different models of bone marrow chimeric mice, namely wildtype mice carrying a wildtype hematopoietic system, wildtype mice carrying a *Myh9-cHet* hematopoietic system and wildtype mice carrying a hematopoietic system consisting of a 50:50 mixture of wildtype and *Myh9-cHet* cells, will be generated and the CXCL1-induced peritonitis model will be performed to analyse whether reduced Myh9 expression in other cell types can influence the trafficking behaviour of PMN in that model.

The third aim of this work is the performance of rescue experiments to verify the results with the *Myh9-cHet* mice, as specifically caused by the reduced Myh9 expression. For this purpose, an immortalized hematopoietic progenitor cell line that can be differentiated towards PMN will be used, as PMN cannot be genetically manipulated. To this end, Hoxb8-SCF cell-derived neutrophils (dHoxb8 cells) are to be established as a tool to study PMN trafficking *in vitro*. The optimisation of differentiation towards PMN will be based on the phenotypic comparison between murine bone marrow-derived PMN and dHoxb8 cells,

comparing nuclear morphology and cell surface progenitor and murine PMN markers. In addition, the behaviour of dHoxb8 cells in functional assays will be assessed. Hoxb8-SCF cell lines will be generated from progenitor cells of the foetal liver of *Vav-iCre^{-}/Myh9$^{fl/fl}$*, *Vav-iCre^{+}/Myh9$^{wt/fl}$* and *Vav-iCre^{+}/Myh9$^{fl/fl}$* (*Myh9-knock-down)* embryos. A Myh9-EGFP expressing *Myh9-knock-down* Hoxb8-SCF cell line (*Myh9-RES*) will be generated and *Myh9-RES* dHoxb8 cells will be compared to *Myh9-knock-down* dHoxb8 cells in their efficiency to migrate under flow conditions and in 3D collagen matrixes. To draw conclusions on the function of Myh9 for migration, the spatial-temporal localisation of Myh9 during migration will be analysed using live-cell imaging of migrating *Myh9-RES* dHoxb8 cells.
Altogether, this study aims to shed light on the mechanistic involvement of Myh9 in PMN migration in innate immunity.

2 Materials and Methods

2.1 Materials

2.1.1 Reagents and Kits

Name	Source
2-Mercaptoethanol	Sigma Aldrich
10 % SDS-solution	Applichem
30 % Bis-acrylamidsolution	Applichem
Acetic acid	Applichem
Agarose	Genaxxon
Ammonium chloride (NH_4Cl)	Sigma Aldrich
Ammoniumperoxodisulfate (APS)	Applichem
Ampicillin	AppliChem
Bacto tryptone	Th. Geyer
BD FACS™ lysing solution	BD Bioscience
Bovine serum albumine (BSA)	Sigma Aldrich
Bromphenole blue	AppliChem
β-Estradiol	Sigma Aldrich
Calcium chloride ($CaCl_2$)	AppliChem
Collagen type I, rat tail	IBIDI GmbH
Cortrimoxazol	Ratiopharm
Crystal violet	Sigma Aldrich
Diisopropyl phosphofluoridate (DFP)	Sigma Aldrich
Dimethyl sulfoxide (DMSO)	AppliChem
Dithiothreitol (DTT)	AppliChem
DNeasy Blood & Tissue Kit	QIAGEN
Dulbecco's modified Eagle medium (DMEM)	Biochrom
eBioscience™ Intracellular Fix & Perm Set	Thermo Fisher Scientific
Essential medium (Opti-MEM)	Thermo Fisher Scientific
Ethanol absolute	Th. Geyer
Ethylenediamine-tetraacetic acid (EDTA)	AppliChem
FACS Lysing Solution	BD Bioscience
Foetal calf serum (FCS)	Biochrom
FITC-Dextran	Sigma Aldrich
GeneRuler™ 1 kb DNA ladder	Nippon
GeneRuler™ 100 bp DNA ladder	Nippon
Giemsa's azur eosin methylene blue	Sigma Aldrich
Glucose	AppliChem
Glutaraldehyde solution	Sigma Aldrich
Glycine	AppliChem
Hank's balanced salt solution	Biochrom
HEPES	AppliChem
HISTOPAQUE® 1083	Sigma Aldrich
Hydrochloric acid, 37% (HCl)	AppliChem
In-Fusion® HD Cloning Kit	Clontech - Takara Bio Company

Intracellular Fixation & Permeabilization Buffer Set	eBioscience™
Isopropanol	Merck KGaA
Lipofectamin® Transfection Reagent	Thermo Fisher Scientific
Lipofectamin® 2000 Transfection Reagent	Thermo Fisher Scientific
Magnesium chloride ($MgCl_2$)	AppliChem
May-Grünwald solution	AppliChem
Methanol	Th. Geyer
Midori Green	Nippon
Modified Eagle's minimum	Thermo Fisher Scientific
NucleoBond Xtra Maxi Plus EF	Macherey-Nagel
NucleoSpin Gel and PCR Clean-up	Macherey-Nagel
Odyssey® Blocking Buffer (TBS)	LI-COR Biosciences
PageRuler™ prestained protein ladder	Thermo Fisher Scientific
Paraformaldehyde (PFA) 37%	Sigma Aldrich
Phorbol myristate acetate (PMA)	Merck
PCRBio Rapid Extract PCR Kit	Nippon
Penicillin / Streptomycin (P/S)	Biochrom
Percoll	Sigma Aldrich
Phenol red	Biochrom
Phosphate buffered saline (PBS)	Biochrom
Pn-blebbistatin	Optopharma Ltd.
Poly-L-Lysin	Merck
Ponceau solution	Applichem
Potassium bicarbonate ($KHCO_3$)	Sigma Aldrich
ProLong™ Gold antifade reagent	Thermo Fisher Scientific
Protease inhibitor Mix B	Sigma Aldrich
PureYield™ Plasmid Miniprep System	Promega
Qubit™ Protein Assay Kit	Thermo Fisher Scientific
Roswell Park Memorial Institute 1640 (RPMI) medium	Biochrom
SiR-actin	Spirochrom
Sodium chloride (NaCl)	AppliChem
Sodium dihydrogen carbonate (NaH_2PO_4)	Sigma Aldrich
Sodium dodecyl sulfate (SDS)	AppliChem
Sodium fluoride	Sigma Aldrich
Sodium hydrogen carbonate (Na_2HCO_3)	AppliChem
Sodium orthovanadate	Sigma Aldrich
TEMED	Applichem
TritonX-100	Sigma Aldrich
Trizma base (Tris)	Applichem
Trypsin/EDTA	Biochrom
Tween 20	Sigma Aldrich
Yeast extract	Applichem

2.1.2 Buffers

Name	Ingredients
2x Lämmli-buffer	H_2O_{dest} + 125 mM Tris-HCl pH 6,8 + 4 % SDS + 20 % Glycerol + 10 % 2-Mercaptoethanol + 0,002 % Bromphenol blue
Adhesion medium (ADM)	Hank's balanced salt solution + 1.2 mM Ca^{2+} + 1 mM Mg^{2+} + 0.25 % BSA + 0.1 % Glucose + 20 mM Hepes pH 7.4
Cell lysis buffer	H_2O_{dest} + 25 mM Tris-HCl pH 7.4 + 150 mM NaCl + 0.5 mM EDTA + 1 % TritonX-100 + 1% (w/v) Sodium deoxycholate + 1 mM DTT + 1x Protease inhibitor (Sigma) + 1 mM DFP + 20 mM Sodium fluoride + 2 mM Sodium orthovanadate
Immune fluorescence (IF) antibody staining solution	H_2O_{dest} + 1% (w/v) BSA + 0.1% TritonX-100
IF Perm/Block solution	H_2O_{dest} + 5% (w/v) BSA + 0.3% TritonX-100
Luria broth (LB) medium	H_2O_{dest} + 0.01% (w/v) Bacto tryptone + 0.005% (w/v) Yeast extract + 0.01% (w/v) NaCl pH 7.0
Red blood cell lysis buffer	H_2O_{dest} + 150 mM NH_4Cl + 10 mM $KHCO_3$ + 1 mM EDTA pH 7.2 – 7.4
SDS PAGE running buffer	H_2O_{dest} + 200 mM Glycine + 25 mM Tris + 0.1% (w/v) SDS
TAE buffer	H_2O_{dest} + 40 mM Tris + 20 mM Sodium acetate

	+ 1.25 mM EDTA pH 8.5
TBST	H_2O_{dest} + 20 mM Tris + 137,2 mM NaCl pH 7,6 + 0,1 % Tween
Transfer buffer	H_2O_{dest} + 25 mM Tris + 192 mM Glycine + 20% Methanol
Western Blot (WB) separating gel buffer	H_2O_{dest} + 1,5 M Tris pH 8,8
WB stacking gel buffer	H_2O_{dest} + 0,5 M Tris pH 6,8

2.1.3 Primers and restriction enzymes

Name	5'-3' Sequence
Myh9 genotyping forward (fwd) 1	TGTCATTAGTGTCCTGAGAGCAG
Myh9 genotyping reverse (rev)	CAGGCATGGAGTTTGTGATG
Myh9 genotyping fwd 2	CCTTACCCCAGGTTTCAGGT
Vav-iCre genotyping fwd	GCCTGCCCTCCCTGTGGATGCCACCT
Vav-iCre genotyping rev	GTGGCAGAAGGGGCAGCCACACCATT
Myh9-EGFP In-Fusion cloning fwd	GAATTAGATCGAATTCATGGTGAGCAAGGGCGAG
Myh9-EGFP In-Fusion cloning rev	AATTAGATCTCTCGAGCGCCTATTCAGCTGCCTT
EcoRI	New England Biolabs
XhoI	New England Biolabs

2.1.4 Antibodies

Target	Label	Company	Clone or catalogue number	Isotype	Dilution/Application
Actin		Santa Cruz Biotechnology	I19	Rabbit polyclonal	1:1000 / WB
CD11a	PE	BD Bioscience	2D7	Rat IgG2a	1:100 / Flow cytometry (FC)
CD11b	PE	eBioscience	M1/70	Rat IgG2b	1:200 / FC
CD11c	APC	eBioscience	N418	Armenian Hamster IgG	1:50 / FC

CD18	PE, FITC	BD Bioscience	C71/16	Rat IgG2a	1:100 / FC
CD34	APC	eBioscience	RAM34	Rat IgG2a	1:50 / FC
CD44	Pe-Cy7	eBioscience	IM7	Rat IgG2b	1:400 / FC
CD45.1	AF488	BioLegend	A20	Mouse IgG2a	1:200 / FC
CD45.2	APC/Cy7	BioLegend	104	Mouse IgG2a	1:100 / FC
c-Kit	PerCP-eF710	eBioscience	2B8	Rat IgG2b	1:200 / FC
CXCR2	AF647	BioLegend	TG11	Rat IgG2a	1:50 / FC
F4/80	APC	eBioscience	BM8	Rat IgG2a	1:50 / FC
Flt3	PE	eBioscience	A2F10	Rat IgG2a	1:20 / FC
GAPDH		Merck Millipore	6C5	Mouse IgG_1	1:5000 / WB
GFP		Santa Cruz Biotechnology	FL	Rabbit polyclonal	1:1000 / WB
Gr-1	FITC	BD Bioscience	RB6-8C5	Rat IgG2b	1:50 / FC
Ly6-G	PerCP-eF710	eBioscience	1A8-Ly6g	Rat IgG2a	1:200 / FC
Ly6-G	PE	eBioscience	1A8-Ly6g,	Rat IgG2a	30µg/mouse / laser-induced injury of the ear
Mouse IgG	IRDye® 680RD	LI-COR Biosciences	P/N 925-68072	donkey polyclonal	1:10000 / WB
Mouse IgM	AF488	Thermo Fisher Scientific	A-21042	Goat polyclonal	1:500 / FC
Myh9		BioLegend	Covance MMS-460R H11	Mouse IgM	1:50 / FC
Myh9		Cell Signaling Technology	#3403	Rabbit polyclonal	1:1000 / WB 1:75 / IF
Rabbit IgG	IRDye® 800CW	LI-COR Biosciences	P/N 925-32213	donkey polyclonal	1:10000 / WB
Rabbit IgG	IRDye® 680RD	LI-COR Biosciences	P/N 925-68073	donkey polyclonal	1:10000 / WB
Rabbit IgG	AF546	Thermo Fisher Scientific	A-11071	Goat F(ab')2	1:500 / IF
Rabbit IgG	AF488	Thermo Fisher Scientific	A-11070	Goat F(ab')2	1:500 / IF

2.1.5 Recombinant proteins

Name	Source
Recombinant (r) murine (m) CXCL1	PeproTech
rmICAM-1 without Fc	Stemcell
rmP-selectin with His-tag	Hölzel Diagnostika Handels GmbH
rmTNFα	R&D Systems
mfibrinogen	Innovative Research
rmIL-3	PeproTech
rmIL-6	PeproTech
rmG-CSF	PeproTech
N-formyl-Met-Ile-Val-Ile-Leu (fMIVIL)	JPT Peptide Technologies

2.1.6 Plasmids

Name	Source
pCL-Eco	Hans Häcker; St. Jude Children's Research Hospital, Memphis, USA
pMSCVneo-ER-Hoxb8	Hans Häcker; St. Jude Children's Research Hospital, Memphis, USA
pMSCV-Puro	Hans Häcker; St. Jude Children's Research Hospital, Memphis, USA
pMyosin-IIA-GFP	Addgene plasmid #38297; donated by M. Krummel, University of California San Francisco, USA [160]
pMSCV-Puro-Myosin-II-A-GFP	Self-made

2.1.7 Cell lines

Name	Description	Source
b.End3	Immortalised mouse brain endothelial cell line	ATCC® CRL-2299™
HEK-293T	Immortalised human embryonal kidney cell line	ATCC® CRL-11268™
NIH-3T3	Immortalised murine embryonic fibroblast cell line	DSMZ ACC 59
WEHI-3B	Murine myelomonocytic leukemia cell line producing mIL3	DSMZ ACC 26
Hoxb8-SCF	Immortalised murine progenitor cell line	Self-made
CHO-MGF	Immortalised Chinese hamster ovary cell line producing stem cell factor (SCF)	Hans Häcker; St. Jude Children's Research Hospital, Memphis, USA

2.1.8 Cell culture media

Composition	Applied for
RPMI 1640 + 10% FCS + 1% P/S	WEHI-3B, NIH-3T3, HEK-293T, CHO-MGF
DMEM^{+} GlutaMAX-I + 10% FCS + 1% P/S	b.End3
RPMI 1640 + 10% FCS + 1% P/S + 20% IL-3 containing WEHI-3B supernatant	Murine bone marrow-derived PMN
RPMI 1640 + 15% FCS + 1% P/S + 10 ng/mL rmIL-3 + 20 ng/mL rmIL-6 + 2% SCF-containing supernatant	Bone marrow or embryonic liver progenitor cells (stem cell medium)
RPMI 1640 + 10% FCS + 1% P/S + 4% SCF containing CHO supernatant + 30 µM beta 2-mercaptoethanol + 10 µM β-Estradiol	Hoxb8-SCF cells
RPMI 1640 + 10% FCS + 1% P/S + 4% SCF containing CHO supernatant + 20 ng/ml G-CSF	Hoxb8-SCF differentiation towards PMN
FCS + 10% DMSO	Cryo-conservation

2.1.9 Software

Name	Company
Adobe Photoshop, Illustrator, Acrobat X Pro	Adobe
Chemotaxis and migration tool	IBIDI GmbH
EndNote X7.7	Clarivate Analytics
FACS Diva	BD Biosciences
FlowJo V10	Treestar
Fiji/ImageJ	NIH
Image Studio Lite V5.2	LI-COR Biosciences
LAS X Leica Application Suite	Leica
Microsoft Office	Microsoft Corporation
SigmaPlot 12.5	Systat Software GmbH
Serial Cloner 2.6	Serial Basics
Slidebook 6.0.8	3i Intelligent Imaging Innovations GmbH

2.2 Methods

2.2.1 Mice and Genotyping

In this study, two different strains of mice were crossed to obtain a deletion of Myh9 in the hematopoietic system. *Myh9$^{fl/fl}$* mice (stock no: 36749-JAX[167], The Jackson Laboratory) were bred with *Vav-iCre^{+}* mice (stock no: 018968[179], The Jackson Laboratory) to receive *Vav-iCre^{+}/Myh9$^{wt/fl}$* mice. Subsequently, *Vav-iCre^{+}/Myh9$^{wt/fl}$* mice were backcrossed to *Myh9$^{fl/fl}$* mice to generate *Vav-iCre^{+}/Myh9$^{wt/fl}$* and *Vav-iCre^{+}/Myh9$^{fl/fl}$* target animals as well as *Vav-iCre^{-}/Myh9$^{wt/fl}$* and *Vav-iCre^{-}/Myh9$^{fl/fl}$* littermate controls. These mice were bred and housed under specific pathogen-free conditions and both male and female mice from the age of 8 weeks were used in the experiments. Animal experiments were conducted in accordance with German federal animal protection laws and were approved by the Bavarian Government (Regierung von Oberbayern, Munich, Germany)[180].

To analyse the genotype of the mice, DNA was extracted from ear biopsies using the PCRBio Rapid Extract PCR Kit and genotyping PCRs were performed according to manufacturer's protocol. Here, the primers Myh9 genotyping fwd 1 and Myh9 genotyping rev were applied to distinguish, on the basis of different sizes of the PCR products, between wildtype (*Myh9^{wt}*) and floxed exon1 of Myh9 (*Myh9^{fl}*) alleles. To identify *Vav-iCre^{+}* mice, the presence, or for *Vav-iCre^{-}* mice, the absence, of a PCR product with the genotyping primers Vav-iCre genotyping fwd and Vav-iCre genotyping rev was documented. To further characterise the Myh9 gene locus in Hoxb8-SCF cells, an additional genotyping PCR was performed. A new Myh9 forward primer - Myh9 genotyping fwd 2 - was employed, along with the Myh9 genotyping rev primer. This strategy allowed the discrimination between *Myh9^{wt}* and *Myh9^{fl}* alleles as well as Myh9 with a deleted exon 1 (*Myh9^{del}*). The positions of the Myh9 primers around exon 1 of Myh9 are illustrated in Fig. 4. The PCR protocols started with an initial denaturation step at 95°C for 3 min, followed by a 33 times repeated loop including denaturation for 15 s at 95°C, annealing for 15 s at 60°C for Myh9 primers and 65°C for Vav-iCre primers, and elongation at 72°C for 30 s for Myh9 genotyping fwd 1 and Myh9 genotyping rev primers, 2 min for Myh9 genotyping fwd 2 and Myh9 genotyping rev primers, and 1 min for Vav-iCre primers. A final elongation step at 72°C for 2 min ended the PCR protocol. Using gel electrophoresis in a 1.5% agarose gel in TAE buffer, the DNA fragments were separated according to their size and visualized with the help of Midori green and UV light. The usage of a DNA ladder allowed the determination of the actual band sizes, with 800 bp for *Vav-iCre^{+}* and no band for *Vav-iCre^{-}*, 350 bp for *Myh9^{wt}* or 480 bp for *Myh9^{fl}* in

the original genotyping PCR and 1800 bp for *Myh9*^{wt}, 2000 bp for *Myh9*^{fl} or 240 bp *Myh9*^{del} in the additional genotyping PCR.

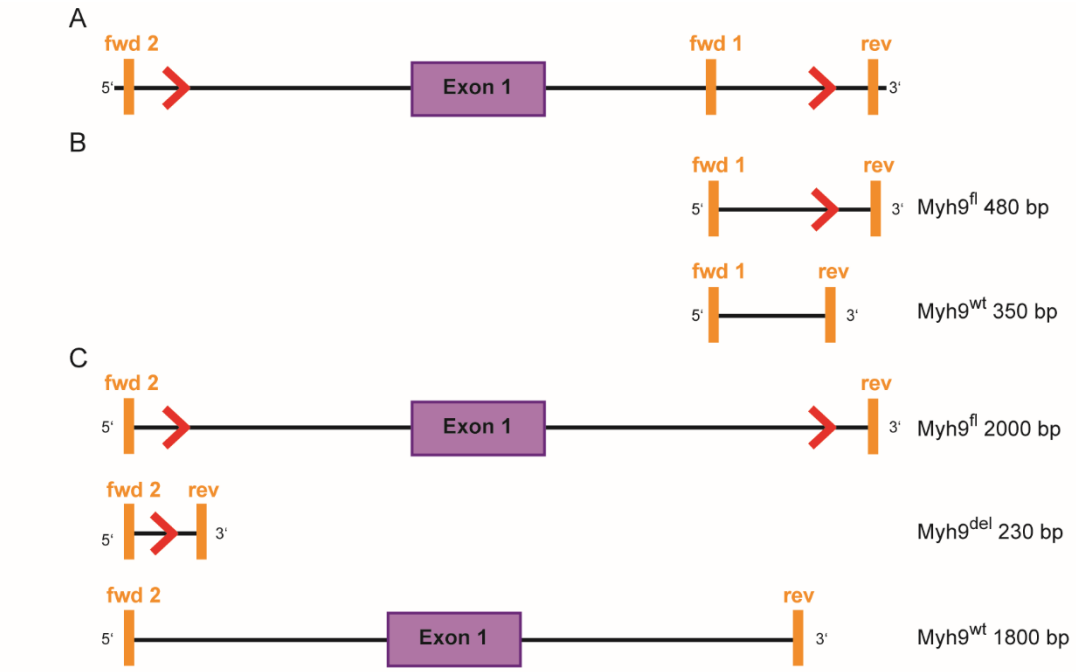

Figure 4. Schematic representation of *Myh9*^{fl} allele and genotyping PCR products. Purple box indicates the exon 1 of Myh9. Red arrows display the location of flox sites and orange boxes represent the 2 different fwd primers Myh9 genotyping forward (fwd) 1 and 2, and the location of the Myh9 genotyping reverse (rev) primer. These primers were used to distinguish between *Myh9*^{fl}, *Myh9*^{wt}, and *Myh9*^{del} DNA according to specific lengths of the PCR products. Schematic representation of **(A)** the Myh9^{fl} allele, **(B)** the PCR products for the original genotyping PCR using the primers fwd1 and rev and **(C)** the PCR products for the additional genotyping PCR using the primers fwd2 and rev.

2.2.2 Cell culture

All cell lines were cultured in their appropriate media at 37°C, 5% CO_2 and 95% air humidity to ensure optimal growth conditions. With the exception of the Hoxb8-SCF cells, all other cell lines had an adherent phenotype and were sub-cultured once they reached 90% confluence. To detach the cells, Trypsin/EDTA was applied and a portion of the cells was transferred to a new culture dish with fresh culture medium. To produce SCF containing supernatant from CHO-MGF cells or IL-3 containing supernatant from WEHI-3B cells, these cells were allowed to grow in 100% confluence for 2 days (d) before the medium was collected. Hoxb8-SCF cells were grown in suspension and were sub-cultured by transferring a portion of the cell suspension into a cell culture flask with fresh culture medium. For long term storage, adherent cells after detachment or cells in suspension were pelleted at 300 x g, resuspended in

freezing medium at 2 x 10^6 cells per mL and aliquoted into cryotubes. These were cooled down to -80°C in a NALGENE™ Cryo 1°C freezing container (Thermo Fisher Scientific) before the transfer to liquid nitrogen. To re-cultivate cells, a 37°C water-bath was employed to quickly thaw the cells before uptake in fresh culture medium. To wash out residual DMSO, the cells were centrifuged at 300 x g and transferred into a new cell culture flask with fresh culture medium. Determination of exact cell numbers is crucial for all *in vitro* assays. Here, trypan blue staining was used to discriminate between live and dead cells and cell numbers were calculated using a Neubauer counting chamber (Th. Geyer).

2.2.3 Isolation of murine bone marrow PMN

PMN were isolated by flushing out bone marrow cells from tibia, femur and humerus of mice with PBS and loading of the obtained cells onto a discontinuous Percoll density gradient (52% / 64% / 72%), followed by centrifugation at 1000 x g for 30 min without break. Due to their specific density, PMN could be collected from the interphase between 64% and 72% Percoll and were cultivated for 24 hours (h) in RPMI 1640 supplemented with 20% WEHI-3B-conditioned medium[180,181].

2.2.4 Pharmacological inhibition of Myh9

In this study, para-nitro blebbistatin (pn-blebbistatin) was used to inhibit NMII activity pharmacologically. Prior to the experiment, murine bone marrow-derived PMN were incubated with 1 µM, 5 µM, 15 µM, 25 µM or 50 µM pn-blebbistatin at 37°C for 30 min. The indicated concentrations of pn-blebbistatin were also applied during the entire duration of the assays to prevent a wash-out of the inhibitor[180].

2.2.5 Generation and differentiation of Hoxb8-SCF cells

In the first step of Hoxb8-SCF cell generation, a retrovirus encoding for the fusion protein of an estrogen responsive element (ER) and Hoxb8 was produced. Here, HEK-293T cells were grown to 90% confluency in a 10 cm^2 dish and transfected with 8 µg of the retroviral backbone pMSCVneo-ER-Hoxb8 as well as the ecotropic packaging vector pCL-Eco using Lipofectamin® 2000. The retrovirus containing supernatant was harvested 48 h post transfection, aliquoted, and stored at -80°C for later usage. To verify the amount of infectious virus particles in the supernatant, the colony forming units (cfu)/mL of the virus were assessed by titration using NIH3T3 cells. In the second step of the Hoxb8-SCF cell generation, bone marrow progenitor cells or foetal liver progenitor cells were transduced with

the ER-Hoxb8 encoding retrovirus. Bone marrow cells from the tibia of 8 - 10 week old mice or E13 foetal liver cells were harvested using PBS + 1% FCS. Progenitor cells were enriched by centrifugation for 30 min at 400 x g without break using HISTOPAQUE® 1083. At the interphase between PBS and the HISTOPAQUE® 1083, mononuclear cells were harvested, and progenitor cells were stimulated to proliferate by culture in 10 mL stem cell medium for 3 d at a starting concentration of 5 x 10^5 cells/mL. These stimulated progenitor cells were transduced with the ER-Hoxb8 encoding retrovirus at a multiplicity of infection of 10 by spinoculation for 80 min at 1500 x g with the help of Lipofectamin® in a final dilution of 1:1000 in Hoxb8-SCF medium. The Hoxb8-SCF cell line was established after 4 weeks by continuous sub-culture in Hoxb8-SCF medium.

To accomplish differentiation of Hoxb8-SCF cells into PMN, 2.5 x 10^5 cells were washed in PBS and were allowed to grow in 10 mL differentiation medium in a 10 cm^2 culture dish for 4 d[180].

2.2.6 Generation of Myh9-EGFP expressing Hoxb8-SCF cells

To generate Myh9-EGFP expressing Hoxb8-SCF cells, cells were transduced with a retrovirus encoding for Myh9-EGFP and a puromycin resistance: First, the coding region of Myosin-IIA-GFP was cloned into the retroviral backbone pMSCV-Puro using the In-Fusion® HD Cloning Kit. The underlying cloning method is ligation independent and based on annealing of 15 bp long complementary overlaps of a cloning insert and the linearized cloning vector. Here, the homologous overlaps were generated by PCR amplification of the Myh9-EGFP locus using the specifically designed primers Myh9-EGFP In-Fusion cloning fwd and rev. The In-Fusion® enzyme mix generated 15 bp single stranded 5' overhangs at the termini of the cloning insert and the linearized vector. These overhangs annealed at the sites of complementarity, and the recombinant circular construct was rescued in Stellar competent E. coli cells[182]. In a second step, retrovirus encoding for Myh9-EGFP and a puromycin resistance was produced in HEK-293T cell using the generated pMSCV-Puro-Myosin-II-A-GFP and the ecotropic packaging vector pCL-Eco. Virus-containing supernatant was harvested 48 h post transfection, and *Vav-iCre$^+$/Myh9$^{fl/fl}$* foetal liver Hoxb8-SCF cells were transduced by spinoculation. After 72 h of transduction 10 µg/mL puromycin was added to the cell culture medium to select for puromycin resistant cells. The puromycin resistant cells where further analysed for their expression of EGFP and EGFP^{high} Hoxb8-SCF cells were sorted using a MoFlo Astrios cell sorter (Beckman Coulter). In the last step of the generation of Myh9-EGFP expressing Hoxb8-SCF cells, the expression of the Myh9-EGFP

fusion protein in *Vav-iCre*$^{+}$*/Myh9*$^{fl/fl}$ foetal liver Hoxb8-SCF cells was confirmed using western blotting and flow cytometry[180].

2.2.7 Western blotting

To analyse protein expression using western blot, cells were lysed at a concentration of 1 x 10^7 per 300 µL in cell lysis buffer for 30 min at 4°C. Subsequent centrifugation at 1500 x g for 5 min ensured that the cell debris was separated from the proteins in suspension. The protein concentration was determined using the Qubit™ Protein Assay Kit. To denature and reduce the proteins, the samples were incubated for 7 min at 97°C in 2x Lämmli-buffer. For separation of proteins on the basis of their molecular weight and charge, total protein lysates were run on SDS-PAGEs. In this study, polyacrylamide gels with 8% separating and 4% stacking gels were used, and proteins were separated by electrophoresis using 80 Volt and 120 Volt. Transfer of proteins onto nitrocellulose membranes was carried out by semi-dry blotting at 0.08 Ampere for 2 h. After blocking of the membrane with Odyssey® blocking buffer for 1 h, the membranes were incubated overnight (o.n.) at 4°C with a specific primary antibody in a 1:1 TBST/Odyssey® blocking buffer solution. Membranes were incubated for 1 h with near-infrared labelled secondary antibodies to enable detection at the Odyssey® CLx Imaging system[180].

2.2.8 Flow cytometry

Upregulation of integrins after stimulation was evaluated in Hoxb8-SCF cells using flow cytometry and specific fluorescence-labelled antibodies. Cells (2.5 x 10^5 per sample) were incubated with 100 ng/mL rmTNFα, 100 ng/mL rmCXCL1, 100 nM PMA or 100 nM N-formyl-Met-Ile-Val-Ile-Leu (fMIVIL) [183] or PBS for control for 20 min at 37°C before application of the indicated antibodies or corresponding isotype controls for 30 min on ice in PBS supplemented with 1% FCS. Labelled cells were kept on ice and acquired immediately after washing on a FACSCanto II or a LSRFortessa flow cytometer (BD Bioscience). For analysis of extracellular markers on murine blood PMN, the antibody solution was directly added to 50 µL whole blood taken from the vena maxillaris and vena temporalis superficiali and incubated for 30 min at 4°C. Red blood cells were removed by adding 1 mL FACS Lysing Solution and incubation for 10 min on ice. For detection of intracellular Myh9, the eBioscience™ Intracellular Fixation & Permeabilization Buffer Set was applied. Hoxb8-SCF cells (5 x 10^5) were fixed in 100 µL fixing solution at room temperature (RT) for 20 min. After washing with PBS, the cells were incubated with 1 mL permeabilization buffer for

10 min at RT, followed by 30 min incubation of the Myh9 specific primary antibody in 50 µL permeabilization buffer on ice. The adequate AF488-labelled anti-mouse IgM secondary antibody was subsequently incubated with the cells in 50 µL perm buffer on ice, before acquisition of cells on the flow cytometer. Fluorescence intensities were measured, and mean fluorescence intensities and histograms were determined using FlowJo V10 software, after exclusion of dead cells before gating on the target population[180].

2.2.9 Microscopy

2.2.9.1 May-Grünwald-Giemsa staining

For May-Grünwald-Giemsa staining, cytospins of Hoxb8-SCF cells and murine bone marrow-derived PMN (1 x 10^5 cells) were stained with the May-Grünwald solution for 3 min and subsequently stained with a 12% Giemsa solution for 20 min. Microscopy was conducted after drying of the samples o.n. using a 63x/1.4NA oil immersion objective (Leica)[180].

2.2.9.2 Confocal microscopy

Subcellular distribution of Myh9 and F-actin in transfected HEK-293T cells was analysed using confocal microscopy. HEK-293T cells were grown to 90% confluence *in vitro* on a gelatine-treated cover slip before fixation with 4% PFA in PBS for 10 min on RT, treatment with IF Perm/Block solution for 1 h at RT and incubation with the primary anti-Myh9 antibody and 100 nM SiR-actin (Spirochrome) in IF antibody staining solution o.n. at 4°C. After washing with PBS, the secondary anti-rabbit AF546-labelled antibody was applied to the coverslips for 1 h before mounting of the samples using ProLong™ Gold antifade reagent[180]. Images were taken using a Leica SP8X WLL confocal microscope equipped with a 63x/1.40 oil immersion objective (Leica) and analysed offline using LAS X software and Fiji/ImageJ.

2.2.9.3 Stimulated emission depletion (STED) nanoscopy

For the identification of the subcellular localisation of Myh9 and F-actin in PMN isolated from *Vav-iCre$^+$/Myh9$^{wt/fl}$* (*Myh9-cHet*) and *Vav-iCre$^-$/Myh9$^{wt/fl}$* (*control*) mice, STED nanoscopy was used. Here, PMN were stimulated and allowed to adhere by exposure to a glass surface coated with 3 µg/mL rmICAM-1 and 5 µg/mL rmCXCL1 for 10 min in an IBIDI 12 well chamber. Fixation and staining of PMN was conducted as described for HEK-293T cells. Here, the anti-rabbit AF488-labelled secondary antibody was used to visualise Myh9. Samples were mounted using ProLong™ Gold antifade reagent and images

were taken using sequential recording at a Leica TCS SP8X WLL STED microscope equipped with a 100x/1.4NA oil immersion objective and depletion in xy direction at 592 nm and 775 nm[180]. Images were analysed offline using LAS X software and Fiji/ImageJ. Quantification of the subcellular localisation of Myh9 and F-actin in *Myh9-cHet* and *control* PMN was performed by splitting the area of the cells equally into two parts, the front and the back of the cell. Myh9 and F-actin distribution to the front or the back of the cell was determined by taking the sum of intensity values of the whole cell area and calculating the ratio between this value and the sum of intensity values of the front or the back of the cell. To determine the spatial correlation between F-actin and Myh9, a randomization approach using the nearest-neighbour analysis was performed with the MosacIA Fiji plugin to calculate the interaction potentials[184,185]. Potential used was Plummer (10 iterations). Grid spacing was 0.5 pixels. Kernel wt(q) was 0.001. Kernel wt(p) was provided by the plugin using Silverman's rule. Interaction strength > 0 indicated that the spatial distribution of F-actin was dependent on the spatial distribution of Myh9. The results were tested for significance against 1,000 Monte Carlo samples of point distributions corresponding to the null hypothesis of 'no interaction'. Quantification of the interaction strength was performed using only results, which were considered statistically significant ($p < 0.05$)[180].

2.2.9.4 Live cell imaging using spinning disk confocal microscopy

Subcellular localisation of Myh9-EGFP was analysed in real-time in Myh9-EGFP expressing *Myh9-RES* Hoxb8-SCF cell derived neutrophils (dHoxb8 cells), during chemotactic migration within a 1.5 mg/mL collagen network towards a rmCXCL1 gradient, as described in the section 3D chemotaxis. For this purpose, an upright spinning disk confocal microscope (Examiner, Zeiss) equipped with a confocal scanner unit CSU-X1 (Yokogawa Electric Corporation), an Evolve 512 EMCCD camera (Photometrics) and a 20x/0.75NA water immersion objective (Plan Apochromat, Zeiss) was employed. Images were acquired using a laser with an excitation wavelength of 488 nm. Data was analysed offline using Slidebook 6.0.8 Software and Fiji/ImageJ[180]. The area of the cell was equally split into two parts, the front and the back of the cell. Myh9 distribution to the front or the back of the cell was determined as described in the section above.

2.2.10 Adhesion under static conditions

Hoxb8-SCF cells were plated in triplicates in ADM at 1 x 10^5 cells per well in a 96-well microtiter plate. Wells were either coated with rmICAM-1 (3 µg/mL) or mfibrinogen

(50 µg/mL) o.n. at 4 °C. Cells were allowed to adhere for 5 min and stimulated for 5 min with 100 ng/mL rmTNFα, 100 ng/mL rmCXCL1, 100 nM PMA and 100 nM fMIVIL (final concentrations) or left untreated for negative control. Non-adherent cells were washed away, and adherent cells were fixed with 1% glutaraldehyde in PBS. After drying, cells were stained with 0.1% crystal violet in PBS and lysed using 10% acetic acid in H_2O[103]. Absorption was measured at 590 nm with a microplate reader (TECAN). All samples were normalized to the untreated control cells (100% = 1) and fold change of adhesion was displayed[180].

2.2.11 Adhesion under flow conditions

To study induction of adhesion under flow conditions of murine bone marrow-derived PMN and dHoxb8 cells IBIDI µ-Slide VI 0.1 flow chambers were coated o.n. at 4°C with 10 µg/mL rmP-selectin for PMN and 5 µg/mL rmP-selectin for dHoxb8 cells, 3 µg/mL rmICAM-1, and 5 µg/mL rmCXCL1. Cells (7.5 x 10^5/mL) in ADM were perfused into the channels for 9 min at a constant shear stress of 1 dyne/cm^2. An Axiovert 200M microscope equipped with a Plan-Apochromat 20×/0.75NA objective, AxioCam HR digital camera, and a temperature-controlled environmental chamber (Zeiss) were used, and time-lapse videos were recorded from 18 different points of view. The number of rolling and adherent cells after 1, 3, 5, 7 and 9 min was determined offline using Fiji/ImageJ as described previously[180,186,187].

2.2.12 Spreading and polarisation

Spreading and polarisation of murine bone marrow-derived PMN were studied in IBIDI µ-Slide VI 0.1 flow chambers coated with rmICAM-1 (3 µg/mL) and rmCXCL1 (5 µg/mL) as described previously[180,186,187]. The PMN (4 x 10^5/sample) in ADM were perfused into the channels and allowed to adhere for 10 min under static conditions. Pictures were taken with the above described microscope set-up and analysed offline using Fiji/ImageJ by measuring the cell area and circularity.

2.2.13 2D mechanotaxis

Mechanotactic crawling under shear stress of murine bone marrow-derived PMN and dHoxb8 cells was studied in IBIDI µ-Slide VI 0.1 flow chambers coated with rmICAM-1 (3 µg/mL) and rmCXCL1 (5 µg/mL). The chambers were perfused with PMN or dHoxb8 cells in ADM (4 x 10^5/sample) and allowed to adhere for 10 min (PMN) or 5 min (dHoxb8 cells). Shear stress of 1 dyne/cm^2 was applied for 10 min and time-lapse videos with a time interval of 5 s were recorded of one field of view with the microscope set-up described in the section

adhesion under flow conditions[187]. Migration tracks were analysed offline with the ImageJ software and its implemented manual tracking plugin (Fabrice Cordeliès, Institute Curie, France)[186]. Single cell migration tracks rose plots and migration parameter were obtained using the IBIDI chemotaxis and migration tool[180].

2.2.14 Adhesion strengthening

Adhesion strengthening of murine bone marrow-derived PMN was analysed using increasing shear stress rates in IBIDI µ-Slide VI 0.1 flow chambers coated with rmICAM-1 (3 µg/mL) and rmCXCL1 (5 µg/mL) as described previously[186,188]. Before onset of shear stress, PMN (4 x 10^5/sample) in ADM were allowed to adhere for 10 min. Shear stress was increased every 90 s, starting from 0.5 dyne/cm^2 up to 8.0 dyne/cm^2. The cells that remained adherent during the observation period were counted and relative adhesion was quantified as percent of adherent cells prior to the onset of shear stress (100%)[180].

2.2.15 2D chemotaxis

Chemotactic behaviour of dHoxb8 cells was investigated in a Zigmond chamber as described previously[104,189]. Glass coverslips were coated with rmICAM-1 (12.5 µg/mL) o.n. at 4 °C, blocked with 10 % casein at RT for 2 h and washed with PBS. Cells (4 x 10^5 per sample) in 50 µL ADM were applied to the coverslip and allowed to adhere for 10 min at 37°C. Coverslips were placed and fixed onto the Zigmond slide. To generate a chemotactic gradient, ADM supplemented with 100 ng/mL mCXCL1 was applied to one side of the Zigmond chamber. After stabilisation of the gradient for 10 min, time-lapse videos with a time interval of 5 s were recorded for 10 min using the above described microscope set-up[187]. Single cell migration tracks rose plots, and the associated cell migration parameters were determined offline using Fiji/ImageJ and the IBIDI chemotaxis and migration tool[180].

2.2.16 Transwell migration assay

Analysis of transmigration *in vitro* was performed using transwell polycarbonate filters (Corning) with a pore size of 3 µm or 8 µm, as described previously[187,190]. Triplicates of murine bone marrow-derived PMN (2.5 x 10^5/sample for 3 µm pore size and 5 x 10^5/sample for 8 µm pore size) were seeded in 100 µL ADM in the upper compartment of the chamber. The lower compartment of the system contained ADM and rmCXCL1 (100 ng/mL) or ADM alone for control. In the first set of experiments, rmICAM-1 (3 µg/mL) coated filters, with a pore size of 3 µm, were used and PMN were allowed to migrate for 70 min. Here,

transmigrated PMN were quantified on a FACSCanto II or LSRFortessa (BD Bioscience) on the basis of a standard curve consisting of a dilution of PMN ranging from 2.5 x 10^5 cells (100%) to 2.5 x 10^3 cells (1%). The samples where further normalized to the transmigrated control cells in the presence of rmCXCL1 (100%). In a second set of experiments, brain-derived b.End3 endothelial cells were seeded in the upper compartment of chambers with filters displaying 8 µm pore size. After 2 d of seeding, the b.End.3 endothelial cells had formed a monolayer and were equilibrated for 30 min before PMN were added and allowed to transmigrate for 45 min at 37 °C. Here, the transmigrated PMN were collected and counted using a Neubauer counting chamber and trypan blue staining. The samples where normalized to the transmigrated control cells in the presence of rmCXCL1 (100%)[180].

2.2.17 3D chemotaxis

The analysis of migration in collagen gels was performed in IBIDI µ-Slides Chemotaxis 3D chambers as previously described[187,190]. For a 1.5 mg/mL collagen gel, a gel-cell mixture with murine bone marrow-derived PMN or dHoxb8 cells (3 x 10^5) in 5 µL ADM was prepared by mixing cells with 2 µL 10 x ADM, 8.5 µL H_2O, 0.4 µL $NaHCO_3$, and 9 µL (5 mg/mL) type I rat tail collagen. The PMN/collagen solution was applied to the middle channel of the 3D chamber and left at 37°C for 5 min for gelation. After application of 100 ng/mL rmCXCL1 in ADM to one reservoir of the chamber and incubation for 20 min at 37°C, time-lapse videos were recorded for the length of 10 min with a frame rate of 14 s using a Plan-Apochromat 10×/0.3NA objective and the above described microscope set-up[180]. Migration was analysed offline using Fiji/ImageJ. Cell migration tracks and rose plots were generated using the IBIDI chemotaxis and migration tool.

2.2.18 Laser-induced injury of the ear

Extravasation and interstitial migration of PMN during sterile inflammation was investigated by two-photon microscopy using a laser-induced injury model of the ear dermis of mice, as described previously[180,191]. After intraperitoneal application of anaesthesia consisting of Medetomidine (0.5 µg/g body weight), Midazolam 5 µg/g and Fentanyl 0.05 µg/g in 0.5 mL NaCl, the ears of *Vav-iCre$^+$/Myh9$^{wt/fl}$* (*Myh9-cHet*) mice and *Vav-iCre$^-$/Myh9$^{wt/fl}$* (*control*) mice were fixed on a custom build stage. A tail vein catheter was used to apply PE-labelled anti-Ly6G (30 µg, 1A8-Ly6g, eBioscience) and FITC-dextran (20 µg, 2MD, Thermo Fisher Scientific). Focusing the laser beam on the ear in a field of 40 µm x 40 µm until autofluorescence appeared led to a single necrotic lesion [192,193]. Images were acquired using a

TrimScope II (LaVision Biotech) connected to an upright microscope with a 20x/0.95W water immersion objective (Olympus), excitation at 800 nm, the emission filters 525/50 and 605/70 and second harmonics. The size of the field of view was 554 µm x 554 µm and a frame rate of 30 s and a z-step size of 3 µm in a total range of 30 µm (20-50 µm below the epidermis) were chosen[180]. Quantification of interstitial migration velocity and Euclidean distance during the observation time was achieved offline by manual tracking using Fiji/ImageJ and the IBIDI chemotaxis and migration tool. Extravasation of PMN was evaluated over time, starting immediately after injury, up to 40 min. Extravascular PE intensities within a circular area of interest, defined by the border of the laser injury to the border of the nearest vessel, were measured. Quantification was performed by calculating the fold change of the sum of intensity values relative to the background intensity immediately after injury[180]. Leukocyte counts were determined from whole blood of the vena maxillaris and vena temporalis superficialis using an IDEXX ProCyte DxTM hematology analyser (IDEXX Laboratories).

2.2.19 CXCL1-induced peritonitis model

To induce peritonitis and the extravasation of PMN into the peritoneal cavity, *Myh9-cHet* and *control* mice or bone marrow chimeras (as described below) were injected intraperitoneally with 300 ng rmCXCL1 or 0.9% NaCl for negative control. After 4 h, mice were sacrificed, and the peritoneal cavity was flushed with 5 mL ice cold 0.9% NaCl, as described previously[180,187,190]. The number of extravasated PMN in the lavage was detected using an IDEXX ProCyte DxTM hematology analyser (IDEXX Laboratories).

2.2.20 Bone marrow chimeras

The congenic marker system CD45.1/2 was used for the generation of the bone marrow chimeras to enable discrimination of *control* and *Myh9-cHet* derived leukocytes[194,195]. CD45.1 wildtype recipient mice were irradiated twice in an interval of 4 h with 6 Gy for 3 min. Bone marrow cells from CD45.1 wildtype and CD45.2 *Myh9-cHet* mice were harvested and a total of 10×10^6 cells per mouse were injected via tail vein into the lethally irradiated recipients. To prevent infections, Cortrimoxazol was given 2 d before irradiation until 4 weeks after transplantation. Three different chimeric models were generated (donor → recipient): CD45.1 wildtype → CD45.1 wildtype (WT→WT); CD45.2 *Myh9-cHet* → CD45.1 wildtype (HET→WT) and CD45.1 wildtype / CD45.2 *Myh9-cHet* (1:1 ratio) → CD45.1 wildtype (MIX→WT)[180].

2.2.21 Statistics

Data shown represent means ± SEM and are representative or compiled from at least 3 independent experiments as indicated. Statistical significance was performed using Sigma Plot 12.5. For pairwise comparison the Student t-test, for multiple comparisons, one way ANOVA with the Holm Sidak method or the Dunnett's method, was applied. A p-value < 0.05 was considered significant[180].

3 Results

Major parts of the following data is published in "A fundamental role of Myh9 for neutrophil migration in innate immunity" by Zehrer et al. in the Journal of Immunology[180].

3.1 Effect of pharmacological inhibition of class II non-muscle myosin on PMN trafficking

To study the effect of pharmacological inhibition of class II non-muscle myosin (NMII) activity on distinct steps in the recruiting cascade of PMN para-nitro blebbistatin (pn-blebbistatin), an inhibitor of NMII activity, was used. First, the ability of PMN to roll and adhere on a 2D surface was analysed under shear stress of 1 dyne/cm^2 (Fig. 5A). This shear rate mimics the situation *in vivo* representing the physiological flow in postcapillary venules. Over the time course of 9 min, the number of rolling and adherent cells on rmICAM-1, rmP-selectin and rmCXCL1 was determined and was found to be similar between pn-blebbistatin- and DMSO-treated control PMN: After 9 min, 129 ± 26 rolling and 495 ± 35 adherent PMN for DMSO- and 119 ± 26 rolling and 413 ± 29 adherent PMN for pn-blebbistatin-treated PMN were identified, indicating that NMIIA activity is dispensable for the process of induction of adhesion under flow conditions.

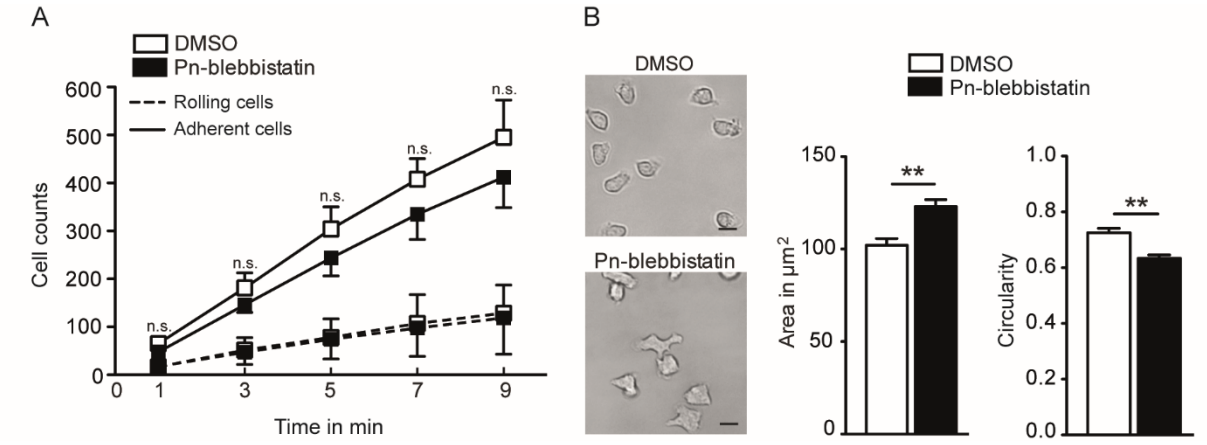

Figure 5. Pn-blebbistatin treatment of murine bone marrow-derived PMN does not affect induction of adhesion but the shape of adherent cells. (A) Numbers of rolling and adherent cells of DMSO- or pn-blebbistatin-treated PMN under 1 dyne/cm^2 of flow on immobilised rmP-selectin, rmICAM-1 and rmCXCL1 at indicated time points. **(B)** Representative images of adherent PMN. Cell shape descriptors determined after 10 min of exposure to immobilised rmICAM-1 and rmCXCL1. Cell area and circularity was calculated from 223 DMSO-treated PMN and 275 pn-blebbistatin-treated PMN from 4 independent experiments. Scale bar, 10 µm. Mean ± SEM n = 5. n.s., not significant, DMSO- versus pn-blebbistatin-treated adherent PMN (adapted from Zehrer et al., 2018[180]).

During the spreading of PMN and the establishment of polarity a striking difference in morphology was observed between the two treatments. The pn-blebbistatin-treated PMN displayed for PMN atypical multiple protrusions. Quantitative analysis revealed that DMSO-treated PMN had a cell area of 103 ± 3.6 μm^2 compared to a significantly increased cell area of 123 ± 3.7 μm^2 for pn-blebbistatin-treated PMN. Additionally, a significant decrease in circularity from 0.73 ± 0.02 µm in control PMN to 0.63 73 ± 0.01 µm after pn-blebbistatin treatment was observed (Fig. 5B).

Subsequent to induction of adhesion and spreading, the ability to migrate under flow conditions is of major importance for PMN as it enables them to reach suitable extravasation sites from the vessel into the inflamed tissue. It was previously reported that the concentration of blebbistatin influences the migration speed of different cell types such as endothelial cells or monocytes in a dose-dependent manner[196]. In this study, the influence of increasing concentrations of pn-blebbistatin on the migration behaviour of PMN was analysed. Pn-blebbistatin was applied to PMN in concentrations from 0 - 50 µM and the effect on migration velocity was monitored during migration on immobilised rmICAM-1 and rmCXCL1 under flow conditions (Fig. 6A). The results revealed a concentration dependence of migration velocity in pn-blebbistatin-treated PMN. Higher pn-blebbistatin concentrations led to lower values in migration velocity with the slowest migrating PMN at 50 µM pn-blebbistatin with 4.3 ± 0.17 µm/min, compared to the control PMN with 9.4 ± 0.68 µm/min migration velocity (Fig. 6A). Further analysis was carried out for PMN treated with 50 µM pn-blebbistatin, to evaluate in detail the migration behaviour of pn-bebbistatin- versus DMSO-treated PMN under flow conditions (Fig. 6 B-D). Time-lapse images of recorded videos revealed an elongated uropod, which the cells could hardly retract, in pn-blebbistatin-treated PMN (Fig. 6B). Interestingly, this phenotype did not occur when PMN were treated with 1 µM pn-blebbistatin, occurred in around half of the imaged PMN when treated with 5 µM pn-blebbistatin, and higher concentrations caused this phenotype in all PMN (data not shown). Comparison of single cell migration tracks of PMN treated with pn-blebbistatin (50 µM) or DMSO (Fig. 6C) and quantitative evaluation of the accumulated distance and the Euclidean distance further elucidated the diminished migratory capacity of the pn-blebbitatin-treated PMN (Fig. 6D). Specifically, the accumulated distance was significantly reduced from 94.6 ± 6.8 µm in DMSO-treated PMN to 43.4 ± 1.7 µm in pn-blebbitatin-treated PMN. Euclidean distance was significantly reduced from 51.7 ± 4.0 µm in DMSO-treated PMN to

26.4 ± 0.8 µm in pn-blebbistatin-treated PMN. Thus, pn-blebbistatin-treated PMN exhibited a severe migration defect under flow conditions compared to control PMN.

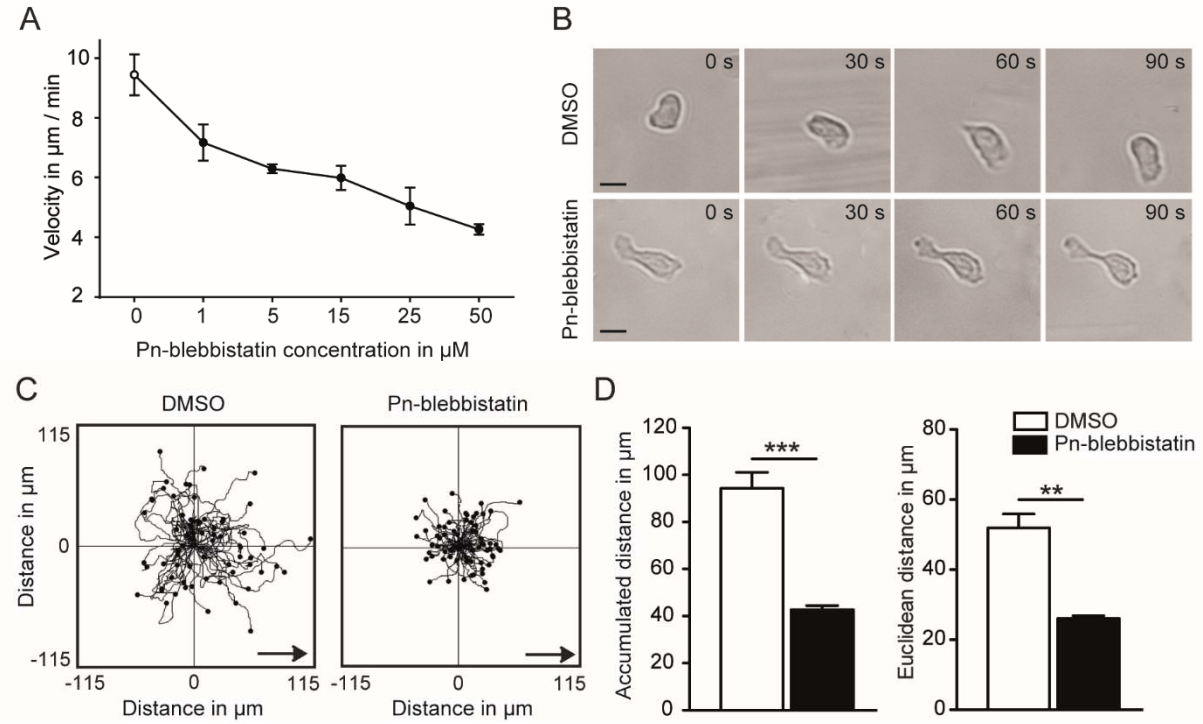

Figure 6. Mechanotactic migration is compromised in murine bone marrow-derived PMN treated with pn-blebbistatin. 1 dyne/cm^2 of shear stress was applied to PMN in microflow chambers coated with immobilised rmICAM-1 and rmCXCL1. **(A)** Velocity of PMN treated with 0, 1, 5, 15, 25 and 50 µM pn-blebbistatin; n = 3 **(B)** Representative time-lapse images of migrating DMSO- or pn-blebbistatin-treated PMN under shear stress at indicated time points. Scale bar, 10 µm. **(C)** Representative single cell migration tracks documented over 10 min. Arrows indicate direction of flow. **(D)** Accumulated and Euclidean distance. n = 4 (with a total of 422 DMSO-treated PMN and 563 pn-blebbistatin-treated PMN). Mean ± SEM, ** $p < 0.01$, *** $p < 0.001$ (adapted from Zehrer et al., 2018[180]).

To investigate whether the inhibition of NMIIA activity could also affect the transmigration of PMN, pn-blebbistatin-treated or DMSO-treated control PMN were permitted to migrate through a membrane with 3 µm pores towards the chemoattractant rmCXCL1 *in vitro* (Fig. 7). In the case of DMSO treatment, when no stimulus was present, 23 ± 5% of control PMN migrated through the pores. Upon application of the chemoattractant the number of transmigrated PMN increased notably (100%) (Fig. 7). This was in strong contrast to the pn-blebbistatin-treated cells where 4.5 ± 0.7% of the PMN transmigrated with or without the presence of the chemoattractant in the lower compartment of the transmigration chamber. This experiment demonstrated that the transmigration of pn-blebbistatin-treated PMN was significantly decreased compared to control cells, especially in the presence of rmCXCL1.

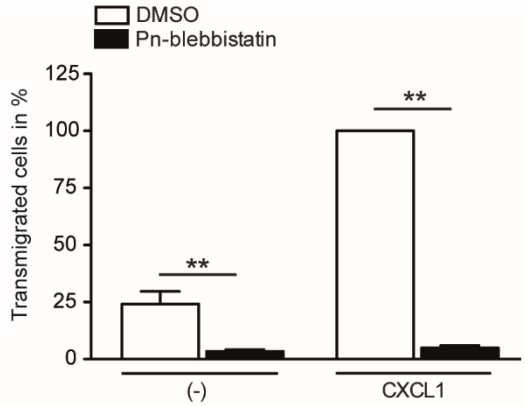

Figure 7. Transmigration through 3 µm pores is diminished in pn-blebbistatin-treated murine bone marrow-derived PMN. Quantitative analysis of transmigrated DMSO- and pn-blebbistatin-treated PMN towards a gradient of rmCXCL1 or without stimulus (-). Transmigrated PMN were normalized to DMSO-treated cells in the presence of rmCXCL1 (100%). n = 4. Mean ± SEM. ** $p < 0.01$ (adapted from Zehrer et al., 2018[180]).

3.2 PMN trafficking upon genetic downregulation of Myh9 in the hematopoietic system of mice

The next part of the study focused on investigating the distinct role of Myh9, the heavy chain of the NMII complex, using a genetic mouse model. A global knock-out of Myh9 was reported to be lethal at embryonic day 7.5[126]. Therefore, a conditional knock-out (cKO) of Myh9 in the hematopoietic system was intended for this study. Mice expressing Cre recombinase under the Vav promotor (*Vav-iCre*$^{+}$) were crossed with *Myh9*$^{fl/fl}$ mice. Offspring with a *Vav-iCre*$^{+}$*/Myh9*$^{wt/fl}$ genotype was bred with *Myh9*$^{fl/fl}$ mice, to generate the *Vav-iCre*$^{+}$*/Myh9*$^{fl/fl}$ cKO target animals.

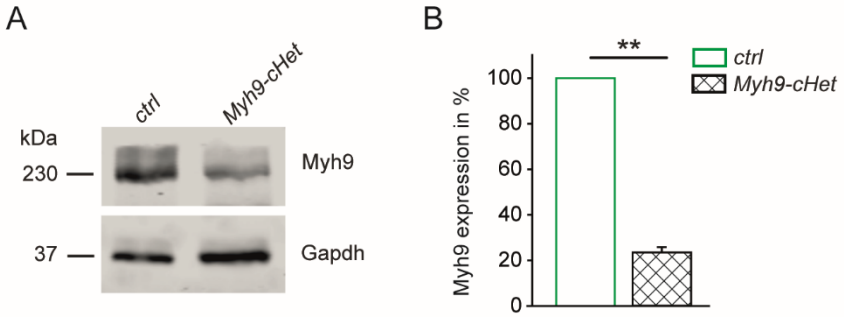

Figure 8. Diminished expression of Myh9 in PMN of *Myh9-cHet* mice. (A) Representative western blot of PMN lysates of *control* (*ctrl*) and *Myh9-cHet* mice **(B)** Quantitative analysis of Myh9 expression. Myh9 expression was normalized to the amount of GAPDH and *ctrl* mice (100%). Mean ± SEM, n = 5, ** $p < 0.01$ (adapted from Zehrer et al., 2018[180]).

As a result, 185 pups from 18 different mating pairs were analysed for their genotypes and *Vav-iCre^{+}/Myh9$^{wt/fl}$*, *Vav-iCre^{-}/Myh9$^{wt/fl}$* and *Vav-iCre^{-}/Myh9$^{fl/fl}$* mice were identified. However, no living offspring with a *Vav-iCre^{+}/Myh9$^{fl/fl}$* cKO genotype was found. Consequently, it was hypothesised that the cKO of Myh9 in the hematopoietic system is lethal. Therefore, experiments with PMN lacking Myh9 were not possible. Subsequently, the expression of Myh9 in PMN of *Vav-iCre^{+}/Myh9$^{wt/fl}$* (*Myh9-cHet*) mice was evaluated (Fig. 8). Interestingly, in *Myh9-cHet* PMN, the amount of expressed Myh9 was reduced to 23.5 ± 2.3% of the protein amount in *Vav-iCre^{-}/Myh9$^{wt/fl}$* (*control)* PMN. This was a greater reduction than expected for PMN with one remaining functional Myh9 allele. Hence, the possible significance of this downregulation of Myh9 expression for PMN trafficking was analysed in detail.

3.2.1 *In vitro* studies using PMN from *Myh9-cHet* and *control* mice

To study the maturation of *control* or *Myh9-cHet* PMN, the nuclear morphology and the expression of Ly6G, CXCR2 and CD11b was compared (Fig. 9). The mean fluorescence intensity of Ly6G, CXCR2 and CD11b as well as the morphology of the nucleus revealed no significant differences between *control* or *Myh9-cHet* PMN, suggesting that the maturation of PMN of *control* and *Myh9-cHet* mice was similar.

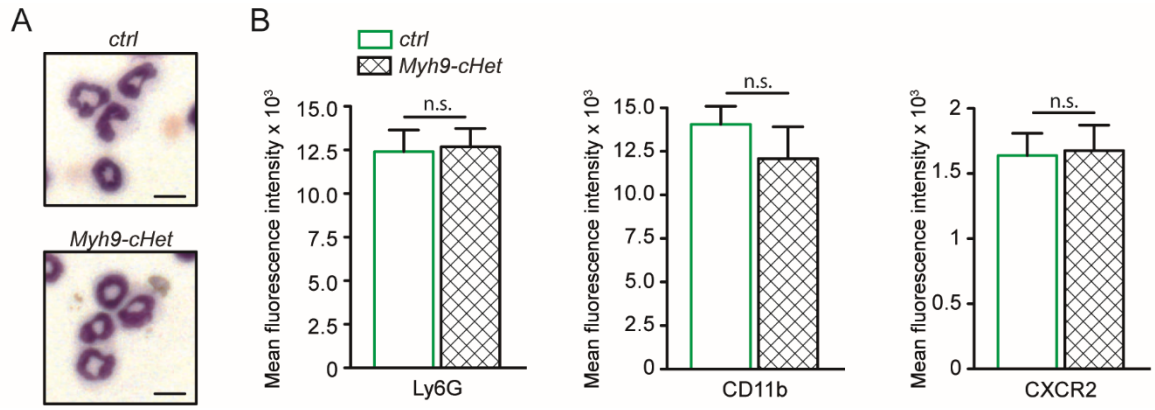

Figure 9. Similar maturity of PMN from *control (ctrl)* and *Myh9-cHet* mice. **(A)** May-Grünwald-Giemsa staining of PMN. Depicted are representative microscopic images. Scale bar, 10 µm. **(B)** Flow cytometry analysis of PMN using specific, fluorescently labelled antibodies for Ly6G, CXCR2 and CD11b. n = 5 (adapted from Zehrer et al., 2018[180]).

The effect of Myh9 knock-down for PMN trafficking was first investigated during spreading and polarisation of PMN on a rmICAM-1 and rmCXCL1 coated surface. No significant difference was found between *control* and *Myh9-cHet* PMN (Fig. 10A). Specifically, the area

and the circularity of PMN was comparable between both the *control* and the *Myh9-cHet* PMN, indicating that polarisation was not compromised upon downregulation of Myh9. To resist increasing shear stress forces, an effective activation of β_2 integrins into the extended, high affinity formation is essential for PMN[87]. To examine the influence of Myh9 for this β_2 integrin activation, *control* and *Myh9-cHet* PMN were allowed to adhere to immobilised rmICAM-1 and rmCXCL1 and increasing shear stress rates ranging from 0.5 up to 8 dyne/cm^2 were applied to the flow chamber. The percentage of adherent cells between c*ontrol* and *Myh9-cHet* PMN was calculated (Fig. 10B). Both the *control* and the *Myh9-cHet* PMN remained adherent throughout the observation time. Even at 8 dyne/cm^2, nearly 100% of *control* and *Myh9-cHet* PMN were still adherent to the surface of the flow chamber, indicating no impact of reduced Myh9 on inducing the high affinity conformation of the β_2 integrins.

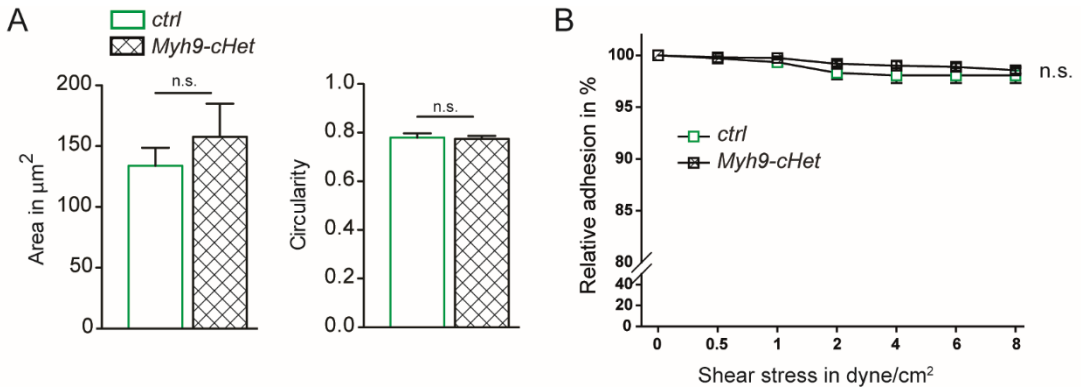

Figure 10. Reduced expression of Myh9 did not influence spreading or adhesion strengthening (A) Spreading of *control (ctrl)* and *Myh9-cHet* PMN upon exposure to immobilised rmICAM-1 and rmCXCL1 for 10 min in the absence of flow. Cell area and circularity were calculated from 3 independent experiments (n = 95 *ctrl* PMN, 74 *Myh9-cHet* PMN). **(B)** Percentage of adherent PMN, relative to the amount of adherent PMN before the onset of flow, at indicated shear stress rates. Mean ± SEM, n = 3, n.s. not significant (adapted from Zehrer et al., 2018[180]).

Next, the migration behaviour under flow conditions of *control* and *Myh9-cHet* PMN was analysed. The shape during migration under flow conditions, illustrated by the time-lapse images in Fig. 11A, appeared to be similar between *control* and *Myh9-cHet* PMN. Despite this, the quantitative analysis of the single cell migration tracks (Fig. 11B) demonstrated reduced migration velocity from 7.6 ± 0.15 µm/min in *control* PMN to 4.6 ± 0.03 µm/min in *Myh9-cHet* PMN. Euclidean distance was also reduced from 36.7 ± 1.6 µm for *control* PMN to 20.5 ± 1.6 µm for *Myh9-cHet* PMN (Fig 11C). Interestingly, this result was comparable to

the treatment with pn-blebbistatin, however the prominent phenotype with multiple pseudopods and an elongated cell shape was absent in *Myh9-cHet* PMN compared to pn-blebbistatin-treated PMN, suggesting a dose-dependent effect of Myh9 downregulation, which first compromises migration speed and only below a certain threshold the morphology of the migrating cells.

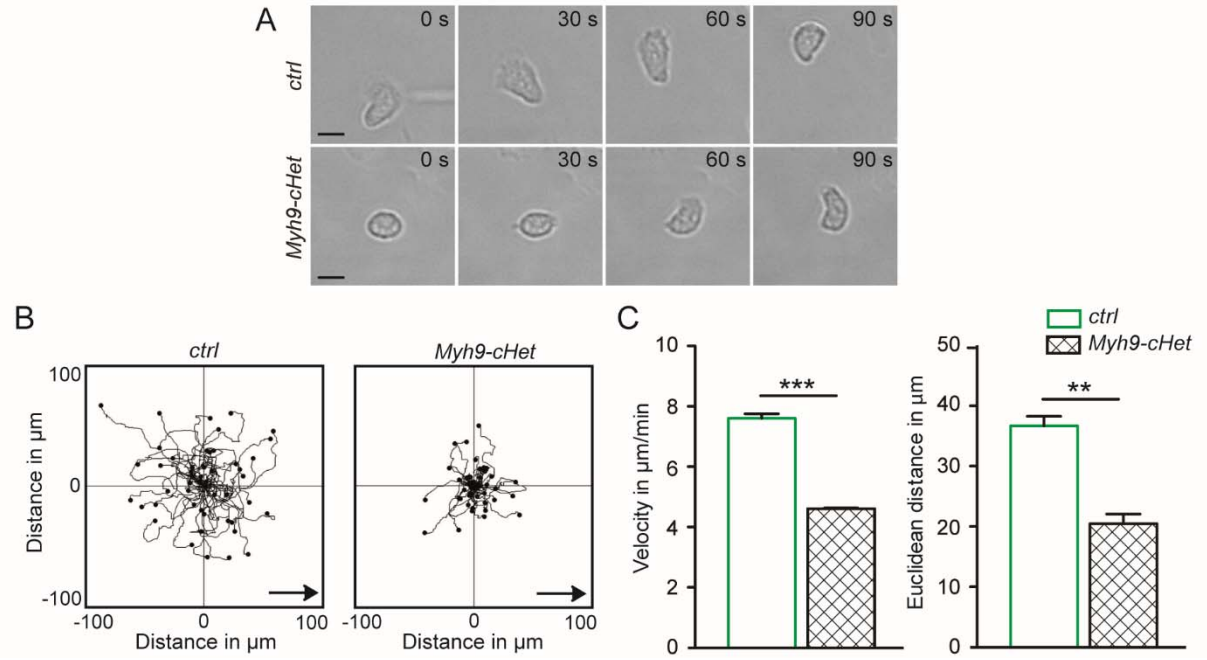

Figure 11. Reduced expression of Myh9 caused defects in 2D migration under flow conditions *in vitro*. (A) Representative time-lapse images of migrating *control (ctrl)* and *Myh9-cHet* PMN under 1 dyne/cm^2 shear stress on immobilised rmICAM-1 and rmCXCL1 at indicated time points. Scale bar, 10 µm. **(B)** Representative single cell migration tracks after 10 min under 1 dyne/cm^2 shear stress on immobilised rmICAM-1 and rmCXCL1. Arrows indicate direction of flow. **(C)** Migration velocity and Euclidean distance. n = 3 (322 *ctrl* PMN, 273 *Myh9-cHet* PMN. Mean ± SEM, n.s. not significant, ** $p < 0.01$, *** $p < 0.001$ (adapted from Zehrer et al., 2018[180]).

According to the consecutive steps in the PMN recruiting cascade, transmigration into the tissue is the next important step in the recruitment of PMN, following the migration along the vessel wall. Consequently, the PMN of *control* and *Myh9-cHet* mice were examined in two transmigration settings *in vitro*. The cells were allowed to transmigrate towards the chemoattractant rmCXCL1 through a membrane with 3 µm pores (Fig. 12A) or through a monolayer of bEnd.3 endothelial cells and an underlying membrane with a pore size of 8 µm (Fig. 12B). Successfully migrated PMN were counted and analysed. The experiments revealed that without the application of the stimulus, no difference in transmigration efficiency was observed between *control* and *Myh9-cHet* PMN. In this situation, 2.2 ± 0.9%

control and 3.6 ± 1.3% *Myh9-cHet* PMN transmigrated through the membrane pores and 21.6 ± 4.4% *control* and 23.3 ± 4.5% *Myh9-cHet* PMN transmigrated through the endothelial coated 8 µm pores. Upon application of rmCXCL1, *control* PMN transmigrated successfully through the membrane pores as well as the bEnd.3 endothelial monolayer towards rmCXCL1 (100%), whereas *Myh9-cHet* PMN transmigrated significantly less efficient in the presence of rmCXCL1, with only 40 ± 8.1% transmigrated *Myh9-cHet* PMN in case of the 3 µm pores and 49 ± 7% *Myh9-cHet* transmigrated PMN through the endothelial coated 8 µm pores compared to *control* PMN. These results indicated an important role for Myh9 during the process of transmigration of PMN.

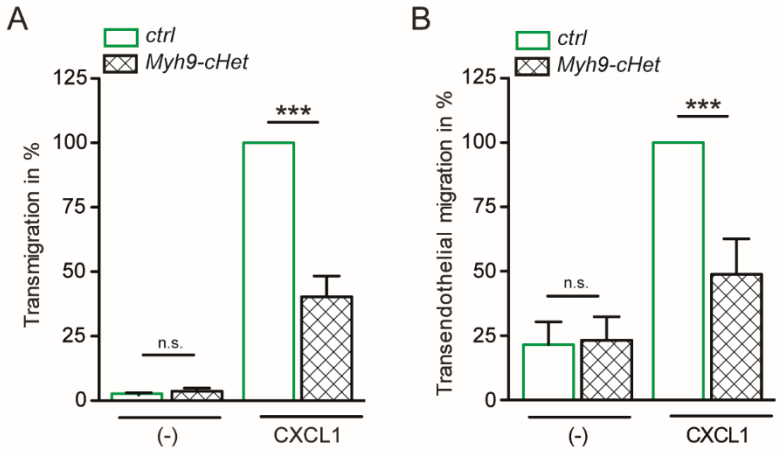

Figure 12. Diminished transmigration of PMN from *Myh9-cHet* mice *in vitro*. Quantitative analysis of transmigrated *control* (*ctrl)* and *Myh9-cHet* PMN towards a gradient of rmCXCL1 or without stimulus (-). Transmigrated PMN were normalized to *ctrl* PMN in the presence of rmCXCL1 (100%). **(A)** Transmigration through 3 µm pores. n = 3. **(B)** Transmigration through bEnd.3 endothelial cell coated 8 µm pores. n = 4. Mean ± SEM. n.s. not significant, *** $p < 0.001$ (adapted from Zehrer et al., 2018[180]).

To investigate the impact of reduced Myh9 expression on the migration behaviour of PMN in fibrillar 3D environment, *control* and *Myh9-cHet* PMN were allowed to migrate in collagen networks towards the chemoattractant rmCXCL1 *in vitro*, mimicking interstitial migration towards sites of inflammation *in vivo*. Single cell migration tracks (Fig. 13A) of *control* and *Myh9-cHet* PMN in the collagen environment were compared and the associated parameters of migration velocity and Euclidean distance were analysed quantitatively (Fig. 13C). Here, *control* PMN displayed a mean velocity of 6.7 ± 0.43 µm/min and *Myh9-cHet* PMN had a significantly reduced migration velocity of 4.7 ± 0.37 µm/min. Also, the Euclidean distance was diminished in *Myh9-cHet* PMN compared to *control* PMN, from 33.7 ± 2.2 µm in *control* PMN to 23.4 ± 1.8 µm in *Myh9-cHet* PMN. To analyse the capacity of the *control* and

Myh9-cHet PMN to sense and orientate in the direction of the chemoattractant, rose plots (Fig. 13B) as well as the parameters directness (Euclidean distance divided by accumulated distance, indicating the straightness of migration) and forward migration index (end-position on x axis divided by accumulated distance, representing the efficiency of the forward migration towards the chemoattractant) (Fig. 13C) were employed. These criteria revealed that the reduction of Myh9 expression in *Myh9-cHet* PMN did not influence their ability to sense the rmCXCL1 gradient and to orientate migration in a specific direction.

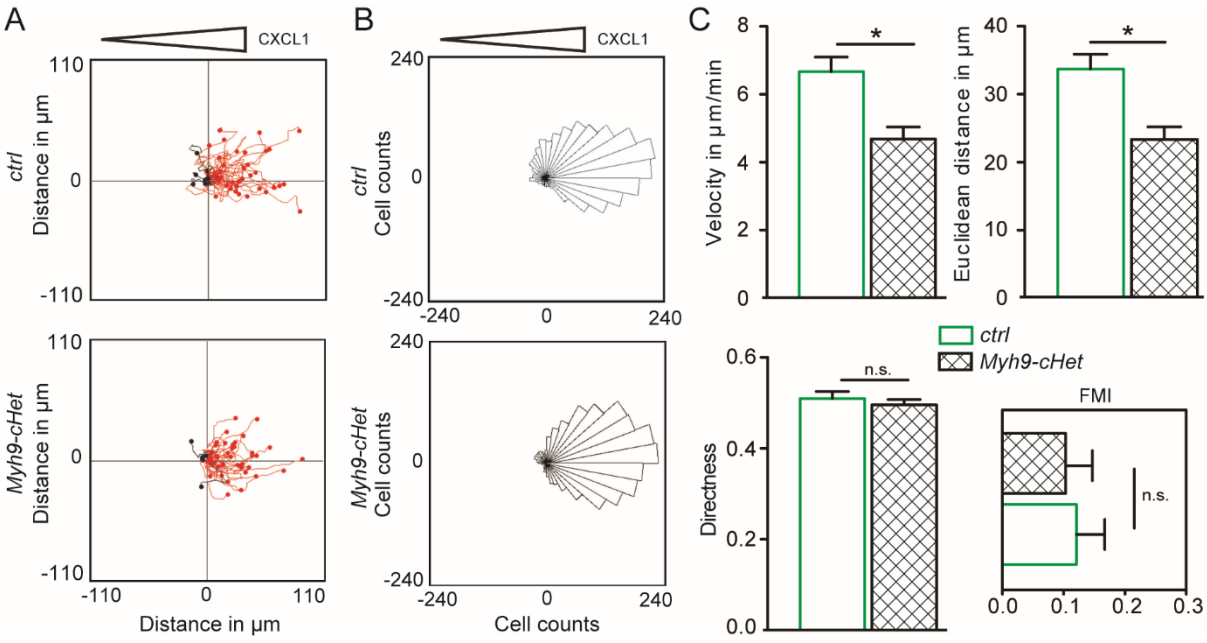

Figure 13. 3D migration *in vitro* was severely reduced in *Myh9-cHet* PMN. Migration in 3D collagen networks (1.5 mg/mL) of *control* (*ctrl)* and *Myh9-cHet* PMN towards gradients of rmCXCL1 for 10 min. **(A)** Exemplary single cell migration tracks and **(B)** Rose plots. The area of each sector is proportional to the frequency of the migration vectors of tracked *ctrl* and *Myh9-cHet* PMN in the respective direction in response to gradients of rmCXCL1. Triangles indicate orientation of gradients. **(C)** Migration velocity and Euclidean distance as well as directness and forward migration index (x) (FMI). Mean ± SEM, n = 3 (441 *ctrl* and 386 *Myh9-cHet* PMN). n.s. not significant, * $p < 0.05$ (adapted from Zehrer et al., 2018[180]).

To decipher the mechanistic link between Myh9 downregulation and the observed migration defects, the subcellular localisation of Myh9 and F-actin during migration of *control* and *Myh9-cHet* PMN was analysed upon immunofluorescence staining of F-actin and Myh9 using STED nanoscopy. *Control* PMN localised their F-actin in the lamellipodium as well as in the trailing edge of the cells. Similarly, Myh9 was localised mainly in the leading edge and the uropod of the *control* PMN and colocalised at the front and back of the cells with F-actin (Fig. 14 left panel, merge). This distribution pattern stood in strong contrast to the observation

in *Myh9-cHet* PMN. Here, F-actin prevailed in the trailing edge of the PMN. Importantly, the Myh9 that was still expressed in *Myh9-cHet* PMN appeared to accumulate in one single spot, close to the rear of the cell with no apparent colocalisation with F-actin (Fig. 14 right panel, merge). These results indicated an impact of Myh9 expression on the subcellular localisation of Myh9 and F-actin during migration.

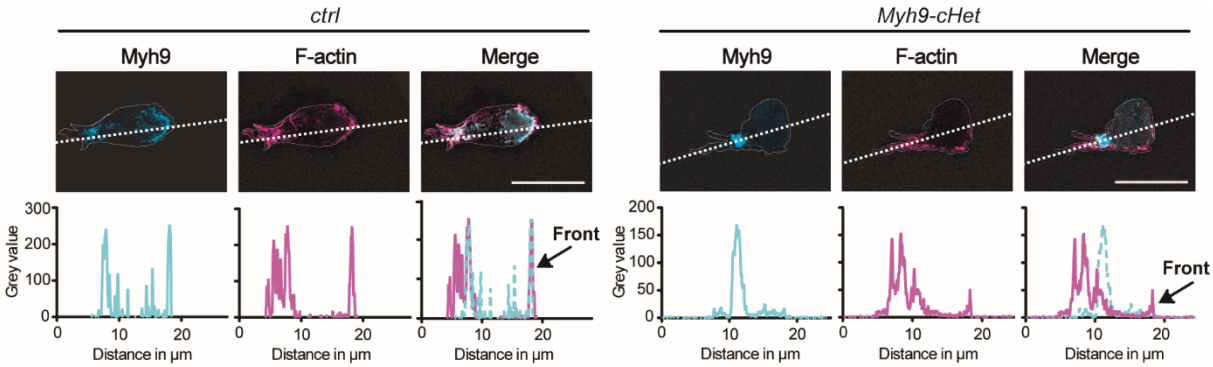

Figure 14. Reduced Myh9 expression influenced subcellular localisation of Myh9 and F-actin during migration. STED nanoscopy images of migrating *control (ctrl)* and *Myh9-cHet* PMN on rmICAM-1 and rmCXCL1. Representative microscopic images (upper panel) and intensity profiles (lower panel) of F-actin and Myh9 along the segmented line through the representative PMN, of 8 *control* and 5 *Myh9-cHet* PMN. F-actin in magenta, Myh9 in cyan, merge in white. Scale bar, 10 µm, arrows indicate the front of the PMN (adapted from Zehrer et al., 2018[180]).

To elucidate the influence of reduced Myh9 expression on the amount of expressed G-actin, the total amount of G-actin protein was compared between *control* and *Myh9-cHet* PMN using western blot. Here, no significant differences between the genotypes were detected (Fig. 15A). Next, the percentage distribution of F-actin and Myh9 to either the front or back of the PMN was analysed (Fig. 15 B, C). In *control* PMN 41.0 ± 4.1% of the F-actin intensity was found in the back of the cells and 57.0 ± 4.1% of the F-Actin intensity in the front of the cells. In *Myh9-cHet* PMN the F-actin distribution was 59.0 ± 8.0% in the back of the cells and 37.5 ± 8.4% in the front of the cells. The distribution of Myh9 fluorescence intensity was in *control* PMN 40.5 ± 3.5% in the back of the cells and 57.0 ± 3.2% in the front of the cell. For *Myh9-cHet* PMN a Myh9 distribution with 57.7 ± 3.0% in the back of the cells and 38.6 ± 3.6% in the front of the cells was detected. These quantitative results confirmed the observed shift of F-actin and Myh9 to the back of the cell in *Myh9-cHet* PMN compared to *control* PMN (Fig. 14 & 15 B/C), indicating a dysregulation in acto-myosin dynamics upon Myh9 downregulation.

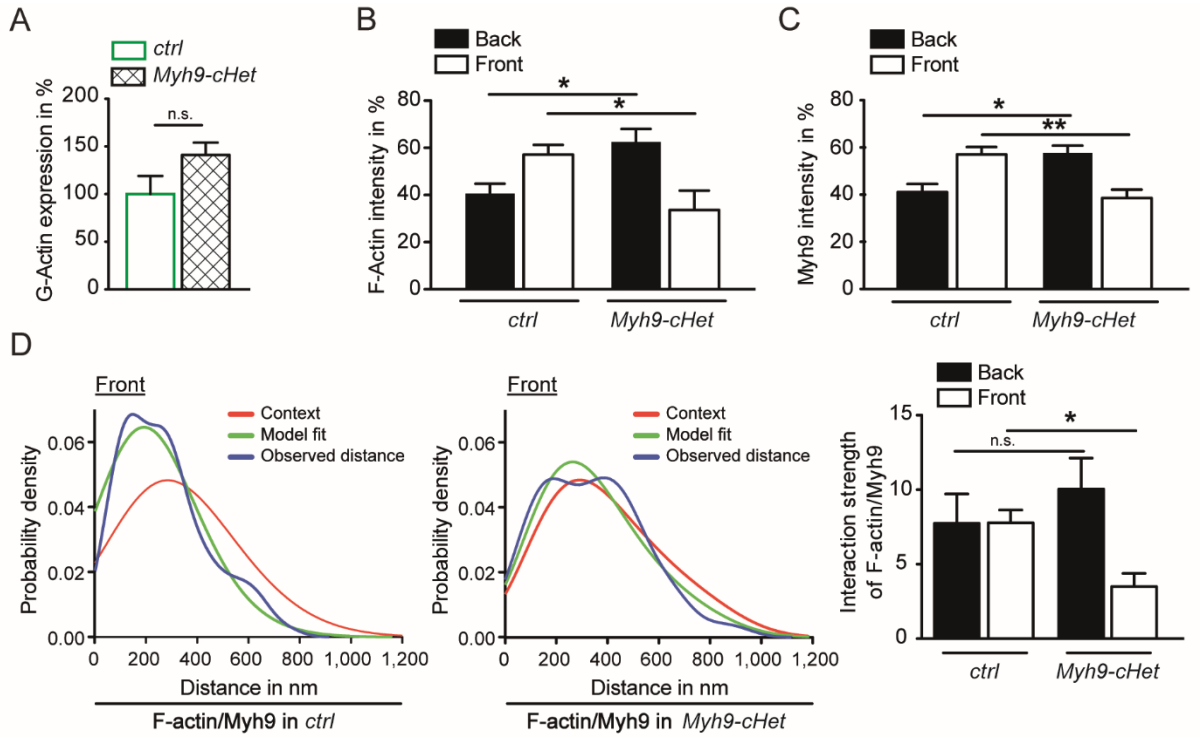

Figure 15. Amount of Myh9 expression influenced Myh9-dependent F-actin distribution. **(A)** Actin expression in cell lysates from *control (ctrl)* and *Myh9-cHet* PMN. Protein expression was normalized to the amount of GAPDH protein expression (*ctrl* PMN 100%). n = 4 **(B)** F-actin and **(C)** Myh9 intensity distribution in percent in the back or the front of *ctrl* and *Myh9-cHet* PMN compared to total cell (100%). Total cell area was split equally into back and front. n = 8 for *ctrl* and n = 5 for *Myh9-cHet* PMN. **(D)** Randomization approach using the nearest-neighbour analysis with the MosaicIA interaction plugin of Fiji to analyse the dependence of F-actin localisation from Myh9 localisation. Exemplary distance distributions of the front of a *ctrl* and a *Myh9-cHet* PMN (Left and middle panel). Blue line, observed distance distribution between F-actin and Myh9. Green line, model fit of the observed distance distribution using a Plummer potential. Red line, probability density function (context) if F-actin was distributed randomly and independent of Myh9. F-actin/Myh9 interaction strength (right panel) in the front and back during migration. n = 4. Data represent mean ± SEM. * $p < 0.05$, ** $p < 0.01$ (adapted from Zehrer et al., 2018[180]).

To investigate if F-actin distributes in dependence of Myh9, a statistical randomization approach was utilised (Fig. 15D). Here, the distance distribution of F-actin to Myh9 was graphically illustrated. In strong contrast to *control* PMN, upon Myh9 downregulation the observed distance distribution between F-actin and Myh9 in the front of the PMN (blue line), became similar to the probability density function (context, red line) representing F-actin distribution independent of Myh9. The curves were employed to calculate the interaction strength, indicating the degree of dependence between F-actin and Myh9 localisation. Values above 0 imply a spatial distribution of F-actin dependent of the spatial distribution of Myh9. The interaction strength of F-actin/Myh9 in the front of the cells was significantly different

between *control* and *Myh9-cHet* PMN with 7.8 ± 0.9 in *control* PMN and only 3.5 ± 0.9 in *Myh9-cHet* PMN[180]. These findings indicated that F-actin distribution was dependent on Myh9 localisation and that reduced expression of Myh9 restricted this interaction causing disturbed F-actin dynamics in the front of the cell, potentially impairing PMN migration.

3.2.2 *In vivo* models using *Myh9-cHet, control* and bone marrow chimeric mice

Despite the valuable *in vitro* experimental designs employed to study PMN trafficking, the situation *in vivo* often involves many unpredictable factors. Therefore, it is crucial to test the *in vitro* gained assumptions in an *in vivo* environment. First, the blood of *control* and *Myh9-cHet* mice was analysed for white blood cell (WBC) counts, along with the maturity of blood PMN between *control* and *Myh9-cHet* mice (Fig. 16). The comparison of WBC counts revealed no significant differences between the two genotypes in total WBC, PMN, lymphocytes, and monocytes (Fig. 16A). The analysis of the expression of the maturity markers Ly6G, CXCR2 and CD11b revealed similar expression of the three markers in *control* and *Myh9-cHet* PMN from the blood of these mice, indicating similar maturity of blood PMN in *control* and *Myh9-cHet* mice (Fig. 16B).

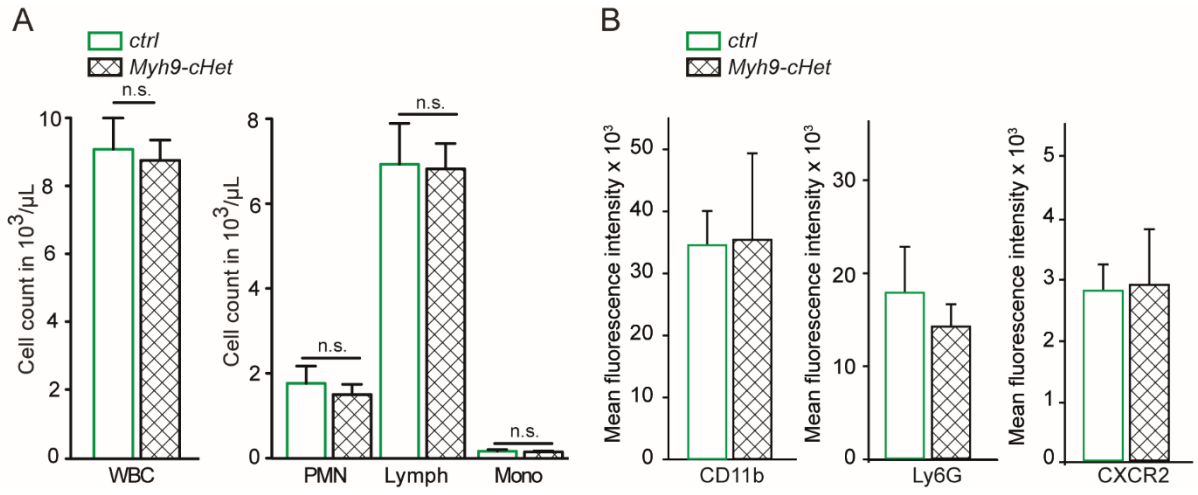

Figure 16. Similar composition of white blood cells and maturity of blood PMN in *control (ctrl)* and *Myh9-cHet* mice. (A) White blood cell (WBC) counts. Lymph, lymphocytes; Mono, monocytes. n = 7 for *ctrl* and 9 for *Myh9-cHet* mice **(B)** Analysis of blood PMN by flow cytometry using specific, fluorescently labelled antibodies for expression of Ly6G, CXCR2 and CD11b. n = 5 (adapted from Zehrer et al., 2018[180]).

To analyse the physiological relevance of Myh9 for PMN recruitment *in vivo*, two different models of acute inflammation were performed using *Myh9-cHet* and *control* mice. In the

model of laser-induced sterile injury of the ear dermis, PMN recruitment is caused by a single necrotic lesion induced by focusing the laser beam to a single site in the murine ear. The tissue damage promotes PMN extravasation out of the vessel into the tissue and swarming towards the site of injury. Extravasation and interstitial migration were monitored using 2-photon microscopy, FITC-dextran labelled vessels and Ly6G-PE-labelled PMN. For the analysis of the recorded videos, extravasation was determined using PE intensities within a circular area of interest, defined by the border of the laser injury to the border of the nearest vessel. Quantification was performed by calculating the fold change of the sum of intensity values, relative to the background intensity immediately after injury. During the observed time period of 40 min, a fold increase of PMN extravasation of 4.3 ± 1.6 compared to the starting time point with 1.0 ± 0.1 was recorded for *control* mice, but only a minimal number of PMN extravasated in *Myh9-cHet* mice, indicated by a fold increase from 1.0 ± 0.1 to 0.9 ± 0.2 after 40 min (Fig. 17A). This significant reduction in extravasation of PMN in *Myh9-cHet* mice compared to *control* mice suggested an important role for Myh9 for extravasation of PMN *in vivo*.

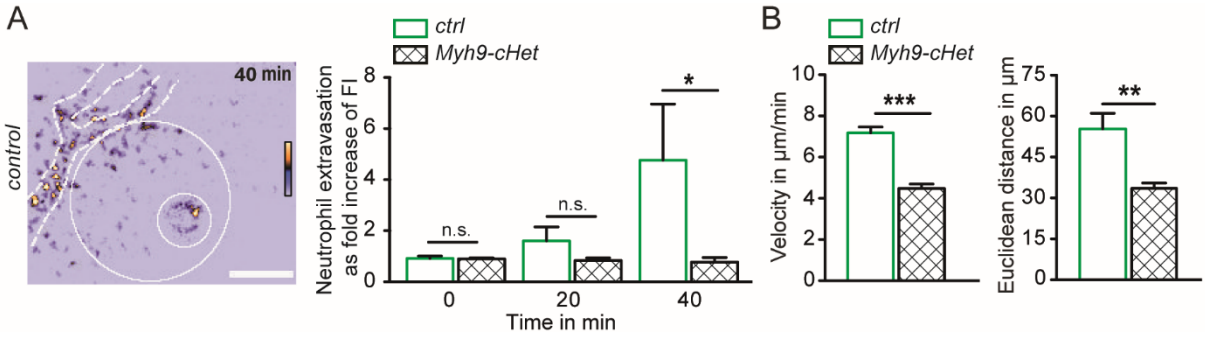

Figure 17. Transmigration and interstitial migration were severely impaired in a laser-induced injury model in the ear of *Myh9-cHet* mice. (A) Representative image of extravasation in a *control* mouse 40 min after induction of injury. Scale bar, 10 µm. PMN in pseudocolors, heat map = . (left panel). PMN extravasation evaluated as fold change of the sum of fluorescence intensity (FI) values compared to time-point 0, relative to the area between the two white circles, at indicated timeframes (right panel). **(B)** Migration velocity and Euclidean distance of interstitially migrating PMN. n = 5 for each mouse strain (≥10 PMN per mouse). Mean ± SEM. n.s. not significant,* $p < 0.05$, ** $p < 0.01$, *** $p < 0.001$ (adapted from Zehrer et al., 2018[180]).

Additionally, PMN interstitially migrating towards the injury were analysed for their migration velocity and Euclidean distance during a 10 min time frame in *control* and *Myh9-cHet* mice (Fig. 17B). For PMN in *control* mice a migration velocity of 7.2 ± 0.29 µm/min and an Euclidean distance of 55.3 ± 5.7 µm was determined. *Myh9-cHet*

PMN migrated with a significantly reduced velocity of 4.5 ± 0.21 µm/min and exhibited a diminished Euclidean distance of 33.6 ± 1.9 µm. The results of this injury model highlighted the importance of Myh9 for the extravasation process of PMN and demonstrated the relevance of Myh9 for interstitial migration *in vivo*.

To confirm the *in vivo* trafficking defects of *Myh9-cHet* PMN, an additional model of acute inflammation was employed. In the rmCXCL1-induced peritonitis model the number of extravasated PMN into the peritoneal cavity was determined 4 h after intra-peritoneal injection of rmCXCL1 (Fig. 18). In *control* mice, 0.32 x 10^6 ± 0.12 PMN extravasated in the control situation with injection of 0.9% NaCl. Upon rmCXCL1 injection a profound extravasation of 3.25 x 10^6 ± 0.20 PMN was induced. On the other hand, in *Myh9-cHet* mice 0.25 x 10^6 ± 0.13 PMN extravasated in the control situation, but only 0.82 x 10^6 ± 0.36 PMN were found in the peritoneal cavity after application of the stimulus. This significant reduction in extravasation after application of rmCXCL1 in *Myh9-cHet* mice compared to *control* mice highlighted the importance of an adequate Myh9 expression for an accurate recruitment of PMN.

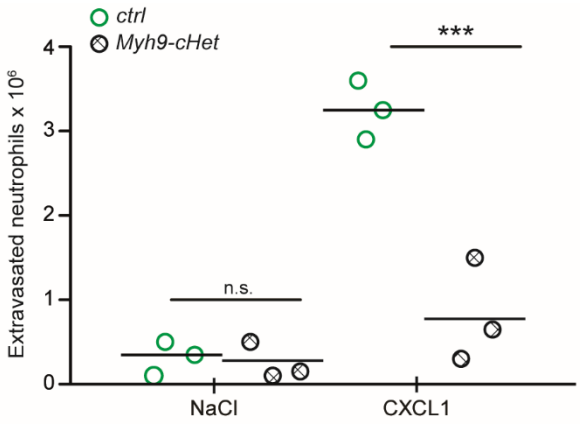

Figure 18. Diminished number of extravasated PMN into the peritoneal cavity in *Myh9-cHet* mice. Number of PMN in the peritoneal lavage 4 h after intra-peritoneal injection of 0.9% NaCl or 300 ng rmCXCL1 in *control* (*ctrl)* or *Myh9-cHet* mice. Data represents mean with individual data points, n = 3. n.s. not significant, *** $p < 0.001$ (adapted from Zehrer et al., 2018[180]).

To study whether the observed migration defects were cell-intrinsic, three different models of bone marrow chimeras were set up (Fig. 19A). To distinguish between donor and recipient cells, the CD45.1/2 system was applied. In the first model, serving as control, CD45.1 expressing wildtype bone marrow cells were transplanted in lethally irradiated CD45.1 expressing wildtype mice (WT→WT). The second model involved the transplantation of

CD45.2 expressing *Myh9-cHet* bone marrow cells into CD45.1 expressing wildtype mice (HET→WT). In the third model, a 1:1 ratio of CD45.1 wildtype and CD45.2 *Myh9-cHet* bone marrow cells were transferred into CD45.1 expressing wildtype mice (MIX→WT).

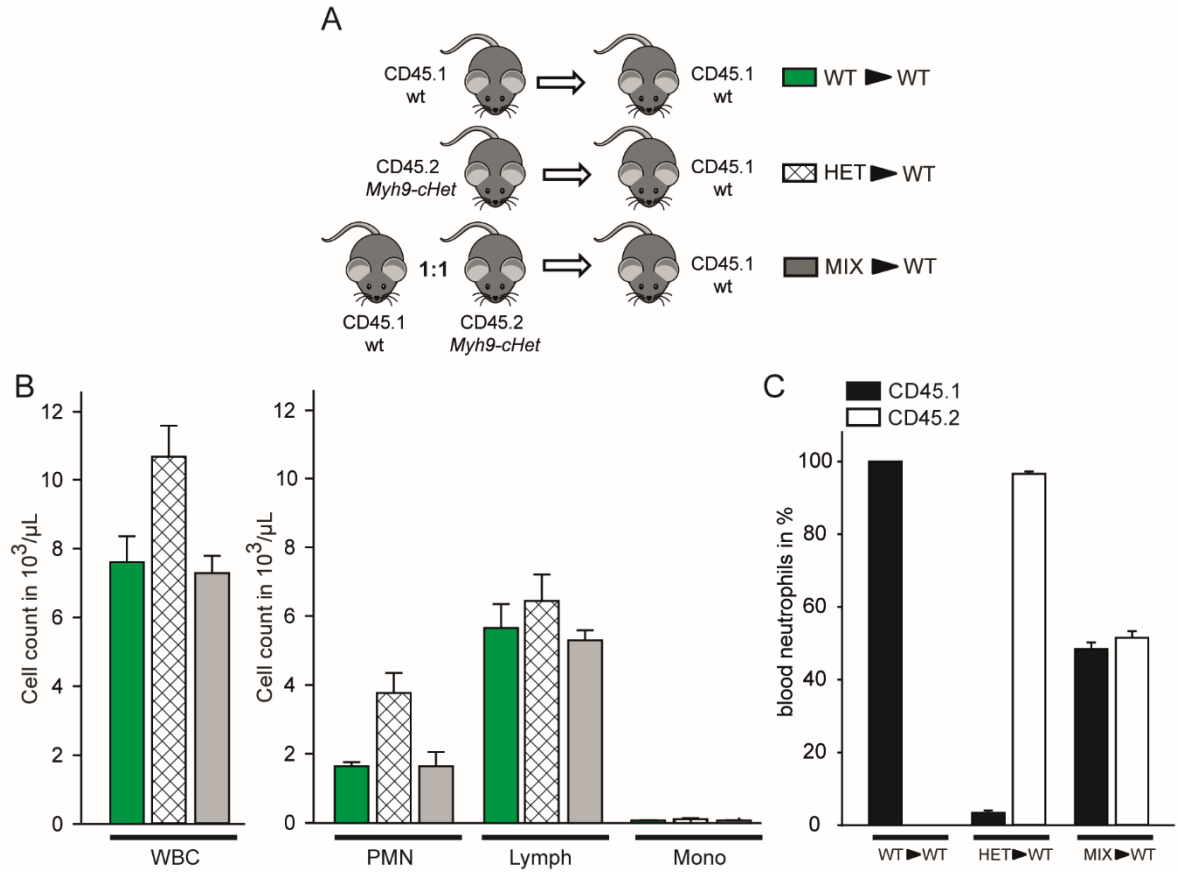

Figure 19. Successful generation of bone marrow chimeras. (A) Schematic of bone marrow transfer models **(B)** White blood cell (WBC) counts. Lymph, lymphocytes; Mono, monocytes. **(C)** Distribution of CD45.1 and CD45.2 positive blood PMN in the three models. $n \geq 5$ (adapted from Zehrer et al., 2018[180]).

After a recovery time of 6 weeks, successful engraftment of donor cells was investigated by analysing the blood of the chimeras for WBC counts and the percentage of CD45.1 or CD45.2 expressing PMN (Fig. 19B, C)[180]. Here, comparable numbers of lymphocytes and monocytes were found in all three models. The counts for PMN and consequently total WBC were slightly elevated in the HET→WT mice, but similar in the WT→WT and MIX→WT models. In the case of successful generation of bone marrow chimeric mice, 100% CD45.1 positive PMN in the WT→WT model, 100% CD45.2 positive PMN in the HET→WT model and a 50%/50% proportion of CD45.1 and CD45.2 positive PMN in the MIX→WT model were expected. In this study, all PMN were CD45.1 positive in the WT→WT model, while in the HET→WT model, only 3% of the PMN were of recipient origin and CD45.1 positive,

whereas 97% were of donor origin and CD45.2 positive. In the MIX→WT model, the distribution was determined to be 48% CD45.1 and 52% CD45.2 positive PMN (Fig. 19C). Thus, the distribution of CD45.1 and CD45.2 amongst the PMN in the blood was as expected and indicated successful engraftment of donor cells in the irradiated recipient mice.

To investigate PMN recruitment in the chimera models, the rmCXCL1-induced peritonitis model was employed. The number of extravasated PMN into the peritoneal cavity was determined 4 h after intra-peritoneal injection of rmCXCL1 (Fig. 20A). In the WT→WT control model, 0.90 x 10^6 ± 0.45 PMN were detected in the peritoneal cavity upon injection of 0.9% NaCl, whereas upon rmCXCL1 injection a profound extravasation of 4.86 x 10^6 ± 0.49 PMN was induced. In contrast, in the HET→WT model, 0.03 x 10^6 ± 0.03 PMN extravasated upon injection of 0.9% NaCl, and only 3.27 x 10^6 ± 0.21 PMN extravasated after application of the stimulus. In the MIX→WT mice 0,60 x 10^6 ± 0.45 PMN were detected in the peritoneal cavity in the control situation. Interestingly, the extravasation of PMN in the peritoneal cavity upon rmCXCL1 application was comparable to that observed in the HET→WT mice, with 3.21 x 10^6 ± 0.40 PMN.

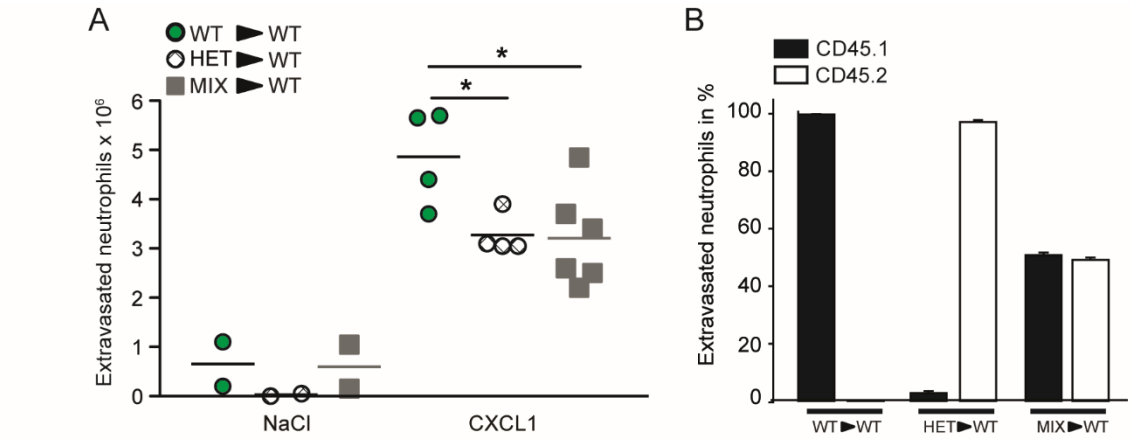

Figure 20. Diminished number of extravasated PMN into the peritoneal cavity in HET→WT and MIX→WT chimeric mice. (A) Number of PMN in the peritoneal lavage 4 h after intra-peritoneal injection of 0.9% NaCl or 300 ng rmCXCL1 in WT→WT, HET→WT and MIX→WT chimeric mouse models. Data represents mean with individual data points **(B)** Distribution of CD45.1 and CD45.2 positive extravasated PMN in the three models. Data represents mean ± SEM, n = 2 for NaCl, n ≥ 4 for rmCXCL1. * $p < 0.05$ (adapted from Zehrer et al., 2018[180]).

The analysis of CD45.1 and CD45.2 distributions in the extravasated PMN pool revealed an unchanged pattern in the blood of the mice (compare Fig. 19C and 20B). These results

suggest a cell-intrinsic migration defect in PMN upon Myh9 downregulation as the presence of wildtype PMN could not rescue the extravasation defect in the MIX→WT mice. Furthermore, the reduced extravasation in HET→WT mice confirmed the observations with the *control* and *Myh9-cHet* mice.

3.3 Hoxb8- SCF cell-derived neutrophils - a tool to study PMN trafficking

3.3.1 Generation and differentiation of Hoxb8-SCF cells

As PMN are especially short-lived cells and therefore not genetically manipulable, PMN research often relied on pharmacological inhibitor studies. During the last decade, a new murine cell system has been developed, based on the immortalisation of murine hematopoietic progenitor cells using an estrogen-dependent variant of the transcription factor Hoxb8 (ER-Hoxb8). The Hans Häcker group described that, upon estrogen binding, the ER-Hoxb8 fusion protein translocates to the nucleus and induces the transcription of all proteins necessary to prevent differentiation of the progenitor cells[197,198]. Upon estrogen removal, the ER-Hoxb8 becomes inactive and the progenitor cells differentiate. During the generation of the Hoxb8 cell line, growth factors influence the type of progenitor cells produced. Lymphoid primed multipotent progenitors (LMPP) can be generated using Flt3L, whereas SCF drives the cells towards granulocyte-macrophage progenitors (GMP)[198]. During the process of differentiation, the addition of growth factors also plays an import role, as they determine the cell type the progenitors differentiate into. In this study, Hoxb8-SCF cells with the potential to differentiate towards PMN and macrophages were generated from hematopoietic progenitor cells in murine bone marrow or foetal livers and differentiation towards PMN was initiated by the removal of estrogen and the presence of SCF and G-CSF.

To establish Hoxb8-SCF cell-derived neutrophils as a tool to study PMN trafficking, the optimisation of the differentiation process including the selection of the optimal length was crucial. Therefore, Hoxb8-SCF cells were allowed to differentiate for 6 days, with samples taken at day 0, 3, 4, 5, and 6, to be analysed for their percentage of viable cells, as well as the expression of CD11b and Ly6G, two key makers of murine PMN differentiation (Fig. 21). The results demonstrated that these extracellular markers were barely detectable on undifferentiated Hoxb8-SCF cells at day 0, but expression was induced upon differentiation, with Ly6G increasing continuously over the observed period of time (Fig. 21B). Importantly,

the viability of the Hoxb8-SCF cells was found to decrease rapidly after day 4 of differentiation (Fig. 21A). Consequently, day 4, with 76.7 ± 1.2% of viable cells and considerable expression of CD11b and Ly6G was chosen as the endpoint of differentiation for this study.

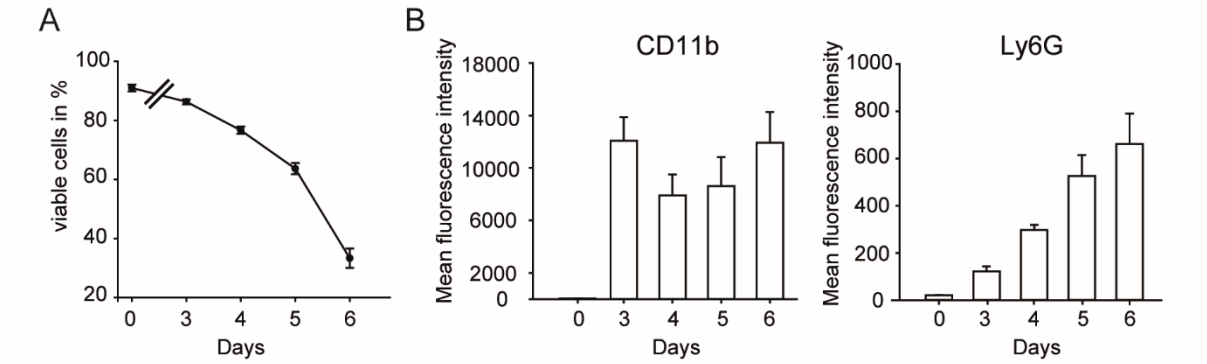

Figure 21. CD11b and Ly6G expression got induced in viable Hoxb8-SCF cells upon differentiation. Hoxb8-SCF cells were differentiated for the indicated days by removal of estrogen and addition of G-CSF. (A) Amount of living Hoxb8-SCF cells in percent, determined using PI staining. (B) Expression of CD11b and Ly6G analysed at indicated days by flow cytometry using specific, fluorescently labelled antibodies. Mean fluorescence intensity corrected by isotype control. n = 3. Mean ± SEM.

Undifferentiated (d0) and differentiated (d4) Hoxb8-SCF cells were subsequently characterised for their phenotypic appearance (Fig. 22). May-Grünwald-Giemsa staining confirmed a large, unsegmented nucleus in the progenitor cells, whereas after 4 days of differentiation the Hoxb8-SCF cells were reduced in size and the nucleus altered to the segmented shape typically observed in PMN (Fig. 22A). Comparison of extracellular markers between d0, d4 and murine bone marrow-derived PMN confirmed that Hoxb8-SCF cells downregulated the progenitor markers CD34, Flt3 and c-kit during differentiation to similar levels as in PMN (Fig. 22B). Murine PMN maturity markers Gr-1, Ly6G and CXCR2 were absent in d0 Hoxb8-SCF progenitor cells, yet were strongly induced in d4 Hoxb8-SCF cells and were also present in PMN (Fig 22C). The analysis of integrin expression revealed that LFA-1 (CD11a/CD18) was similarly expressed in d0, d4 Hoxb8-SCF cells and PMN, whereas CD11b was barely expressed in undifferentiated d0 Hoxb8-SCF cells and highly expressed in d4 Hoxb8-SCF cells and PMN. The integrin subunit CD11c was absent in all three tested cell types, confirming the absence of CD11c expressing cell types, like dendritic cells (Fig. 22D). This data suggests a very similar phenotype between d4 Hoxb8-SCF cells and murine bone marrow-derived PMN.

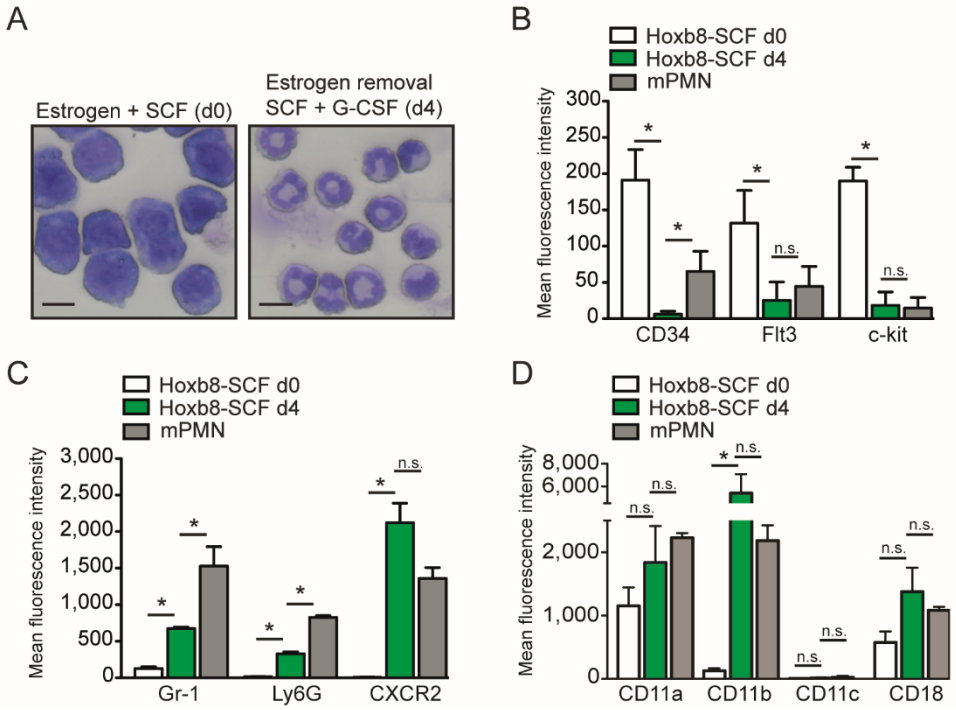

Figure 22. Differentiation profile of Hoxb8-SCF cells before and after removal of estrogen for 4 days. Undifferentiated (d0) Hoxb8-SCF cells, differentiated for 4 days with SCF and G-CSF towards PMN (d4) **(A)** Stained with May-Grünwald-Giemsa. Depicted are representative microscopic images. Scale bar, 10 µm. **(B-D)** D0 and d4 Hoxb8-SCF cells, as well as murine bone marrow-derived PMN were analysed by flow cytometry using specific, fluorescently labelled antibodies for expression of differentiation markers. **(B)** CD34, Flt3, and c-kit, **(C)** Gr-1, Ly6G, and CXCR2 and **(D)** CD11a, CD11b, CD11c, and CD18. Mean fluorescence intensity corrected by isotype control. n = 3. Mean ± SEM. * $p < 0.05$ (adapted from Zehrer et al., 2018[180]).

3.3.2 Functional characterisation of Hoxb8-SCF cell-derived neutrophils

To employ Hoxb8-SCF cell-derived neutrophils as a tool to study the processes involved in PMN trafficking, the cells not only have to have a phenotype similar to PMN, but must also behave similar to PMN in various experimental conditions. Upon stimulation, PMN quickly upregulate the integrins CD11b and CD18. These are stored in secondary, peroxidase-negative, granules to be immediately available for presentation at the cell surface when the PMN is activated[33].To determine whether Hoxb8-SCF cells are able to react upon stimulation with upregulation of surface CD11b and CD18, d0 and d4 Hoxb8-SCF cells were stimulated with PMA, rmCXCL1, rmTNFα, or fMIVIL and cell surface expression of the integrins CD11b, CD18 and CD11a was analysed using flow cytometry (Fig. 23). Undifferentiated d0 Hoxb8-SCF progenitor cells, as expected, did not react upon stimulation by upregulation of integrins, rather they maintained the expression of CD18 and CD11a at the basal level

described previously (Fig. 22D). However, d4 Hoxb8-SCF cells significantly increased CD11b and CD18 at the cell surface upon interaction with all tested stimuli compared to the controls. In contrast, the expression of CD11a, was not affected by stimulation, as expected (Fig. 23)[33,34].

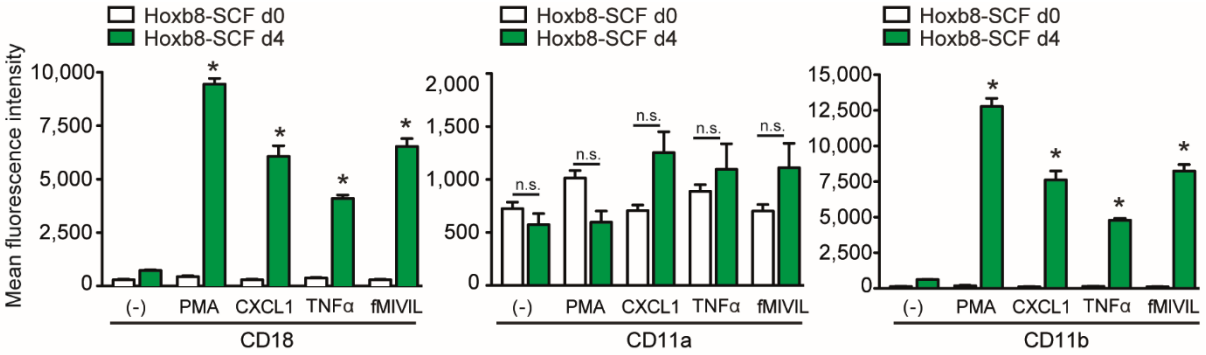

Figure 23. Upregulation of Mac-1 in d4 Hoxb8-SCF cells after stimulation. Hoxb8-SCF cells before (d0) and after (d4) removal of estrogen were stimulated with 100 nM PMA, 100 ng/mL rmCXCL1, 100 ng/mL rmTNFα, 100 nM fMIVIL, or left untreated (-) for negative control. CD11b, CD18 and CD11a cell surface expression was analysed using flow cytometry using specific, fluorescently labelled antibodies. Mean fluorescence intensity corrected by isotype control. n = 3. Mean ± SEM. * $p < 0.05$ unstimulated vs. stimulated (adapted from Zehrer et al., 2018[180]).

After upregulation and activation of integrins, PMN have the potential to adhere to surfaces via their integrins. Hence, the ability of Hoxb8-SCF cells to induce adhesion was investigated under static and flow conditions *in vitro* (Fig. 24). Under static conditions d0 and d4 Hoxb8-SCF cells were allowed to adhere after stimulation with PMA, rmCXCL1, rmTNFα, or fMIVIL and the result was calculated in fold induction of adhesion compared to unstimulated conditions (Fig. 24A). In accordance to the basal expression of CD11a and CD18 in d0 Hoxb8-SCF cells, these progenitor cells adhered to ICAM-1 coated surfaces when stimulated with the non-physiological stimulator PMA or the inflammatory mediator rmTNFα. As binding of mfibrinogen requires CD11b, the d0 Hoxb8-SCF cells were not able to induce adhesion on this surface, as expected. However, d4 Hoxb8-SCF cells were found to adhere after incubation with all tested stimuli on rmICAM-1, and after incubation with PMA, rmCXCL1 and fMIVIL on mfibrinogen (Fig. 24A). The efficiency for induction of adhesion under flow conditions was directly compared between d4 Hoxb8-SCF cells and murine bone marrow-derived PMN. Cell counts for rolling and adherent cells on immobilised rmP-selectin, rmICAM-1 and rmCXCL1 were determined at five different time-points during the assay (Fig. 24B, left panel). No significant difference was observed between PMN and

d4 Hoxb8-SCF cells during this time-course, indicating that the behaviour of the two cell types is highly comparable in this experiment. Furthermore, the specificity of adhesion of the d4 Hoxb8-SCF cells was tested by repeating the assay without immobilised rmCXCL1 (Fig. 24B, right panel). As expected, the number of rolling cells was significantly increased from 22 ± 8, in the presence of rmCXCL1, to 235 ± 51, in the absence of rmCXCL1. The number of adherent cells was strongly diminished from 445 ± 60, in the presence of rmCXCL1, to 195 ± 69, in the absence of rmCXCL1. Hence, the induction of adhesion of d4 Hoxb8-SCF cells occurred specificly through activation of the cells by rmCXCL1.

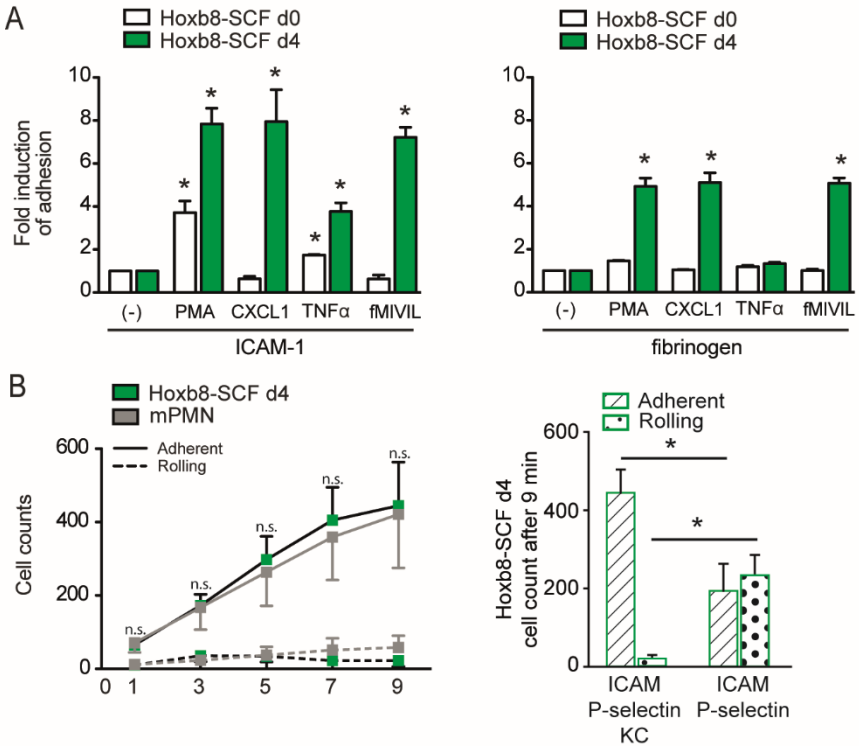

Figure 24. Induction of adhesion of Hoxb8-SCF cells. (A) D0 and d4 Hoxb8-SCF cells on immobilised rmICAM-1 or mfibrinogen were stimulated under static conditions using 100 ng/mL rmTNFα, 100 ng/mL rmCXCL1, 3 mM Mn^{2+}, 100 nM PMA, or 100 nM fMIVIL, or left untreated (-) for negative control. Adherent cells were normalized to untreated d0, or d4 Hoxb8-SCF cells respectively. n = 3. * $p < 0.05$. **(B)** Numbers of rolling and adherent cells of d4 Hoxb8-SCF cells or murine bone marrow-derived PMN under 1 dyne/cm^2 of flow on immobilised rmP-selectin, rmICAM-1 and rmCXCL1 (left panel) at indicated time points and (right panel) after 9 min with rmCXCL1 stimulation or without for control. n = 4. Mean ± SEM. n.s., not significant (d4 Hoxb8-SCF cells to PMN adherent cells), * $p < 0.05$ (adapted from Zehrer et al., 2018[180]).

After successful adhesion, PMN start to migrate along blood vessel walls. To mimic this process *in vitro*, d4 Hoxb8-SCF cells were allowed to migrate on immobilised rmICAM-1 and rmCXCL1 under 1 dyne/cm^2 of shear stress (Fig. 25A). Single cell migration tracks were

analysed for migration velocity and Euclidean distance. Rose plots were used to determine the distribution of migration directions. With a mean migration velocity of 4.19 ± 0.51 µm/min and an Euclidean distance of 24.8 ± 2.66 d4 Hoxb8-SCF migrate with less than half the speed and distance compared to what was previously described for murine PMN under flow conditions (Fig. 25A)[104,187]. However, d4 Hoxb8-SCF cells were able to migrate directionally, as well as against and perpendicular to the direction of flow, identical to what is described for murine PMN[186,187]. When exposed to a chemotactic gradient of rmCXCL1 in the 2D environment of a Zigmond chamber, d4 Hoxb8-SCF cells migrated with a mean velocity of 5.5 ± 0.1 µm/min preferentially in the direction of the higher concentration of the chemoattractant rmCXCL1, as determined by single cell migration tracks and the corresponding rose plots (Fig. 25B). Thus, the behaviour of d4 Hoxb8-SCF cells in the presence of shear stress and chemotactic gradients underline the similarity of d4 Hoxb8-SCF cells to murine bone marrow-derived PMN and further prove their suitability as a tool to study PMN trafficking.

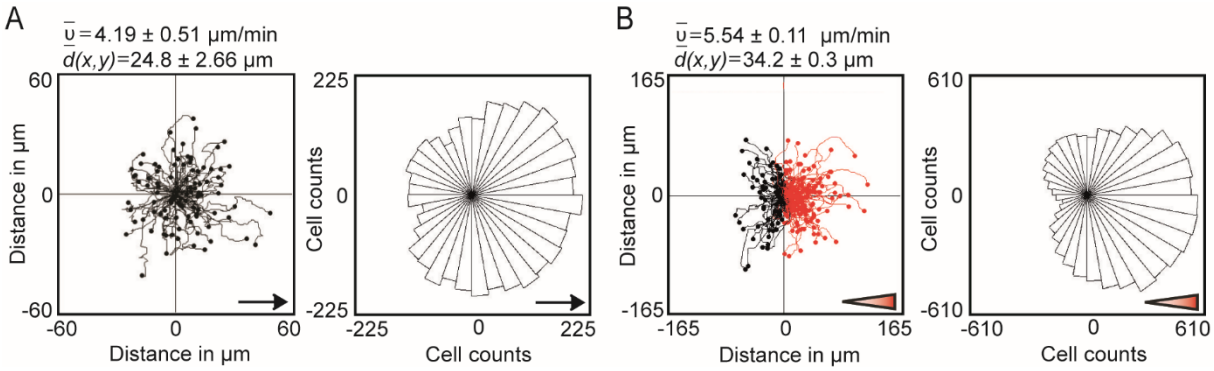

Figure 25. Mechanotactic and chemotactic migration of d4 Hoxb8-SCF cells. **(A)** Mechanotactic migration on immobilised rmICAM-1 and rmCXCL1 under 1 dyne/cm^2 of flow for 10 min. Representative single cell migration tracks and rose plot with indicated mean migration velocity (v) and Euclidean distance *(d(x/y))*. Arrows indicate direction of flow. n = 3 (206 d4 Hoxb8-SCF cells). **(B)** Chemotactic migration of d4 Hoxb8-SCF cells on immobilised rmICAM-1 in Zigmond chambers towards a gradient of rmCXCL1 for 10 min. Triangles indicate orientation of gradients. Representative single cell migration tracks and rose plot with indicated mean migration velocity (v) and Euclidean distance *(d(x/y))*. n = 3 (479 d4 Hoxb8-SCF cells), (adapted from Zehrer et al., 2018[180]).

3.4 Migration of Myh9-EGFP expressing Myh9-knock-down Hoxb8-SCF cell-derived neutrophils

3.4.1 Generation of Hoxb8-SCF cells from *Vav-iCre^{-}/Myh9$^{fl/fl}$*, *Vav-iCre^{+}/Myh9$^{wt/fl}$*, and *Vav-iCre^{+}/Myh9$^{fl/fl}$* foetal liver progenitor cells

To perform rescue experiments, a Myh9-EGFP fusion protein should be expressed in cells with a knock-down in Myh9 expression. As the d4 Hoxb8-SCF cells were successfully evaluated as a suitable tool to study PMN trafficking, the Hoxb8-SCF cells system was employed for this task. Hoxb8-SCF cells were generated from foetal liver progenitor cells of E13 embryos with a *Vav-iCre^{-}/Myh9$^{fl/fl}$*, *Vav-iCre^{+}/Myh9$^{wt/fl}$* and *Vav-iCre^{+}/Myh9$^{fl/fl}$* genotype. The discovery of embryos, but no viable pups, with the *Vav-iCre^{+}/Myh9$^{fl/fl}$* genotype, suggested that mice with this genotype die between E13 during embryogenesis and birth.

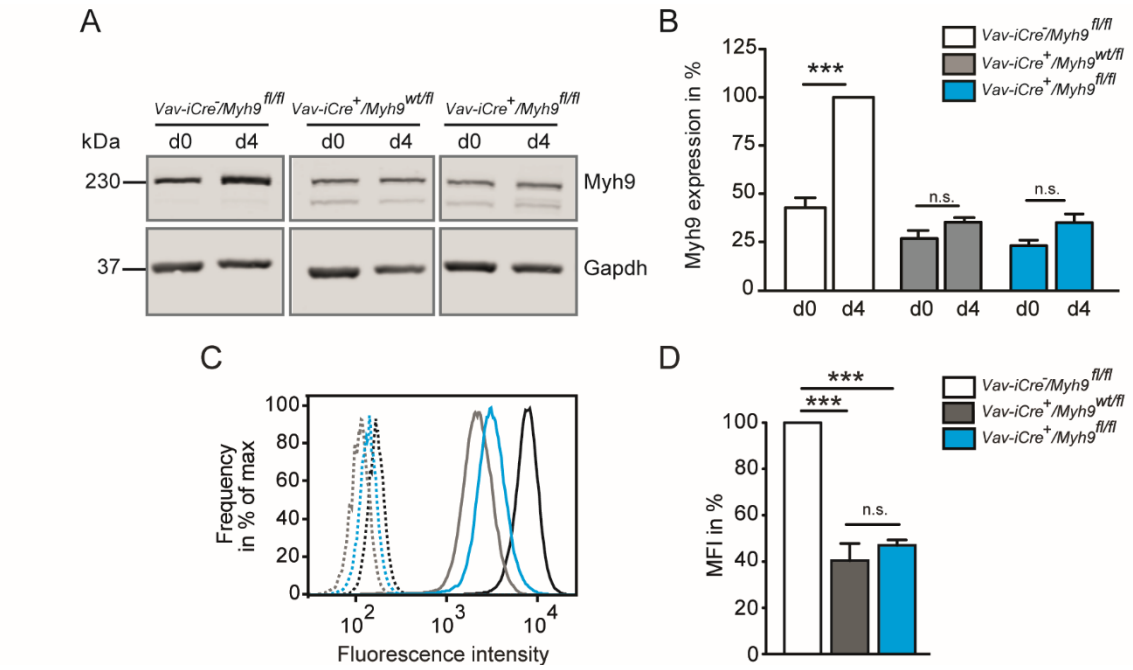

Figure 26. Myh9 expression in Hoxb8-SCF cells generated from foetal liver progenitor cells. (A) Representative western blot of Myh9 expression in cell lysates from foetal liver Hoxb8-SCF d0 and d4 cells derived from *Vav-iCre^{-}/Myh9$^{fl/fl}$* mice and Myh9 knock-down *Vav-iCre^{+}/Myh9$^{wt/fl}$* and *Vav-iCre^{+}/Myh9$^{fl/fl}$* mice. **(B)** Quantitative analysis of Myh9 protein expression. Protein expression of Myh9 was normalized to GAPDH and d4 Hoxb8-SCF *Vav-iCre^{-}/Myh9$^{fl/fl}$* cells (100%). n ≥ 3 **(C)** Flow cytometry histograms of intracellularly stained Myh9 in d4 Hoxb8-SCF cells and isotype controls. **(D)** Quantification of mean fluorescence intensities (MFI) normalized to *Vav-iCre^{-}/Myh9$^{fl/fl}$* cells (100%). n = 3: Mean ± SEM. n.s. not significant, *** $p < 0.001$ (adapted from Zehrer et al., 2018[180]).

To determine the amount of Myh9 protein expressed in these Hoxb8-SCF cell lines, western blotting was performed using cell lysates of Hoxb8-SCF progenitor cells and d4 Hoxb8-SCF cells (Fig. 26A). Unexpectedly, quantification of normalized Myh9 expression revealed that the expression of Myh9 in the undifferentiated Hoxb8-SCF cells was similar between the three genotypes. During differentiation to PMN, control Hoxb8-SCF cells with a *Vav-iCre*$^{-}$*/Myh9*$^{fl/fl}$ genotype increased their Myh9 expression drastically, whereas *Vav-iCre*$^{+}$*/Myh9*$^{wt/fl}$ and *Vav-iCre*$^{+}$*/Myh9*$^{fl/fl}$ Hoxb8-SCF cells failed to increase their Myh9 levels significantly, resulting in a diminished expression of Myh9 in these d4 Hoxb8-SCF cells, with 38.7 ± 4.9% for *Vav-iCre*$^{+}$*/Myh9*$^{wt/fl}$ and 35.4 ± 1.7% for *Vav-iCre*$^{+}$*/Myh9*$^{fl/fl}$ compared to *Vav-iCre*$^{-}$*/Myh9*$^{fl/fl}$ d4 Hoxb8-SCF cells (100%, Fig. 26B). To investigate the expression of Myh9 throughout the populations on a single cell niveau, flow cytometry of intracellular stained Myh9 was performed. Comparison of the histograms for Myh9 in *Vav-iCre*$^{-}$*/Myh9*$^{fl/fl}$, *Vav-iCre*$^{+}$*/Myh9*$^{wt/fl}$ and *Vav-iCre*$^{+}$*/Myh9*$^{fl/fl}$ d4 Hoxb8-SCF cells, allowed an exclusion of heterogeneity within the single populations (Fig. 26C). Quantification of the mean fluorescence intensity values confirmed the significant downregulation of Myh9 determined using western blots in *Vav-iCre*$^{+}$*/Myh9*$^{wt/fl}$ and *Vav-iCre*$^{+}$*/Myh9*$^{fl/fl}$ compared to *Vav-iCre*$^{-}$*/Myh9*$^{fl/fl}$ d4 Hoxb8-SCF cells (Fig. 26D).

The unexpected similar amounts of Myh9 protein in *Vav-iCre*$^{+}$*/Myh9*$^{wt/fl}$ and *Vav-iCre*$^{+}$*/Myh9*$^{fl/fl}$ d4 Hoxb8-SCF cells demanded further investigation of the genetic processes occurring in these cells. Therefore, an additional PCR was performed. In contrast to the originally described genotyping PCR, the forward primer was designed in front of the 5' flox region of the Myh9 exon 1. The reverse primer used was in the same position as in the originally described genotyping PCR and located after the 3' flox region (Fig. 4, methods section). With this new approach wildtype alleles (*Myh9*^{wt}) as well as floxed alleles (*Myh9*^{fl}), and alleles where the Cre recombinase deleted exon 1 (*Myh9*^{del}), could be visualized and distinguished. In Fig. 27A, the original genotyping PCR of the E13 embryos for *Vav-iCre* and *floxed Myh9* is displayed and demonstrates the indicated genotypes. The results of the additionally performed PCR are depicted in Fig. 27B. In the case of the control *Vav-iCre*$^{-}$*/Myh9*$^{fl/fl}$ Hoxb8-SCF cells, one band for the *Myh9*^{fl} allele was visible, as expected. For *Vav-iCre*$^{+}$*/Myh9*$^{wt/fl}$ Hoxb8-SCF cells, a band for the *Myh9*^{wt} and a band for *Myh9*^{del} were found, as expected for hematopoietic cells with active Cre recombinase. Interestingly, in *Vav-iCre*$^{+}$*/Myh9*$^{fl/fl}$ Hoxb8-SCF cells, a band for *Myh9*^{fl} was still present as additionally verified by sequencing, but a strong band for *Myh9*^{del} was also visible. In combination with

the flow cytometry data, this led to the hypothesis that in the pool of *Vav-iCre*$^{+}$*/Myh9*$^{fl/lf}$ Hoxb8-SCF cells, a population with less effective Cre recombination, and therefore only one *Myh9*^{del} allele, had a tremendous selection advantage during proliferation resulting in a heterozygous phenotype of the *Vav-iCre*$^{+}$*/Myh9*$^{fl/fl}$ d4 Hoxb8-SCF cells.

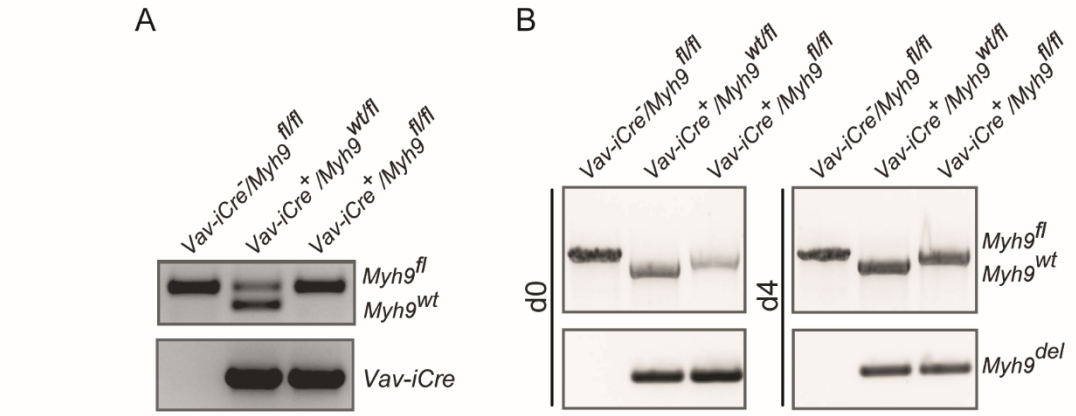

Figure 27. Genotyping PCRs of the Myh9 exon 1 locus (A) Original genotyping of *Vav-iCre* and *Myh9* loci for *Myh9*^{fl} and *Myh9*^{wt}, and *Vav-iCre*$^{+}$. **(B)** Additional PCR of the *Myh9* locus for *Myh9*^{fl}, *Myh9*^{wt} and *Myh9*^{del} in d0 and d4 Hoxb8-SCF cells. Images are representative of 3 independent experiments (adapted from Zehrer et al., 2018[180]).

To exclude the possibility that the reduced amount of Myh9 protein in Hoxb8-SCF cells interferes with the differentiation process towards PMN, *Vav-iCre*$^{-}$*/Myh9*$^{fl/fl}$, *Vav-iCre*$^{+}$*/Myh9*$^{wt/fl}$ and *Vav-iCre*$^{+}$*/Myh9*$^{fl/fl}$ d0 and d4 Hoxb8-SCF cells were analysed for their expression of surface progenitor markers, PMN markers and integrin expression using flow cytometry. The progenitor markers CD34 and c-kit were found to be expressed in all three cell lines before differentiation (d0) and were strongly downregulated after their differentiation towards PMN (d4) (Fig. 28A). On the other hand, Gr-1, Ly6G and CXCR2 were barely expressed in all three d0 Hoxb8-SCF cells lines and, as expected, were upregulated upon differentiation (Fig. 28B). The analysis of integrin expression revealed that CD11a was similarly expressed between all three genotypes and independent of differentiation. In contrast, CD11b was barely expressed in d0 Hoxb8-SCF cells and highly expressed in d4 Hoxb8-SCF of all genotypes, as expected. The integrin subunit CD11c was absent in all three tested cell lines and time points, confirming the absence of CD11c expressing cell types, like dendritic cells. Also, CD18 was found to be expressed in d0 Hoxb8-SCF cells and was upregulated in all three genotypes upon differentiation, as expected (Fig. 28C). This data suggests that the differentiation process towards PMN was equally

successful in *Vav-iCre⁻/Myh9$^{fl/fl}$* and *Vav-iCre⁺/Myh9$^{fl/fl}$*, as well as *Vav-iCre⁺/Myh9$^{wt/fl}$* Hoxb8-SCF cells.

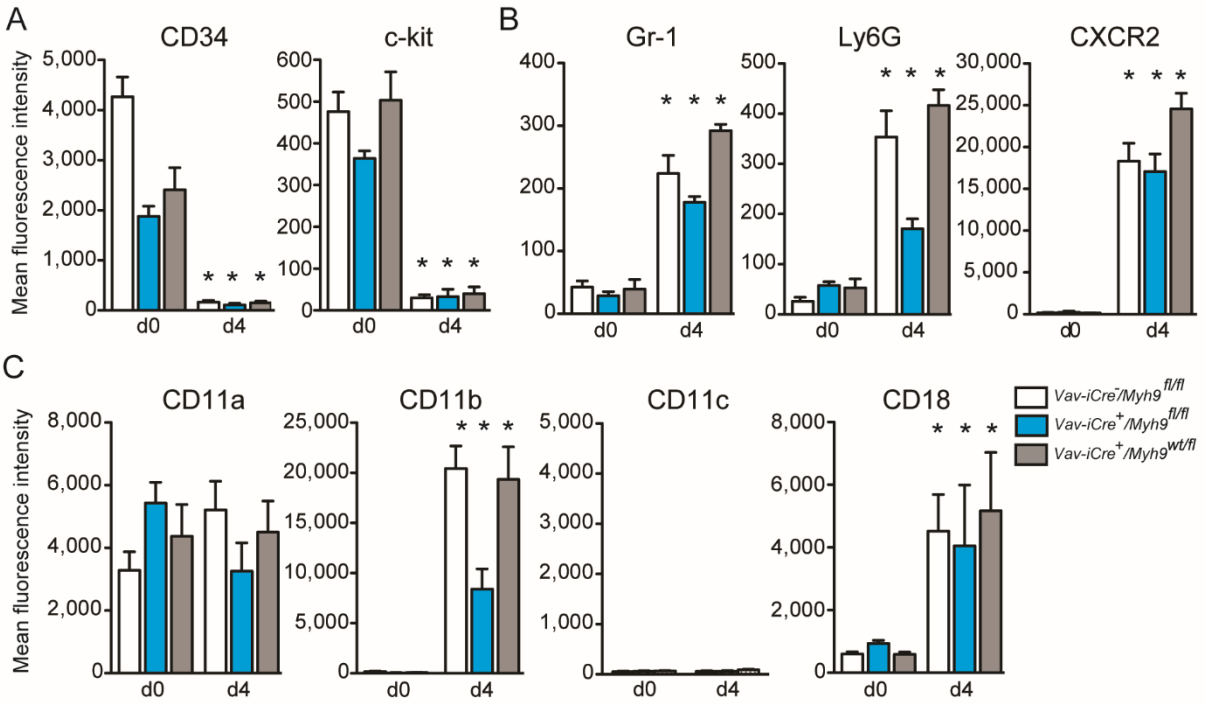

Figure 28. Differentiation profile of foetal liver-derived Hoxb8-SCF cells. D0 and d4 Hoxb8-SCF cells from *Vav-iCre⁻/Myh9$^{fl/fl}$* as well as from *Vav-iCre⁺/Myh9$^{wt/fl}$* and *Vav-iCre⁺/Myh9$^{fl/fl}$* embryos were analysed by flow cytometry using specific, fluorescently labelled antibodies for expression of differentiation markers. **(A)** CD34 and c-kit, **(B)** Gr-1, Ly6G, and CXCR2 and **(C)** CD11a, CD11b, CD11c, and CD18. Mean fluorescence intensity corrected by isotype control. n = 4. Mean ± SEM. * $p < 0.05$.

3.4.2 Generation of a Myh9-EGFP expressing Hoxb8-SCF cell line

Before the generation of a Myh9-EGFP expressing Hoxb8-SCF cell line, the functionality of the #38297 *pMyosin-II-A-GFP* plasmid was confirmed by transfection of HEK-293T cells with the plasmid. Expression of the Myh9-EGFP fusion protein was analysed using confocal microscopy (Fig. 29A). Myh9-EGFP was visible and colocalised with F-actin, as expected. For successful introduction of the EGFP-MyosinII-A DNA into Hoxb8-SCF cells, retroviral transduction was selected. Therefore, EGFP-MyosinII-A was cloned into the retroviral backbone *pMSCV-Puro* proceeding as displayed in Fig. 29B. Primers including restriction sites and 15 bp, overlapping with the backbone, were designed to amplify the region of interest from the *pMyosin-II-A-GFP*. Using the In-Fusion ligase mix, the EcoRI / XhoI opened *pMSCV-Puro* was linked with the PCR fragment. Transformation into competent

bacteria ensured the amplification of the plasmid. In the next step, the purified plasmid was cut with EcoRI to identify successfully ligated *MSCV-Puro-Myosin-II-A-GFP* plasmids by an additionally appearing band (Fig. 29C lane B) in contrast to a linearized empty backbone (Fig. 29C lane A).

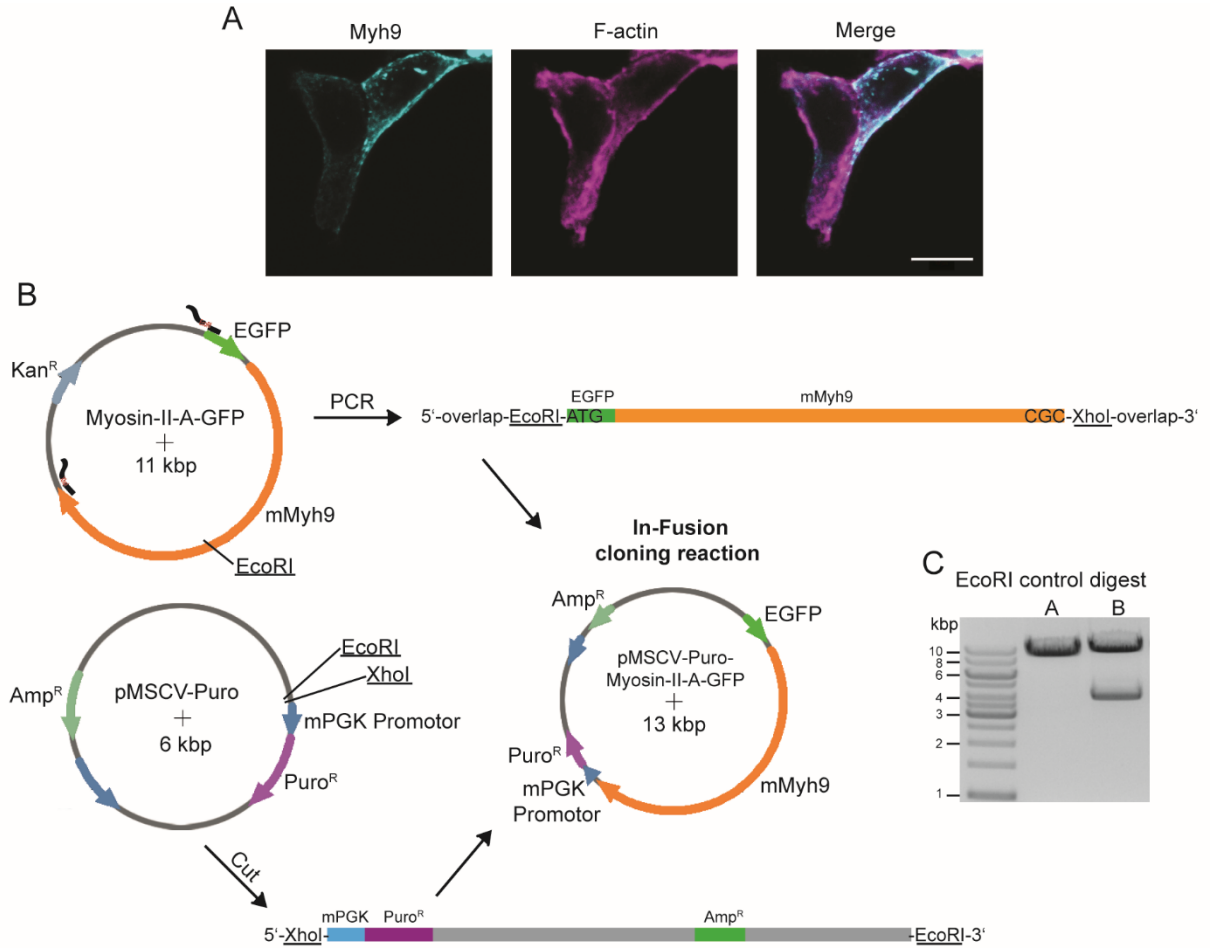

Figure 29. Generation of *pMSCV-Puro-Myosin-II-A-GFP*. (A) Microscopy of two HEK-293T cells. One cell successfully transfected with p*Myosin-II-A-GFP* (turquoise, left picture), F-actin staining in both cells (magenta, middle picture) and colocalisation of Myh9 and F-actin in the one Myh9 expressing cell (merge, white, right picture) Representative images of 2 independent experiments. Scale bar, 10 µm (adapted from Zehrer et al., 2018[180]). **(B)** Schematic for the generation of *pMSCV-Puro-Myosin-II-A-GFP*. **(A)** The retroviral backbone pMSCV-Puro was opened using EcoRI and XhoI restriction enzymes. Myh9-EGFP was extracted from the expression plasmid by PCR using primers including the restriction site for EcoRI or XhoI, and additionally overlapping sequences with the *pMSCV-Puro* vector. These compatible ends enable recombination and fusion of the two linearized DNA strands in the In-Fusion cloning reaction to the *MSCV-Puro-pMyosin-II-A-GFP* plasmid. **(B)** Successful cloning was confirmed by control digest with EcoRI. The two expected bands with 9.174 bp and 3.786 bp, can be seen in lane B of the representative image.

The *MSCV-Puro-Myosin-II-A-GFP* vector was sequenced (data not shown) and further used to generate retrovirus encoding for Myh9-EGFP. *Vav-iCre*$^{+}$*/Myh9*$^{fl/fl}$ Hoxb8-SCF cells were defined as *knock-down (KD)* cells and transduced with the virus. After Puromycin selection, successful transduction was confirmed via flow cytometry (Fig. 30A). Subsequently, EGFP positive cells were sorted from the Hoxb8-SCF cell pool (Fig. 30A). To confirm the expression of the fusion protein, western blotting for EGFP and Myh9 was performed using lysates of the sorted Hoxb8-SCF cell population and non-transduced *Myh9-KD* Hoxb8-SCF cells (Fig. 30B). As expected, endogenous Myh9 was detected in undifferentiated and differentiated *Myh9-KD* cells, whereas the fusion protein Myh9-EGFP was only identified in the transduced undifferentiated and differentiated *Myh9-KD* Hoxb8-SCF cells. These cells were defined as *Myh9-RES* Hoxb8-SCF cells.

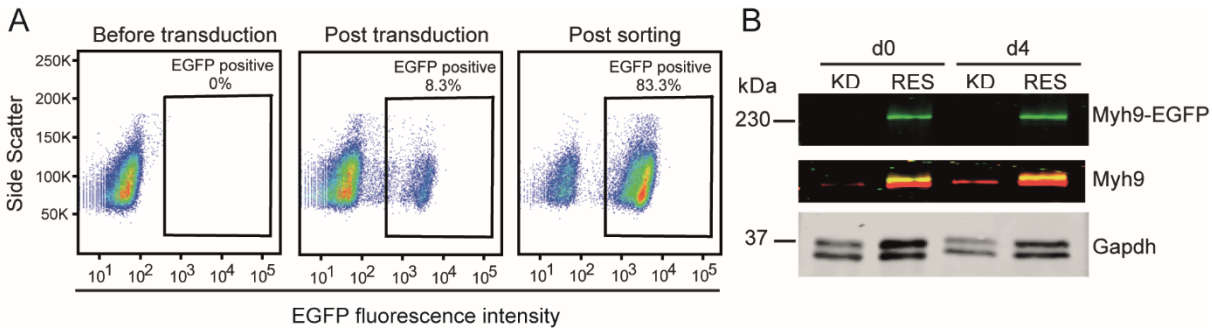

Figure 30. Generation of Myh9-EGFP expressing *Myh9 kock-down (KD)* Hoxb8-SCF cells. (A) Flow cytometry for EGFP intensity in foetal liver *Myh9-KD*-Hoxb8-SCF cells, before (left panel) and after transduction (middle panel) with p*MSCV-Puro-Myosin-II-A-GFP*, as well as after sorting for EGFP positive cells (right panel). Numbers indicate percent of total cells analysed (100%) in each panel. **(B)** Representative western blot indicating the expression of Myh9-EGFP (green) in transduced *Myh9-KD* Hoxb8-SCF cells (*Myh9-RES* Hoxb8-SCF cells, *RES*) before and after differentiation. Endogenous Myh9 expression (red) in *Myh9-KD* Hoxb8-SCF cells (*KD*) and *Myh9-RES* Hoxb8-SCF cells (*RES*). Overlapping signal of Myh9-EGFP (green) and endogenous Myh9 (red) presented as merge (yellow) (adapted from Zehrer et al., 2018[180]).

3.4.3 Rescue of migration in Myh9-RES Hoxb8-SCF cells

To investigate the potential rescue function of the introduced fusion protein, the migratory capacity of *Vav-iCre*$^{-}$*/Myh9*$^{fl/fl}$ (*control*), *Vav-iCre*$^{+}$*/Myh9*$^{wt/fl}$ (*Myh9-cHet*), *Vav-iCre*$^{+}$*/Myh9*$^{fl/fl}$ (*Myh9-KD)* and *Myh9-RES* Hoxb8-SCF cell-derived neutrophils (dHoxb8 cells) was analysed in a 2D environment using 1 dyne/cm^2 shear stress on immobilised rmICAM-1 and rmCXCL1. Single cell migration tracks revealed a longer migrated distance for *control* and

Myh9-RES dHoxb8 cells in comparison to *Myh9-KD* and *Myh9-cHet* dHoxb8 cells (Fig. 31A). This finding was confirmed by quantitative analysis of the migration velocity and the Euclidean distance (Fig. 31B). Specifically, *control* and *Myh9-RES* dHoxb8 cells reached mean velocities of 3.7 ± 0.2 and 3.3 ± 0.5 µm/min SEM, whereas *Myh9-KD* and *Myh9-cHet* dHoxb8 cells migrated significantly slower with 1.9 ± 0.1 and 2.4 ± 0.1 µm/min. The same picture emerged when the Euclidean distance was compared. Here, *control* and *Myh9-RES* dHoxb8 cells exhibited an Euclidean distance of 19.4 ± 2.1 µm SEM and 19.4 ± 1.7 µm, whereas the Euclidean distance in *Myh9-KD* and *Myh9-cHet* dHoxb8 cells was significantly lower with 8.8 ± 0.4 and 12.0 ± 0.2 µm (Fig. 31B). These results were in line with the experimental outcomes for bone marrow-derived PMN of *control* and *Myh9-cHet* mice, where *Myh9-cHet* PMN displayed reduced migratory capacity in a 2D environment. Furthermore, these results proved that the introduced Myh9-EGFP fusion protein rescued the 2D migration defect observed in *Myh9-KD* dHoxb8 cells.

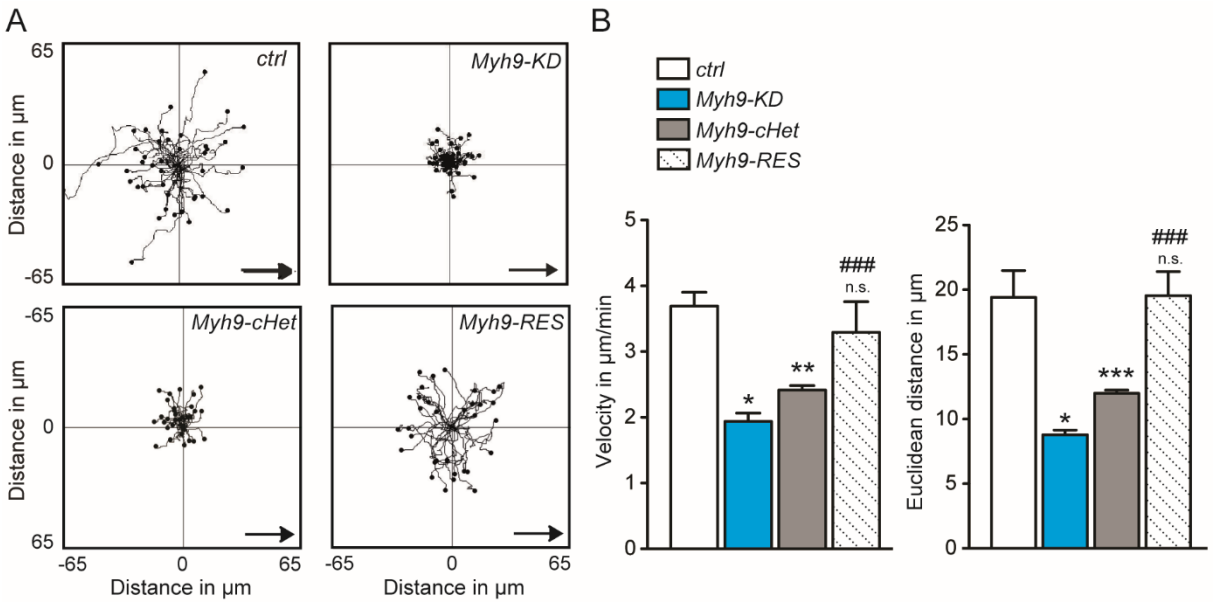

Figure 31. Expression of Myh9-EGFP in *Myh9-KD* dHoxb8 cells rescued migratory defects in 2D environment. (A) Single cell migration tracks of *control* (*ctrl)*, *Myh9-KD*, *Myh9-cHet* and *Myh9-RES* dHoxb8 cells after 10 min under shear stress of 1 dyne/cm^2 on immobilised rmICAM-1 and rmCXCL1. Arrows indicate direction of flow. Displayed are single cell migration tracks of representative experiments. **(B)** Quantitative analysis of migration velocity and Euclidean distance. Mean ± SEM, n > 3 (395 *ctrl*, 734 *Myh9-KD*, 268 *Myh9-cHet* and 233 *Myh9-RES* dHoxb8 cells). n.s. not significant, *p < 0.05, ** p < 0.01, *** p < 0.001, ### p < 0.001 compared to *Myh9-KD* dHoxb8 cells (adapted from Zehrer et al., 2018[180]).

To investigate whether *Myh9-RES* cells also benefit from the introduced Myh9-EGFP fusion protein in a 3D environment, *Myh9-KD* and *Myh9-RES* dHoxb8 cells were allowed to migrate in a 1.5 mg/mL collagen gel towards a gradient of rmCXCL1. On the basis of single cell migration tracks and rose plots, it was found that both cell types sensed and orientated towards the gradient (Fig 32A and B). This was confirmed quantitatively using the parameters directness and forwards migration index in x direction (Fig. 32C). Here, no significant difference was detected between *Myh9-KD* and *Myh9-RES* dHoxb8 cells. The positive values for the migration index in x direction confirmed migration in the direction of the increasing rmCXCL1 concentration. In contrast to this, *Myh9-KD* dHoxb8 cells were significantly slower and migrated less far than the *Myh9-RES* dHoxb8 cells (Fig. 32A, C): *Myh9-KD* cells exhibited 22.5 ± 3.4 µm Euclidean distance with a velocity of 4.3 ± 0.6 µm/min, whereas the introduced Myh9-EGFP increased the migratory capacity of *Myh9-RES* cells to 37 ± 2.6 µm Euclidean distance and 6.2 ± 0.2 µm/min migration velocity. It was concluded that *Myh9-RES* dHoxb8 cells indeed benefitted from the introduced Myh9-EGFP in terms of migration speed and distance, compared to *Myh9-KD* dHoxb8 cells in 3D environment.

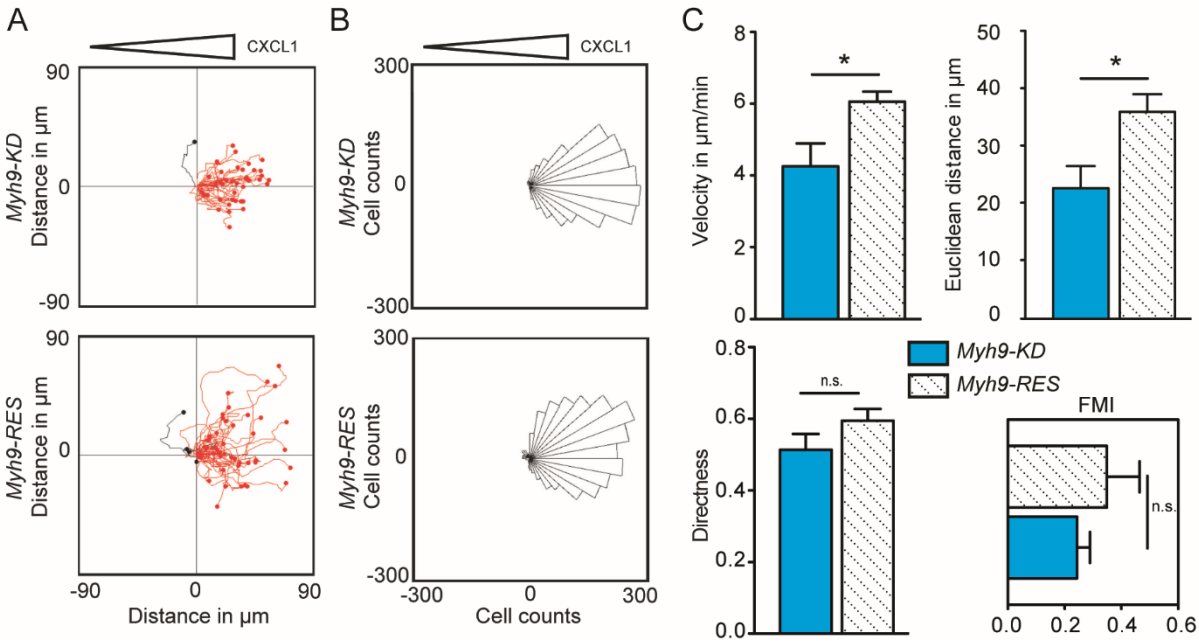

Figure 32. Migration behaviour in 3D environment was recovered by the expression of Myh9-EGFP in *Myh9-KD* dHoxb8 cells. Migration in 3D collagen networks (1.5 mg/mL) of *Myh9-KD* and *Myh9-RES* dHoxb8 cells towards gradients of rmCXCL1 for 10 min. **(A)** Representative exemplary single cell migration tracks and **(B)** Rose plots. Triangles indicate orientation of gradients. **(C)** Migration velocity and Euclidean distance, as well as directness and forward migration index (x) (FMI). Mean ± SEM, n = 4 (503 *Myh9-KD* and 320 *Myh9-RES* dHoxb8 cells). n.s. not significant, * $p < 0.05$ (adapted from Zehrer et al., 2018[180]).

3.4.4 Role of Myh9 during 3D migration

To elucidate the role of Myh9 during 3D migration in collagen meshwork towards a chemotactic gradient of rmCXCL1, the spatial and temporal dynamics of Myh9 were analysed using live-cell spinning disk confocal microscopy of Myh9-EGFP expressing *Myh9-RES* dHoxb8 cells. First, differences in Myh9 localisation during fast, medium, and slow migration were investigated.

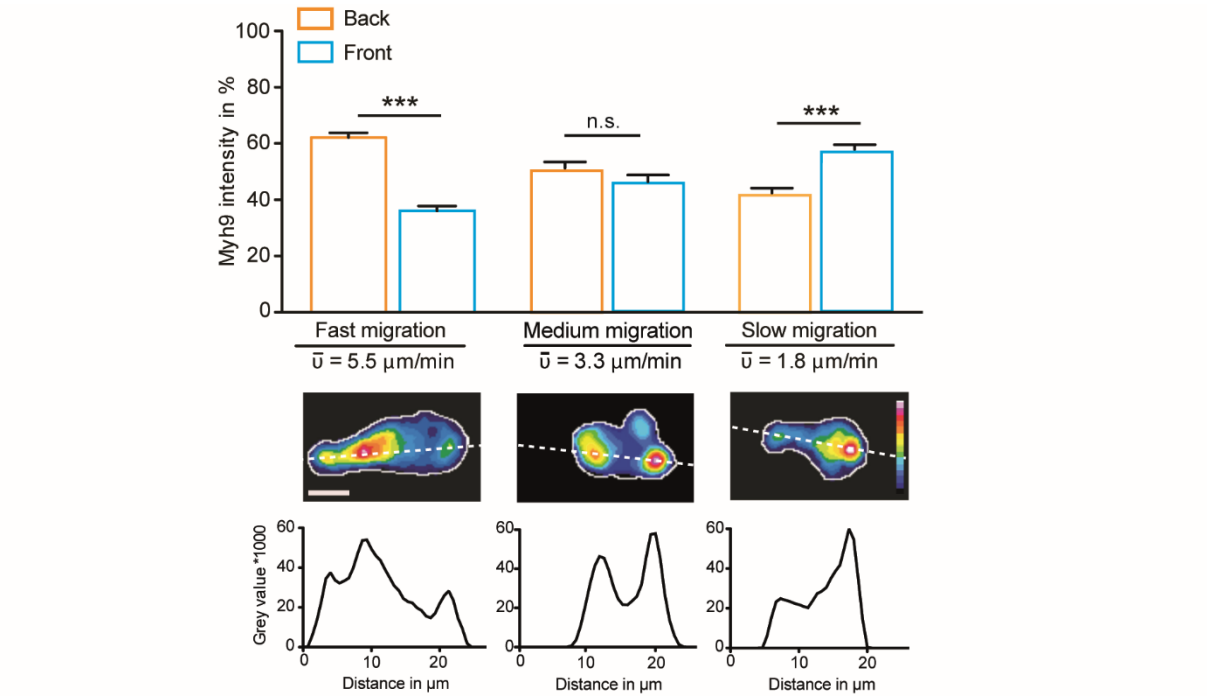

Figure 33. Myh9-EGFP distribution during different migration speeds in 3D environment. Upper panel: Relative distribution of Myh9 to the front and back of *Myh9-RES* dHoxb8 cells compared to whole cell intensity of Myh9-EGFP (100%) during fast, medium, or slow migration. Cell area was equally split into front and back (n=23 for fast migration, n=17 for medium migration, n=28 for slow migration). Middle and lower panel: Representative fast, medium, and slow migrating cells with Myh9 in pseudocolours and intensity profile along segmented line (adapted from Zehrer et al., 2018[180]).

The fastest, a medium, and the slowest migration velocity were detected for each individual cell and the intracellular localisation of Myh9 was analysed at these three time points (Fig. 33). Fast migrating *Myh9-RES* dHoxb8 cells displayed a mean velocity of 5.5 ± 0.6 µm/min and localised Myh9 mainly towards the rear of the cell. *Myh9-RES* dHoxb8 cells migrating with a medium migration velocity of 3.3 ± 0.2 µm/min located Myh9-EGFP equally to the front and the back of the cell[180]. Slow migrating *Myh9-RES* dHoxb8 cells with a velocity of 1.8 ± 0.2 µm/min positioned Myh9 more to the front of the cell. This analysis was

visualised based on one representative fast, one medium, and one slow migrating cell using Myh9 intensity profiling along a horizontal axis through the cell (Fig. 33 lower panel).

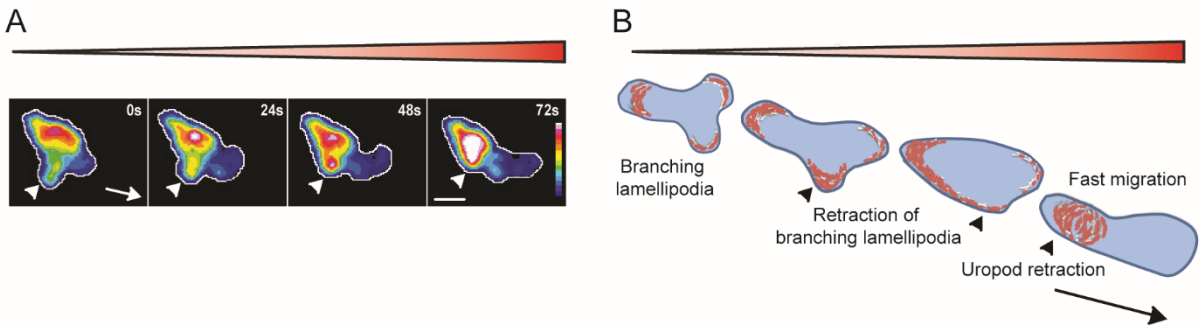

Figure 34. Myh9-EGFP specifically localised at sites of cell membrane retraction during 3D migration. (A) Representative pseudocoloured snapshots at indicated time points during 3D migration of *Myh9-RES* dHoxb8 cells demonstrating the subcellular localisation of Myh9. Triangles indicate orientation of gradients. Arrow indicates direction of migration, arrowheads point towards retracting membrane sites. Scale bar, 5 µm. **(B)** Model of Myh9 localisation and function during migration: retraction of branching lammelipodia and the uropod (adapted from Zehrer et al., 2018[180])

Furthermore, the analysis of the recorded videos revealed that *Myh9-RES* dHox8 cells enriched Myh9 in branching lamellipodia and at the rear of the cells while retracting these cell compartments (Fig. 34A). Branching lamellipodia were retracted upon the enrichment of Myh9, leading to a consolidation of the leading edge towards the chemoattractant. Taken together, these findings suggest a model where Myh9 exerts its function specifically at sites of membrane retraction for example branching lamellipodia and retraction of the rear of the cell (Fig. 34B)[180].

In summary, the genetic approach to knock-down Myh9 in the hematopoietic system of mice resulted in a reduction of Myh9 expression down to less than 30% in PMN. With his residual expression PMN were not able to migrate or to transmigrate as efficient as *control* PMN *in vitro*. Additionally, the reduced amount of Myh9 was found to influence the subcellular localisation of F-actin and Myh9, as well as their interaction strength. The *in vitro* results were confirmed in two *in vivo* models. Here, the *Myh9-cHet* PMN displayed reduced extravasation and migratory speed compared to *control* PMN. Using bone marrow chimeric mice, a cell-intrinsic defect of PMN with reduced Myh9 expression was identified. Using the Hoxb8-SCF cell model and by expression of Myh9-EGFP in *Myh9-KD* cells, the spatiotemporal distribution of Myh9 during migration was elucidated.

4 Discussion

In the past, studies on the functional impact of Myh9 in polymorphonuclear neutrophils (PMN) have been limited to pharmacological inhibitors. In this study, a genetic approach to knock-down Myh9 in PMN was applied using *Vav-iCre*$^{+}$*/Myh9*$^{wt/fl}$ (*Myh9-cHet*) mice. Furthermore, a Myh9 knock-down Hoxb8-SCF cell line and a cell line expressing rescuing Myh9-EGFP were established. The data demonstrated the importance of Myh9 for 2D migration, transmigration, and 3D migration *in vitro*. Using STED nanoscopy, dysregulation of F-actin and Myh9 dynamics were found upon Myh9 downregulation. *In vivo*, PMN with a downregulation of Myh9 demonstrated defects in extravasation and interstitial migration in two different models, the CXCL1-induced peritonitis model and a laser-induced injury model in the ear. Bone marrow chimeras confirmed the cell-intrinsic migration defect of PMN with a downregulation in Myh9. The versatile subcellular localisation of Myh9 and its role in membrane retraction during migration were elucidated using live cell imaging[180].

4.1 Effect of pharmacological inhibition of class II non-muscle myosin on PMN migration

In the first part of the study, PMN isolated from the bone marrow of wildtype mice were treated with pn-blebbistatin. This cell-permeable compound works as an non-competitive inhibitor of the ATPase activity of class II myosins and was developed to eliminate the photo- and cytotoxic side effects of the previously used pharmacological inhibitor blebbistatin[173,174]. Previous studies were performed under static conditions *in vitro.* Therefore, it remained to be explored whether the published results reflect the situation under flow conditions mimicking the physiological conditions *in vivo*. In the present study, inhibition of Myh9 had no effect on the number of rolling and adherent cells during induction of adhesion under flow conditions[180]. These results were in line with reports for T cells and indicated that Myh9 was dispensable for the induction of adhesion of PMN under these conditions[159]. During 2D migration under flow conditions, pn-blebbistatin-treated PMN exhibited a phenotype with multiple pseudopods and an elongated uropod as well as reduced migration speed and Euclidian distance. These findings were in accordance with results under static conditions which also observed a diminished migration speed and the elongated cell shape[93,94,178]. Both, the migration velocity and the elongated phenotype were demonstrated to depend on the concentration of pn-blebbistatin. This corresponds well with reports for migration behaviour of blebbistatin-treated human umbilical vein endothelial cells, smooth muscle cells and macrophages, which also described a dose-dependent effect of blebbistatin on migration[196,199].

In the present study, spreading of pn-blebbistatin-treated PMN resulted in an increased cell area compared to control PMN. This observation was in line with the findings of Jacobelli et al. in blebbistatin-treated T cells[160]. Consistent with other studies showing that blebbistatin-treated HL-60 cells or T cells failed to properly transmigrate through a monolayer of endothelial cells, pn-blebbistatin-treated PMN demonstrated inhibited transmigration[146,158]. In contrast to those studies analysing trans-endothelial migration, in the present work, a reductionist transmigration set-up using pn-blebbistatin-treated PMN and a rmICAM-1 coated polycarbonate membrane was employed to study transmigration. Also, pn-blebbistatin-treated PMN were able to deform and insert their nuclei into the pores of the membrane (data not shown), which is in line with previous reports for blebbistatin-treated PMN. However, transmigrating T cells were reported to fail in squeezing their nuclei between endothelial cells upon blebbistatin treatment[146,158], emphasising the necessity to study the distinct roles of Myh9 in each specific cell type.

4.2 Impact of Myh9 downregulation on PMN migration

To specifically knock-out Myh9 in the hematopoietic system, the Vav-iCre system and *Myh9$^{fl/fl}$* mice were used. As none of the living offspring had the desired *Vav-iCre^{+}/Myh9$^{fl/fl}$* genotype, the theory that the deletion of Myh9 in the progenitor cells of the hematopoietic system is lethal during embryogenesis, was established. This was in accordance with reports of Shin et al. using an inducible Myh9 knock-out in bone marrow chimeras. Upon Myh9 deletion, progenitor cells in the bone marrow stopped dividing and performed progressive apoptosis, causing a drop in peripheral blood cells[144]. In the Vav-iCre mouse model, Cre recombinase is active from day E11.5 in all progenitor cells of leukocytes, erythrocytes, and in megakaryocytes resulting in a knock-out of Myh9 in these cells[179,180,200,201]. Based on this knowledge, it is likely that *Vav-iCre^{+}/Myh9$^{fl/fl}$* foeti died due to a lack of blood cells, as a consequence of missing bone marrow progenitor cells. Nevertheless, *Vav-iCre^{+}/Myh9$^{wt/fl}$* (*Myh9-cHet*) mice with one Myh9 allele still present were viable and demonstrated an unexpected low amount of Myh9 protein in their PMN population compared to *Vav-iCre^{-}/Myh9$^{wt/fl}$* (*control)* mice. With one allele missing, a reduction of Myh9 to 50% was expected, but a reduction of approximately 75% compared to *control* PMN (100%) was detected[180]. Similar to the observations with pn-blebbistatin-treated PMN, PMN isolated from the bone marrow of *Myh9-cHet* mice exhibited migration defects with reduced migration velocity and Euclidean distance on rmICAM-1 coated surfaces and in 3D collagen environment. Interestingly, the prominent phenotype with multiple pseudopods and an

elongated uropod, seen in 2D migration in pn-blebbistatin-treated PMN as well as in previous reports for blebbistatin-treated murine PMN in 3D migration[87], was absent in *Myh9-cHet* PMN. In line with the dose-dependent effects of pn-blebbistatin, a dose-dependent effect of Myh9 for migration behaviour seems plausible and one could speculate that the residual amount of Myh9 was sufficient to prevent the phenotypic failure. Similarly, a dose-dependent effect of Kindlin-3 on murine PMN function and a minimal threshold amount of Kindlin-3 for survival was observed[202]. In the present study, the influence of reduced Myh9 expression on integrin affinity seemed unlikely, as migration defects of *Myh9-cHet* PMN occurred, not just on 2D surfaces, but also in 3D collagen environment where migration can occur integrin independent[87]. This theory was supported by the results of the adhesion strengthening assay under flow conditions. Here, integrins in the high affinity conformation are crucial for resisting increasing shear stress rates and no differences between *Myh9-cHet* and *control* PMN were detected. This finding was in slight contrast to a report for T cells, finding increased numbers of adherent Myh9 knock-out T cells over wildtype T cells *in vitro* and *in vivo*[159]. This discrepancy could be the consequence of the residual amount of Myh9 in the PMN in this present study compared to the complete knock-out of Myh9 in the T cell study. In accordance with the results for pn-blebbistatin-treated PMN, as well as published results for Myh9 knock-out T cells, *Myh9-cHet* PMN displayed less efficient transmigration through 3 µm membrane pores, and 8 µm membrane pores coated with a monolayer of endothelial cells, compared to *control* PMN[158]. Defects in maturation, potentially contributing to the migration defects, were excluded by comparison of extracellular PMN markers and nuclear morphology between *Myh9-cHet* and *control* PMN.

The subcellular localisation of F-actin and Myh9 during 2D migration of *control* and *Myh9-cHet* PMN was investigated to elucidate the mechanisms behind the reduced migratory capacity of *Myh9-cHet* PMN. Here, *control* PMN showed the well-characterised F-actin distribution to the front and rear of the cell[94,104,178,187]. Myh9 was visualized at the leading edge and the uropod of these cells, as described previously for migrating PMN[178,203]. This distribution pattern was significantly changed in *Myh9-cHet* PMN. Specifically, F-actin was no longer accumulated at the leading edge of the cell but enriched at the trailing edge. Interestingly, the remaining Myh9 in *Myh9-cHet* PMN did not distribute equally to the previous locations identified in *control* PMN but concentrated in one spot close to the rear of the PMN. These findings were in line with observations of Eddy et al, describing a re-location of F-actin and Myh9 out of the lamellipodium and towards the uropod of migrating PMN after treatment with BDM[178]. Also, blebbistatin-treated endothelial cells displayed disorganized

F actin structures composed of short F-actin bundles instead of long F-actin fibres[140]. A randomization approach investigating the dependence of F-actin localisation to Myh9 distribution, revealed that in *control* PMN, F-actin distributed dependent on Myh9 in the front and back of the cell, whereas upon downregulation of Myh9, the interaction strength of F-actin/Myh9 dropped significantly in the front of the cell, suggesting disturbed F-actin dynamics in the front of migrating PMN due to Myh9 downregulation[180].

In the past, studies investigating the role of Myh9 in PMN were limited to *in vitro* assays as the established pharmacological inhibitors are problematic in systemic application *in vivo* and for live cell imaging[173,204]. The genetic model of Myh9 knock-down in hematopoietic cells permitted *in vivo* investigations in this study. The similarity between *control* and *Myh9-cHet* mice in their WBC counts provided the basis for correct evaluation of the *in vivo* results. In a model of laser-induced sterile injury in the skin of the ear, *in vivo* life-cell imaging revealed that *Myh9-cHet* mice had a drastic reduction in extravasated PMN compared to *control* mice in the observed 40 min after induction of injury. This indicated that PMN with reduced Myh9 expression extravasated less efficiently than *control* PMN *in vivo*. Furthermore, this model enabled the assessment of migration velocity in interstitial tissue *in vivo* of PMN with reduced Myh9 expression. Here, the defects observed in 3D collagen environment *in vitro* were confirmed. *Myh9-cHet* PMN demonstrated a significant decline in migration velocity and Euclidean distance *in vivo* compared to *control* PMN. This finding was similar to studies in mice with Myh9-deficient T cells, showing less intra-lymph node migration compared to *control* T cells[77,159]. In a second *in vivo* model, the rmCXCL1-induced peritonitis model, the negative consequences of reduced Myh9 on extravasation for PMN were confirmed. In accordance with the *in vitro* findings, significantly less PMN extravasated into the peritoneum in *Myh9-cHet* mice compared to *control* mice, highlighting the importance of Myh9 for PMN recruitment to sites of inflammation during acute inflammation.

To test whether these observed effects were due to a cell-intrinsic defect in PMN with reduced Myh9, or if other hematopoietic cells with a reduction in Myh9 expression influence the PMN, mixed bone marrow chimeras from CD45.1 wildtype and CD45.2 *Myh9-cHet* mice, as well as appropriate control chimeras, were generated and rmCXCL1-induced peritonitis was performed. The CD45 congenic marker system is a highly utilized technique to track hematopoietic cells after bone marrow transplantation and to efficiently distinguish between donor and recipient cells[194,205]. Since both, donor and recipient cells, develop in the same environment, any defects in differentiation or function indicate a cell-intrinsic defect[194,205,206]. Successful engraftment of the bone marrow was verified by analysis WBC counts between

WT→WT, HET→WT, and MIX→WT chimeras. The distribution of CD45.1 and CD45.2 was found as expected confirming the depletion of recipient bone marrow and demonstrating that bone marrow cells from *Myh9-cHet* mice had no disadvantage in repopulating the host bone marrow or to contribute to the blood leukocyte pool. The evaluation of the peritoneal lavage, 4 h after rmCXCL1 application, revealed similar diminished extravasation in the HET→WT, and MIX→WT chimeras compared to the WT→WT control bone marrow chimeras. The reduced extravasation in the HET→WT model verified the results observed in *Myh9-cHet* mice and excluded an influence of Cre activity in other than hematopoietic cells. The unexpected reduction of extravasated PMN in the MIX→WT chimeras indicated a cell-intrinsic defect of PMN with reduced Myh9 expression, as the presence of CD45.1 wildtype PMN could not rescue the observed extravasation defect. The distribution of CD45.1 and CD45.2 expressing PMN in the peritoneal lavage was unchanged compared to the distribution determined in the blood before the start of the experiment. In combination with the reduced numbers of extravasated PMN in the MIX→WT model, a dominant negative jamming effect of the *Myh9-cHet* PMN was hypothesized. Here, the *Myh9-cHet*-derived PMN could block the passages for the wildtype PMN so that wildtype PMN can't exhaust their potential for extravasation. In summary, these results indicate a cell-intrinsic migration defect of the *Myh9-cHet* PMN and that these cells potentially influence the transmigration behaviour of wildtype PMN negatively[180].

4.3 Hoxb8–SCF cell-derived neutrophils as a valid tool to study PMN trafficking

To perform essential rescue experiments, the Hoxb8-SCF cell system should be applied[197,198]. In the present study, the differentiation of Hoxb8-SCF cells to Hoxb8-SCF cell-derived neutrophils (dHoxb8 cells) was optimized for d4. Longer differentiation options were dismissed, as the expression of CD11b and CXCR2 were already induced at d4 and the percentage of living cells drastically dropped after d4, resulting in increasing amounts of dead cells with potential negative effects on surviving cells. The phenotype of undifferentiated Hoxb8-SCF cells and dHoxb8 cell was analysed and dHoxb8 cells were discovered to have a very similar appearance to murine bone marrow-derived PMN. To apply these dHoxb8 cells as a tool to study PMN trafficking, these cells needed to behave similarly to PMN. Hence, their response upon stimulation regarding integrin upregulation, induction of adhesion under static and flow conditions, migration under flow conditions, as well as chemotaxis was tested. Interestingly, even undifferentiated Hoxb8-SCF cells were able to bind to rmICAM-1 under

static conditions, due to their constitutive expression of LFA-1, when stimulated with PMA and TNFα, but not with the PMN activators rmCXCL1 and fMIVIL. Unexpectedly, dHoxb8 cells stimulated with TNFα seemed to fail to adhere on mfibrinogen coated surfaces. However, under physiological conditions, TNFα operates as an activator of endothelial cells, acting mostly indirect on PMN[23,25,53]. Therefore, the stimulation time of 5 min given to the dHoxb8 cells to adhere, may not have been long enough to induce sufficient Mac-1 upregulation and activation.

Importantly, under flow conditions, dHoxb8 cells adhered as efficiently as PMN to rmICAM-1 coated surfaces upon stimulation with immobilised rmCXCL1. Of particular importance was the ability of dHoxb8 cells to sense and orientate to a chemotactic gradient and the observation that dHoxb8 cells were able to migrate under flow conditions perpendicular to, against and with the direction of flow. Notably, their migration velocity was slower compared to PMN. This may be due to their increased cell area in contact with the surface compared to PMN, which may cause increased adhesion force. In summary, the analysis in functional assays and their phenotypic similarity to murine bone marrow-derived PMN, demonstrated the potential of dHoxb8 cells to serve as a useful tool to study processes like PMN activation and trafficking.

4.4 Myh9 enrichment at sites of cell membrane retraction

To ensure the same genetic background for the Hoxb8-SCF cells as in the mice used for the performed *in vitro* and *in vivo* experiments, Hoxb8-SCF cells were generated from E13 foeti of a *Vav-iCre^{+}/Myh9$^{wt/fl}$, Vav-iCre^{-}/Myh9$^{fl/fl}$* breeding pair. Interestingly, at this day during embryogenesis, just before the onset of the shift of the definite haematopoiesis from the foetal liver to the bone marrow, viable foeti with a *Vav-iCre^{+}/Myh9$^{fl/fl}$* genotype were discovered. Hence, Hoxb8-SCF cells from foetal liver progenitor cells of *Vav-iCre^{-}/Myh9$^{fl/fl}$*, *Vav-iCre^{+}/Myh9$^{wt/fl}$* and *Vav-iCre^{+}/Myh9$^{fl/fl}$* foeti were generated.

During the establishment of the cell lines, half of the generated *Vav-iCre^{+}/Myh9$^{fl/fl}$* Hoxb8-SCF cell lines stopped dividing and died (data not shown). The surviving cell lines expressed Myh9 comparable to the Hoxb8-SCF cells generated from *Vav-iCre^{+}/Myh9$^{wt/fl}$* and *Vav-iCre^{-}/Myh9$^{fl/fl}$* foetal livers, leading to the theory that only cells with a certain amount of Myh9 survived the multiple cell divisions. This theory is in line with previous reports for T cells, megakaryocytes and hematopoietic progenitor cells. Specifically, T cell specific knock-out of Myh9 led to defects in cell division resulting in multi-nucleated cells and increased cell death of T cells[158,159]. Megakaryocytes with inhibited NMII activity displayed

enhanced polyploidy compared to control megakaryocytes and treatment of $CD34^+$ common potent progenitor cells with blebbistatin caused cytokinesis-associated cell death of these cells[144,207].

Upon differentiation towards PMN, differences in the Myh9 expression between the *Vav iCre$^+$/Myh9$^{wt/fl}$ (Myh9-cHet), Vav-iCre$^+$/Myh9$^{fl/fl}$* and *Vav-iCre$^-$/Myh9$^{fl/fl}$ (control)* Hoxb8-SCF cells were uncovered using the western blot technique. The reported upregulation of Myh9 during the differentiation towards PMN only occurred in *control* but not in *Myh9-cHet* and *Vav-iCre$^+$/Myh9$^{fl/fl}$* Hoxb8-SCF cells[144,172]. *Vav-iCre$^+$/Myh9$^{fl/fl}$* Hoxb8-SCF cells were therefore defined as *Myh9-knock-down (KD)* cells. Flow cytometry analysis of intracellularly stained Myh9 confirmed the similar downregulation of Myh9 in *Myh9-cHet* and *Myh9-KD* compared to *control* dHoxb8 cells. Furthermore, evaluation of the histograms revealed a homogeneous expression of Myh9 within dHoxb8 cells of all three genotypes, excluding heterogeneity within the single Hoxb8-SCF cell population.

To gain further insight into the underlying genetic processes leading to this unexpected Myh9 expression in *Myh9-KD* dHoxb8-SCF cells, two genotyping PCR strategies were applied. These demonstrated that in *Myh9-cHet* Hoxb8-SCF cells the *Myh9^{fl}* allele was deleted in all cells by the Cre recombinase under the Vav promotor, as expected for hematopoietic cells. Strikingly, *Myh9-KD* Hoxb8-SCF cells deleted one *Myh9^{fl}* allele, yet kept the other *Myh9^{fl}* allele. These observations manifested the theory that the high selection pressure to successfully perform cell division, during establishment of the cell line and differentiation towards PMN, favoured cells with a less active Cre recombinase resulting in *Myh9-KD* Hoxb8-SCF cells with a heterozygous phenotype instead of a knock-out of Myh9. However, expression of Ly6G, CXCR2 and CD11b was assessed by flow cytometry and confirmed the similar maturity of *Myh9-cHet*, *Myh9-KD* and *control* dHoxb8 cells.

Analysis of migration behaviour revealed that *Myh9-KD* dHoxb8 cells had impaired migration with reduced migration velocity as well as diminished Euclidean distance, on rmICAM-1 coated 2D surfaces and in 3D collagen networks, compared to *control* dHoxb8 cells. These results were in line with the findings for *Myh9-cHet* and *control* PMN. Importantly, the expression of an EGFP-tagged Myh9 fusion protein in the *Myh9-KD* Hoxb8-SCF cells (*Myh9-RES* Hoxb8-SCF cells) rescued the migratory defects in 2D and 3D environment. These results indicated that the observed migration defects in Myh9-cHet PMN and dHoxb8 cells was specifically caused by a decreased Myh9 expression.

Using live-cell imaging of *Myh9-RES* dHoxb8 cells migrating in 3D environment, Myh9-EGFP was observed to be enriched at the uropod of fast migrating cells and

accumulated in branching lamellipodia. In previous studies, Myh9 was found to be of importance to maintain membrane tension but negligible for the formations of protrusions[87,177]. Hence, it seems likely that Myh9 enrichment facilitates membrane retraction. This concept corresponds well to the present and previous studies observing elongated tails and multiple pseudopods upon blebbistatin treatment during 2D migration, demonstrating the lack of Myh9 function in these regions[93,94,178]. For chemotactic 3D migration this study proposed a model in which PMN employ Myh9-dependent membrane retraction to enable fast migration by retraction of their uropod, and also to retract branching lamellipodia[180]. During orientation towards a chemoattractant movement of PMN in this direction is promoted by the accumulation of Myh9 in one branching lamellipodium and subsequent retraction of the branching lamellipodium to consolidate the leading edge in the direction of the chemoattractant.

Together with the Myh9-downregulation-dependent displacement of the acto-myosin network out of the lamellipodium to the rear of the cell, as confirmed by the randomisation approach, this concept can also be applied to explain the slow migrating phenotype of PMN with diminished Myh9 expression. The concentration of the remaining Myh9 at the back of the cell could prevent the uropod retraction defect and the diminished F-actin in the lamellipodium possibly hampers promotion of forward protrusions resulting in an overall reduced migration velocity[180].

This present study demonstrates the generic importance of Myh9 for PMN migration. A remaining Myh9 expression of less than 30% was not sufficient for murine bone marrow-derived PMN to perform proper migration in 2D or 3D environment or to transmigrate. Investigations of the underlying mechanisms revealed that maintenance of proper F-actin dynamics in the front of the migrating cell required a certain threshold amount of Myh9. The defect in extravasation was also observed in a model of laser-induced sterile injury in the ear and in a rmCXCL1-induced peritonitis using *Myh9-cHet* and *control* mice, indicating the relevance of Myh9 *in vivo*. Bone marrow chimeric mice confirmed the cell-intrinsic migration defect of PMN with reduced Myh9. Rescuing Myh9 expression enabled *Myh9-RES* dHoxb8 cells to increase their migration velocity and Euclidean distance to control levels[180]. Taken together, this study proved that the non-muscle myosin heavy chain Myh9 is essential for PMN migration during acute inflammation.

5 References

1. Hunter J. A treatise on the blood, inflammation, and gun-shot wounds. London: J. Richardson for G. Nicol; 1794.
2. Turk JL. Inflammation: John Hunter's "A treatise on the blood, inflammation and gun-shot wounds". Int J Exp Pathol 1994;75:385-95.
3. Walzog B, Gaehtgens P. Adhesion Molecules: The Path to a New Understanding of Acute Inflammation. News Physiol Sci 2000;15:107-13.
4. Nathan C. Points of control in inflammation. Nature 2002;420:846-52.
5. Glenn EM, Bowman BJ, Koslowske TC. The systemic response to inflammation. Biochem Pharmacol 1968:Suppl:27-49.
6. Ryan GB, Majno G. Acute inflammation. A review. Am J Pathol 1977;86:183-276.
7. Kolaczkowska E, Kubes P. Neutrophil recruitment and function in health and inflammation. Nat Rev Immunol 2013;13:159-75.
8. Ley K, Laudanna C, Cybulsky MI, Nourshargh S. Getting to the site of inflammation: the leukocyte adhesion cascade updated. Nat Rev Immunol 2007;7:678-89.
9. Nourshargh S, Alon R. Leukocyte migration into inflamed tissues. Immunity 2014;41:694-707.
10. Metschnikow E. Lectures on the comparative pathology of inflammation : delivered at the Pasteur Institute in 1891. London: Kegan Paul, Trench, Trübner & Co.,LTD.; 1893.
11. Metschnikow E. Immunity in infectious diseases. Cambridge: Cambridge University Press Warehouse; 1905.
12. Pillay J, den Braber I, Vrisekoop N, Kwast LM, de Boer RJ, Borghans JA, Tesselaar K, Koenderman L. In vivo labeling with 2H2O reveals a human neutrophil lifespan of 5.4 days. Blood 2010;116:625-7.
13. Basu S, Hodgson G, Katz M, Dunn AR. Evaluation of role of G-CSF in the production, survival, and release of neutrophils from bone marrow into circulation. Blood 2002;100:854-61.
14. Saverymuttu SH, Peters AM, Keshavarzian A, Reavy HJ, Lavender JP. The kinetics of 111indium distribution following injection of 111indium labelled autologous granulocytes in man. Br J Haematol 1985;61:675-85.
15. McCracken JM, Allen LAH. Regulation of Human Neutrophil Apoptosis and Lifespan in Health and Disease. J Cell Death 2014;7:15-23.
16. Casanova-Acebes M, Nicolas-Avila JA, Li JL, Garcia-Silva S, Balachander A, Rubio-Ponce A, Weiss LA, Adrover JM, Burrows K, N AG, Ballesteros I, Devi S, Quintana JA, Crainiciuc G, Leiva M, Gunzer M, Weber C, Nagasawa T, Soehnlein O, Merad M, Mortha A, Ng LG, Peinado H, Hidalgo A. Neutrophils instruct homeostatic and pathological states in naive tissues. J Exp Med 2018;215:2778-95.
17. Adrover JM, Del Fresno C, Crainiciuc G, Cuartero MI, Casanova-Acebes M, Weiss LA, Huerga-Encabo H, Silvestre-Roig C, Rossaint J, Cossio I, Lechuga-Vieco AV, Garcia-Prieto J, Gomez-Parrizas M, Quintana JA, Ballesteros I, Martin-Salamanca S, Aroca-Crevillen A, Chong SZ, Evrard M, Balabanian K, Lopez J, Bidzhekov K, Bachelerie F, Abad-Santos F, Munoz-Calleja C, Zarbock A, Soehnlein O, Weber C, Ng LG, Lopez-Rodriguez C, Sancho D,

Moro MA, Ibanez B, Hidalgo A. A Neutrophil Timer Coordinates Immune Defense and Vascular Protection. Immunity 2019;50:390-402.e10.

18. Tang D, Kang R, Coyne CB, Zeh HJ, Lotze MT. PAMPs and DAMPs: signal 0s that spur autophagy and immunity. Immunol Rev 2012;249:158-75.
19. Medzhitov R, Preston-Hurlburt P, Janeway CA, Jr. A human homologue of the Drosophila Toll protein signals activation of adaptive immunity. Nature 1997;388:394-7.
20. Shi Y, Evans JE, Rock KL. Molecular identification of a danger signal that alerts the immune system to dying cells. Nature 2003;425:516-21.
21. Williams MR, Azcutia V, Newton G, Alcaide P, Luscinskas FW. Emerging mechanisms of neutrophil recruitment across endothelium. Trends Immunol 2011;32:461-9.
22. Nauseef WM, Borregaard N. Neutrophils at work. Nat Immunol 2014;15:602-11.
23. Slowik MR, De Luca LG, Fiers W, Pober JS. Tumor necrosis factor activates human endothelial cells through the p55 tumor necrosis factor receptor but the p75 receptor contributes to activation at low tumor necrosis factor concentration. Am J Pathol 1993;143:1724-30.
24. Bevilacqua MP, Pober JS, Wheeler ME, Cotran RS, Gimbrone MA, Jr. Interleukin 1 acts on cultured human vascular endothelium to increase the adhesion of polymorphonuclear leukocytes, monocytes, and related leukocyte cell lines. J Clin Invest 1985;76:2003-11.
25. Mackay F, Loetscher H, Stueber D, Gehr G, Lesslauer W. Tumor necrosis factor alpha (TNF-alpha)-induced cell adhesion to human endothelial cells is under dominant control of one TNF receptor type, TNF-R55. J Exp Med 1993;177:1277-86.
26. Kienle K, Lammermann T. Neutrophil swarming: an essential process of the neutrophil tissue response. Immunol Rev 2016;273:76-93.
27. Lammermann T, Afonso PV, Angermann BR, Wang JM, Kastenmuller W, Parent CA, Germain RN. Neutrophil swarms require LTB4 and integrins at sites of cell death in vivo. Nature 2013;498:371-5.
28. Barzilai S, Yadav SK, Morrell S, Roncato F, Klein E, Stoler-Barak L, Golani O, Feigelson SW, Zemel A, Nourshargh S, Alon R. Leukocytes Breach Endothelial Barriers by Insertion of Nuclear Lobes and Disassembly of Endothelial Actin Filaments. Cell Rep 2017;18:685-99.
29. Segal AW, Dorling J, Coade S. Kinetics of fusion of the cytoplasmic granules with phagocytic vacuoles in human polymorphonuclear leukocytes. Biochemical and morphological studies. J Cell Biol 1980;85:42-59.
30. Segal AW, Geisow M, Garcia R, Harper A, Miller R. The respiratory burst of phagocytic cells is associated with a rise in vacuolar pH. Nature 1981;290:406-9.
31. Lee WL, Harrison RE, Grinstein S. Phagocytosis by neutrophils. Microbes Infect 2003;5:1299-306.
32. Rada BK, Geiszt M, Kaldi K, Timar C, Ligeti E. Dual role of phagocytic NADPH oxidase in bacterial killing. Blood 2004;104:2947-53.
33. Borregaard N, Sorensen OE, Theilgaard-Monch K. Neutrophil granules: a library of innate immunity proteins. Trends Immunol 2007;28:340-5.
34. Faurschou M, Borregaard N. Neutrophil granules and secretory vesicles in inflammation. Microbes Infect 2003;5:1317-27.

35. Brinkmann V, Reichard U, Goosmann C, Fauler B, Uhlemann Y, Weiss DS, Weinrauch Y, Zychlinsky A. Neutrophil extracellular traps kill bacteria. Science 2004;303:1532-5.

36. Brinkmann V. Neutrophil Extracellular Traps in the Second Decade. J Innate Immun 2018:1-8.

37. Kubes P. The enigmatic neutrophil: what we do not know. Cell Tissue Res 2018;371:399-406.

38. Wang J, Hossain M, Thanabalasuriar A, Gunzer M, Meininger C, Kubes P. Visualizing the function and fate of neutrophils in sterile injury and repair. Science 2017;358:111-6.

39. Schiwon M, Weisheit C, Franken L, Gutweiler S, Dixit A, Meyer-Schwesinger C, Pohl JM, Maurice NJ, Thiebes S, Lorenz K, Quast T, Fuhrmann M, Baumgarten G, Lohse MJ, Opdenakker G, Bernhagen J, Bucala R, Panzer U, Kolanus W, Grone HJ, Garbi N, Kastenmuller W, Knolle PA, Kurts C, Engel DR. Crosstalk between sentinel and helper macrophages permits neutrophil migration into infected uroepithelium. Cell 2014;156:456-68.

40. Nourshargh S, Renshaw SA, Imhof BA. Reverse Migration of Neutrophils: Where, When, How, and Why? Trends Immunol 2016;37:273-86.

41. Leliefeld PH, Koenderman L, Pillay J. How Neutrophils Shape Adaptive Immune Responses. Front Immunol 2015;6:471.

42. Soehnlein O, Lindbom L, Weber C. Mechanisms underlying neutrophil-mediated monocyte recruitment. Blood 2009;114:4613-23.

43. Bennouna S, Bliss SK, Curiel TJ, Denkers EY. Cross-talk in the innate immune system: neutrophils instruct recruitment and activation of dendritic cells during microbial infection. J Immunol 2003;171:6052-8.

44. Kalyan S, Kabelitz D. When neutrophils meet T cells: beginnings of a tumultuous relationship with underappreciated potential. Eur J Immunol 2014;44:627-33.

45. Slaba I, Wang J, Kolaczkowska E, McDonald B, Lee WY, Kubes P. Imaging the dynamic platelet-neutrophil response in sterile liver injury and repair in mice. Hepatology 2015;62:1593-605.

46. Mocsai A, Walzog B, Lowell CA. Intracellular signalling during neutrophil recruitment. Cardiovasc Res 2015;107:373-85.

47. Schymeinsky J, Sperandio M, Walzog B. The mammalian actin-binding protein 1 (mAbp1): a novel molecular player in leukocyte biology. Trends Cell Biol 2011;21:247-55.

48. McEver RP. Selectins: initiators of leucocyte adhesion and signalling at the vascular wall. Cardiovasc Res 2015;107:331-9.

49. Moore KL, Stults NL, Diaz S, Smith DF, Cummings RD, Varki A, McEver RP. Identification of a specific glycoprotein ligand for P-selectin (CD62) on myeloid cells. J Cell Biol 1992;118:445-56.

50. Jung U, Norman KE, Scharffetter-Kochanek K, Beaudet AL, Ley K. Transit time of leukocytes rolling through venules controls cytokine-induced inflammatory cell recruitment in vivo. J Clin Invest 1998;102:1526-33.

51. Ley K. The role of selectins in inflammation and disease. Trends Mol Med 2003;9:263-8.

52. Vestweber D, Blanks JE. Mechanisms that regulate the function of the selectins and their ligands. Physiol Rev 1999;79:181-213.

53. Gotsch U, Jager U, Dominis M, Vestweber D. Expression of P-selectin on endothelial cells is upregulated by LPS and TNF-alpha in vivo. Cell Adhes Commun 1994;2:7-14.

54. Chesnutt BC, Smith DF, Raffler NA, Smith ML, White EJ, Ley K. Induction of LFA-1-dependent neutrophil rolling on ICAM-1 by engagement of E-selectin. Microcirculation 2006;13:99-109.

55. Sigal A, Bleijs DA, Grabovsky V, van Vliet SJ, Dwir O, Figdor CG, van Kooyk Y, Alon R. The LFA-1 integrin supports rolling adhesions on ICAM-1 under physiological shear flow in a permissive cellular environment. J Immunol 2000;165:442-52.

56. Salas A, Shimaoka M, Kogan AN, Harwood C, von Andrian UH, Springer TA. Rolling adhesion through an extended conformation of integrin alphaLbeta2 and relation to alpha I and beta I-like domain interaction. Immunity 2004;20:393-406.

57. Zarbock A, Abram CL, Hundt M, Altman A, Lowell CA, Ley K. PSGL-1 engagement by E-selectin signals through Src kinase Fgr and ITAM adapters DAP12 and FcR gamma to induce slow leukocyte rolling. J Exp Med 2008;205:2339-47.

58. Kuwano Y, Spelten O, Zhang H, Ley K, Zarbock A. Rolling on E- or P-selectin induces the extended but not high-affinity conformation of LFA-1 in neutrophils. Blood 2010;116:617-24.

59. Lefort CT, Ley K. Neutrophil arrest by LFA-1 activation. Front Immunol 2012;3:157.

60. Nishida N, Xie C, Shimaoka M, Cheng Y, Walz T, Springer TA. Activation of leukocyte beta2 integrins by conversion from bent to extended conformations. Immunity 2006;25:583-94.

61. Luo BH, Carman CV, Springer TA. Structural basis of integrin regulation and signaling. Annu Rev Immunol 2007;25:619-47.

62. Li YF, Tang RH, Puan KJ, Law SK, Tan SM. The cytosolic protein talin induces an intermediate affinity integrin alphaLbeta2. J Biol Chem 2007;282:24310-9.

63. Lefort CT, Rossaint J, Moser M, Petrich BG, Zarbock A, Monkley SJ, Critchley DR, Ginsberg MH, Fassler R, Ley K. Distinct roles for talin-1 and kindlin-3 in LFA-1 extension and affinity regulation. Blood 2012;119:4275-82.

64. Moser M, Bauer M, Schmid S, Ruppert R, Schmidt S, Sixt M, Wang HV, Sperandio M, Fassler R. Kindlin-3 is required for beta2 integrin-mediated leukocyte adhesion to endothelial cells. Nat Med 2009;15:300-5.

65. Fan Z, McArdle S, Marki A, Mikulski Z, Gutierrez E, Engelhardt B, Deutsch U, Ginsberg M, Groisman A, Ley K. Neutrophil recruitment limited by high-affinity bent beta2 integrin binding ligand in cis. Nat Commun 2016;7:12658.

66. Herter J, Zarbock A. Integrin Regulation during Leukocyte Recruitment. J Immunol 2013;190:4451-7.

67. Phillipson M, Heit B, Colarusso P, Liu L, Ballantyne CM, Kubes P. Intraluminal crawling of neutrophils to emigration sites: a molecularly distinct process from adhesion in the recruitment cascade. J Exp Med 2006;203:2569-75.

68. Sumagin R, Prizant H, Lomakina E, Waugh RE, Sarelius IH. LFA-1 and Mac-1 define characteristically different intralumenal crawling and emigration patterns for monocytes and neutrophils in situ. J Immunol 2010;185:7057-66.

69. Nourshargh S, Hordijk PL, Sixt M. Breaching multiple barriers: leukocyte motility through venular walls and the interstitium. Nat Rev Mol Cell Biol 2010;11:366-78.

70. Alon R, van Buul JD. Leukocyte Breaching of Endothelial Barriers: The Actin Link. Trends Immunol 2017;38:606-15.

71. Carman CV, Springer TA. A transmigratory cup in leukocyte diapedesis both through individual vascular endothelial cells and between them. J Cell Biol 2004;167:377-88.

72. Kroon J, Schaefer A, van Rijssel J, Hoogenboezem M, van Alphen F, Hordijk P, Stroes ESG, Stromblad S, van Rheenen J, van Buul JD. Inflammation-Sensitive Myosin-X Functionally Supports Leukocyte Extravasation by Cdc42-Mediated ICAM-1-Rich Endothelial Filopodia Formation. J Immunol 2018;200:1790-801.

73. Kenne E, Soehnlein O, Genove G, Rotzius P, Eriksson EE, Lindbom L. Immune cell recruitment to inflammatory loci is impaired in mice deficient in basement membrane protein laminin alpha4. J Leukoc Biol 2010;88:523-8.

74. Hallmann R, Zhang X, Di Russo J, Li L, Song J, Hannocks MJ, Sorokin L. The regulation of immune cell trafficking by the extracellular matrix. Curr Opin Cell Biol 2015;36:54-61.

75. Proebstl D, Voisin MB, Woodfin A, Whiteford J, D'Acquisto F, Jones GE, Rowe D, Nourshargh S. Pericytes support neutrophil subendothelial cell crawling and breaching of venular walls in vivo. J Exp Med 2012;209:1219-34.

76. Armulik A, Abramsson A, Betsholtz C. Endothelial/pericyte interactions. Circ Res 2005;97:512-23.

77. Lammermann T, Germain RN. The multiple faces of leukocyte interstitial migration. Semin Immunopathol 2014;36:227-51.

78. Lerchenberger M, Uhl B, Stark K, Zuchtriegel G, Eckart A, Miller M, Puhr-Westerheide D, Praetner M, Rehberg M, Khandoga AG, Lauber K, Massberg S, Krombach F, Reichel CA. Matrix metalloproteinases modulate ameboid-like migration of neutrophils through inflamed interstitial tissue. Blood 2013;122:770-80.

79. Lam PY, Huttenlocher A. Interstitial leukocyte migration in vivo. Curr Opin Cell Biol 2013;25:650-8.

80. Anderson DC, Schmalsteig FC, Finegold MJ, Hughes BJ, Rothlein R, Miller LJ, Kohl S, Tosi MF, Jacobs RL, Waldrop TC, et al. The severe and moderate phenotypes of heritable Mac-1, LFA-1 deficiency: their quantitative definition and relation to leukocyte dysfunction and clinical features. J Infect Dis 1985;152:668-89.

81. Phillips ML, Schwartz BR, Etzioni A, Bayer R, Ochs HD, Paulson JC, Harlan JM. Neutrophil adhesion in leukocyte adhesion deficiency syndrome type 2. J Clin Invest 1995;96:2898-906.

82. Svensson L, Howarth K, McDowall A, Patzak I, Evans R, Ussar S, Moser M, Metin A, Fried M, Tomlinson I, Hogg N. Leukocyte adhesion deficiency-III is caused by mutations in KINDLIN3 affecting integrin activation. Nat Med 2009;15:306-12.

83. Pai SY, Kim C, Williams DA. Rac GTPases in human diseases. Dis Markers 2010;29:177-87.

84. Vorotnikov AV, Tyurin-Kuzmin PA. Chemotactic signaling in mesenchymal cells compared to amoeboid cells. Genes & Diseases 2014;1:162-73.

85. Pankova K, Rosel D, Novotny M, Brabek J. The molecular mechanisms of transition between mesenchymal and amoeboid invasiveness in tumor cells. Cell Mol Life Sci 2010;67:63-71.

86. Talkenberger K, Cavalcanti-Adam EA, Voss-Bohme A, Deutsch A. Amoeboid-mesenchymal migration plasticity promotes invasion only in complex heterogeneous microenvironments. Sci Rep 2017;7:9237.

87. Lammermann T, Bader BL, Monkley SJ, Worbs T, Wedlich-Soldner R, Hirsch K, Keller M, Forster R, Critchley DR, Fassler R, Sixt M. Rapid leukocyte migration by integrin-independent flowing and squeezing. Nature 2008;453:51-5.

88. Renkawitz J, Schumann K, Weber M, Lammermann T, Pflicke H, Piel M, Polleux J, Spatz JP, Sixt M. Adaptive force transmission in amoeboid cell migration. Nat Cell Biol 2009;11:1438-43.

89. Gambardella L, Vermeren S. Molecular players in neutrophil chemotaxis--focus on PI3K and small GTPases. J Leukoc Biol 2013;94:603-12.

90. Servant G, Weiner OD, Herzmark P, Balla T, Sedat JW, Bourne HR. Polarization of chemoattractant receptor signaling during neutrophil chemotaxis. Science 2000;287:1037-40.

91. Liu L, Gritz D, Parent CA. PKCbetaII acts downstream of chemoattractant receptors and mTORC2 to regulate cAMP production and myosin II activity in neutrophils. Mol Biol Cell 2014;25:1446-57.

92. Pestonjamasp KN, Forster C, Sun C, Gardiner EM, Bohl B, Weiner O, Bokoch GM, Glogauer M. Rac1 links leading edge and uropod events through Rho and myosin activation during chemotaxis. Blood 2006;108:2814-20.

93. Xu J, Wang F, Van Keymeulen A, Herzmark P, Straight A, Kelly K, Takuwa Y, Sugimoto N, Mitchison T, Bourne HR. Divergent signals and cytoskeletal assemblies regulate self-organizing polarity in neutrophils. Cell 2003;114:201-14.

94. Liu X, Yang T, Suzuki K, Tsukita S, Ishii M, Zhou S, Wang G, Cao L, Qian F, Taylor S, Oh MJ, Levitan I, Ye RD, Carnegie GK, Zhao Y, Malik AB, Xu J. Moesin and myosin phosphatase confine neutrophil orientation in a chemotactic gradient. J Exp Med 2015;212:267-80.

95. Li Z, Dong X, Wang Z, Liu W, Deng N, Ding Y, Tang L, Hla T, Zeng R, Li L, Wu D. Regulation of PTEN by Rho small GTPases. Nat Cell Biol 2005;7:399-404.

96. Smith A, Bracke M, Leitinger B, Porter JC, Hogg N. LFA-1-induced T cell migration on ICAM-1 involves regulation of MLCK-mediated attachment and ROCK-dependent detachment. J Cell Sci 2003;116:3123-33.

97. Niggli V. Rho-kinase in human neutrophils: a role in signalling for myosin light chain phosphorylation and cell migration. FEBS Lett 1999;445:69-72.

98. Begandt D, Thome S, Sperandio M, Walzog B. How neutrophils resist shear stress at blood vessel walls: molecular mechanisms, subcellular structures, and cell-cell interactions. J Leukoc Biol 2017.

99. Hyun YM, Sumagin R, Sarangi PP, Lomakina E, Overstreet MG, Baker CM, Fowell DJ, Waugh RE, Sarelius IH, Kim M. Uropod elongation is a common final step in leukocyte extravasation through inflamed vessels. J Exp Med 2012;209:1349-62.

100. Lammermann T, Sixt M. Mechanical modes of 'amoeboid' cell migration. Curr Opin Cell Biol 2009;21:636-44.

101. Ding ZM, Babensee JE, Simon SI, Lu H, Perrard JL, Bullard DC, Dai XY, Bromley SK, Dustin ML, Entman ML, Smith CW, Ballantyne CM. Relative contribution of LFA-1 and Mac-1 to neutrophil adhesion and migration. J Immunol 1999;163:5029-38.

102. Phillipson M, Heit B, Parsons SA, Petri B, Mullaly SC, Colarusso P, Gower RM, Neely G, Simon SI, Kubes P. Vav1 is essential for mechanotactic crawling and migration of neutrophils out of the inflamed microvasculature. J Immunol 2009;182:6870-8.

103. Schymeinsky J, Gerstl R, Mannigel I, Niedung K, Frommhold D, Panthel K, Heesemann J, Sixt M, Quast T, Kolanus W, Mocsai A, Wienands J, Sperandio M, Walzog B. A fundamental

role of mAbp1 in neutrophils: impact on beta(2) integrin-mediated phagocytosis and adhesion in vivo. Blood 2009;114:4209-20.

104. Hepper I, Schymeinsky J, Weckbach LT, Jakob SM, Frommhold D, Sixt M, Laschinger M, Sperandio M, Walzog B. The mammalian actin-binding protein 1 is critical for spreading and intraluminal crawling of neutrophils under flow conditions. J Immunol 2012;188:4590-601.
105. Jakob SM, Pick R, Brechtefeld D, Nussbaum C, Kiefer F, Sperandio M, Walzog B. Hematopoietic progenitor kinase 1 (HPK1) is required for LFA-1-mediated neutrophil recruitment during the acute inflammatory response. Blood 2013;121:4184-94.
106. Fine N, Dimitriou ID, Rullo J, Sandi MJ, Petri B, Haitsma J, Ibrahim H, La Rose J, Glogauer M, Kubes P, Cybulsky M, Rottapel R. GEF-H1 is necessary for neutrophil shear stress-induced migration during inflammation. J Cell Biol 2016;215:107-19.
107. Conti MA, Adelstein RS. Nonmuscle myosin II moves in new directions. J Cell Sci 2008;121:11-8.
108. Lodish H BA, Zipursky SL. Myosin: The Actin Motor Protein. New York: W H Freeman 2000;Molecular Cell Biology. 4th edition
109. Hartman MA, Spudich JA. The myosin superfamily at a glance. J Cell Sci 2012;125:1627-32.
110. Hodge T, Cope MJ. A myosin family tree. J Cell Sci 2000;113 Pt 19:3353-4.
111. Berg JS, Powell BC, Cheney RE. A millennial myosin census. Mol Biol Cell 2001;12:780-94.
112. Foth BJ, Goedecke MC, Soldati D. New insights into myosin evolution and classification. Proc Natl Acad Sci U S A 2006;103:3681-6.
113. Wang A, Ma X, Conti MA, Adelstein RS. Distinct and redundant roles of the non-muscle myosin II isoforms and functional domains. Biochem Soc Trans 2011;39:1131-5.
114. Adelstein RS, Conti MA. Phosphorylation of platelet myosin increases actin-activated myosin ATPase activity. Nature 1975;256:597-8.
115. Amano M, Ito M, Kimura K, Fukata Y, Chihara K, Nakano T, Matsuura Y, Kaibuchi K. Phosphorylation and activation of myosin by Rho-associated kinase (Rho-kinase). J Biol Chem 1996;271:20246-9.
116. Golomb E, Ma X, Jana SS, Preston YA, Kawamoto S, Shoham NG, Goldin E, Conti MA, Sellers JR, Adelstein RS. Identification and characterization of nonmuscle myosin II-C, a new member of the myosin II family. J Biol Chem 2004;279:2800-8.
117. Vicente-Manzanares M, Ma X, Adelstein RS, Horwitz AR. Non-muscle myosin II takes centre stage in cell adhesion and migration. Nat Rev Mol Cell Biol 2009;10:778-90.
118. Vicente-Manzanares M, Zareno J, Whitmore L, Choi CK, Horwitz AF. Regulation of protrusion, adhesion dynamics, and polarity by myosins IIA and IIB in migrating cells. J Cell Biol 2007;176:573-80.
119. Dulyaninova NG, Bresnick AR. The heavy chain has its day: regulation of myosin-II assembly. Bioarchitecture 2013;3:77-85.
120. Sellers JR. Myosins: a diverse superfamily. Biochim Biophys Acta 2000;1496:3-22.
121. Billington N, Wang A, Mao J, Adelstein RS, Sellers JR. Characterization of three full-length human nonmuscle myosin II paralogs. J Biol Chem 2013;288:33398-410.
122. Beach JR, Shao L, Remmert K, Li D, Betzig E, Hammer JA, 3rd. Nonmuscle myosin II isoforms coassemble in living cells. Curr Biol 2014;24:1160-6.

123. Ma X, Jana SS, Conti MA, Kawamoto S, Claycomb WC, Adelstein RS. Ablation of nonmuscle myosin II-B and II-C reveals a role for nonmuscle myosin II in cardiac myocyte karyokinesis. Mol Biol Cell 2010;21:3952-62.

124. Ma X, Adelstein RS. The role of vertebrate nonmuscle Myosin II in development and human disease. Bioarchitecture 2014;4:88-102.

125. Maupin P, Phillips CL, Adelstein RS, Pollard TD. Differential localization of myosin-II isozymes in human cultured cells and blood cells. J Cell Sci 1994;107 (Pt 11):3077-90.

126. Conti MA, Even-Ram S, Liu C, Yamada KM, Adelstein RS. Defects in cell adhesion and the visceral endoderm following ablation of nonmuscle myosin heavy chain II-A in mice. J Biol Chem 2004;279:41263-6.

127. Tullio AN, Accili D, Ferrans VJ, Yu ZX, Takeda K, Grinberg A, Westphal H, Preston YA, Adelstein RS. Nonmuscle myosin II-B is required for normal development of the mouse heart. Proc Natl Acad Sci U S A 1997;94:12407-12.

128. Tai-Nagara I, Yoshikawa Y, Numata N, Ando T, Okabe K, Sugiura Y, Ieda M, Takakura N, Nakagawa O, Zhou B, Okabayashi K, Suematsu M, Kitagawa Y, Bastmeyer M, Sato K, Klein R, Navankasattusas S, Li DY, Yamagishi S, Kubota Y. Placental labyrinth formation in mice requires endothelial FLRT2/UNC5B signaling. Development 2017;144:2392-401.

129. Takeda K, Kishi H, Ma X, Yu ZX, Adelstein RS. Ablation and mutation of nonmuscle myosin heavy chain II-B results in a defect in cardiac myocyte cytokinesis. Circ Res 2003;93:330-7.

130. Ma X, Kawamoto S, Hara Y, Adelstein RS. A point mutation in the motor domain of nonmuscle myosin II-B impairs migration of distinct groups of neurons. Mol Biol Cell 2004;15:2568-79.

131. Bao J, Ma X, Liu C, Adelstein RS. Replacement of nonmuscle myosin II-B with II-A rescues brain but not cardiac defects in mice. J Biol Chem 2007;282:22102-11.

132. Ma X, Bao J, Adelstein RS. Loss of cell adhesion causes hydrocephalus in nonmuscle myosin II-B-ablated and mutated mice. Mol Biol Cell 2007;18:2305-12.

133. Ma X, Kovacs M, Conti MA, Wang A, Zhang Y, Sellers JR, Adelstein RS. Nonmuscle myosin II exerts tension but does not translocate actin in vertebrate cytokinesis. Proc Natl Acad Sci U S A 2012;109:4509-14.

134. Betapudi V. Life without double-headed non-muscle myosin II motor proteins. Front Chem 2014;2:45.

135. Sandquist JC, Swenson KI, Demali KA, Burridge K, Means AR. Rho kinase differentially regulates phosphorylation of nonmuscle myosin II isoforms A and B during cell rounding and migration. J Biol Chem 2006;281:35873-83.

136. Sandquist JC, Means AR. The C-terminal tail region of nonmuscle myosin II directs isoform-specific distribution in migrating cells. Mol Biol Cell 2008;19:5156-67.

137. Betapudi V. Myosin II motor proteins with different functions determine the fate of lamellipodia extension during cell spreading. PLoS One 2010;5:e8560.

138. Even-Ram S, Doyle AD, Conti MA, Matsumoto K, Adelstein RS, Yamada KM. Myosin IIA regulates cell motility and actomyosin-microtubule crosstalk. Nat Cell Biol 2007;9:299-309.

139. Kolega J. Cytoplasmic dynamics of myosin IIA and IIB: spatial 'sorting' of isoforms in locomoting cells. J Cell Sci 1998;111 (Pt 15):2085-95.

140. Kolega J. The role of myosin II motor activity in distributing myosin asymmetrically and coupling protrusive activity to cell translocation. Mol Biol Cell 2006;17:4435-45.

141. Cai Y, Biais N, Giannone G, Tanase M, Jiang G, Hofman JM, Wiggins CH, Silberzan P, Buguin A, Ladoux B, Sheetz MP. Nonmuscle myosin IIA-dependent force inhibits cell spreading and drives F-actin flow. Biophys J 2006;91:3907-20.

142. Bao J, Jana SS, Adelstein RS. Vertebrate nonmuscle myosin II isoforms rescue small interfering RNA-induced defects in COS-7 cell cytokinesis. J Biol Chem 2005;280:19594-9.

143. Roy A, Lordier L, Mazzi S, Chang Y, Lapierre V, Larghero J, Debili N, Raslova H, Vainchenker W. Activity of nonmuscle myosin II isoforms determines localization at the cleavage furrow of megakaryocytes. Blood 2016;128:3137-45.

144. Shin JW, Buxboim A, Spinler KR, Swift J, Christian DA, Hunter CA, Leon C, Gachet C, Dingal PC, Ivanovska IL, Rehfeldt F, Chasis JA, Discher DE. Contractile forces sustain and polarize hematopoiesis from stem and progenitor cells. Cell Stem Cell 2014;14:81-93.

145. Maravillas-Montero JL, Santos-Argumedo L. The myosin family: unconventional roles of actin-dependent molecular motors in immune cells. J Leukoc Biol 2012;91:35-46.

146. Stroka KM, Hayenga HN, Aranda-Espinoza H. Human neutrophil cytoskeletal dynamics and contractility actively contribute to trans-endothelial migration. PLoS One 2013;8:e61377.

147. Bertram A, Ley K. Protein kinase C isoforms in neutrophil adhesion and activation. Arch Immunol Ther Exp (Warsz) 2011;59:79-87.

148. Matsumura F, Hartshorne DJ. Myosin phosphatase target subunit: Many roles in cell function. Biochem Biophys Res Commun 2008;369:149-56.

149. Komatsu S, Ikebe M. The phosphorylation of myosin II at the Ser1 and Ser2 is critical for normal platelet-derived growth factor induced reorganization of myosin filaments. Mol Biol Cell 2007;18:5081-90.

150. Kawamoto S, Bengur AR, Sellers JR, Adelstein RS. In situ phosphorylation of human platelet myosin heavy and light chains by protein kinase C. J Biol Chem 1989;264:2258-65.

151. Moussavi RS, Kelley CA, Adelstein RS. Phosphorylation of vertebrate nonmuscle and smooth muscle myosin heavy chains and light chains. Mol Cell Biochem 1993;127-128:219-27.

152. Clark K, Middelbeek J, Lasonder E, Dulyaninova NG, Morrice NA, Ryazanov AG, Bresnick AR, Figdor CG, van Leeuwen FN. TRPM7 regulates myosin IIA filament stability and protein localization by heavy chain phosphorylation. J Mol Biol 2008;378:790-803.

153. Sanborn KB, Mace EM, Rak GD, Difeo A, Martignetti JA, Pecci A, Bussel JB, Favier R, Orange JS. Phosphorylation of the myosin IIA tailpiece regulates single myosin IIA molecule association with lytic granules to promote NK-cell cytotoxicity. Blood 2011;118:5862-71.

154. Ludowyke RI, Elgundi Z, Kranenburg T, Stehn JR, Schmitz-Peiffer C, Hughes WE, Biden TJ. Phosphorylation of nonmuscle myosin heavy chain IIA on Ser1917 is mediated by protein kinase C beta II and coincides with the onset of stimulated degranulation of RBL-2H3 mast cells. J Immunol 2006;177:1492-9.

155. Pasapera AM, Plotnikov SV, Fischer RS, Case LB, Egelhoff TT, Waterman CM. Rac1-dependent phosphorylation and focal adhesion recruitment of myosin IIA regulates migration and mechanosensing. Curr Biol 2015;25:175-86.

156. Betapudi V, Gokulrangan G, Chance MR, Egelhoff TT. A proteomic study of myosin II motor proteins during tumor cell migration. J Mol Biol 2011;407:673-86.

157. Dulyaninova NG, House RP, Betapudi V, Bresnick AR. Myosin-IIA heavy-chain phosphorylation regulates the motility of MDA-MB-231 carcinoma cells. Mol Biol Cell 2007;18:3144-55.

158. Jacobelli J, Estin Matthews M, Chen S, Krummel MF. Activated T cell trans-endothelial migration relies on myosin-IIA contractility for squeezing the cell nucleus through endothelial cell barriers. PLoS One 2013;8:e75151.

159. Jacobelli J, Friedman RS, Conti MA, Lennon-Dumenil AM, Piel M, Sorensen CM, Adelstein RS, Krummel MF. Confinement-optimized three-dimensional T cell amoeboid motility is modulated via myosin IIA-regulated adhesions. Nat Immunol 2010;11:953-61.

160. Jacobelli J, Bennett FC, Pandurangi P, Tooley AJ, Krummel MF. Myosin-IIA and ICAM-1 regulate the interchange between two distinct modes of T cell migration. J Immunol 2009;182:2041-50.

161. Rey M, Vicente-Manzanares M, Viedma F, Yanez-Mo M, Urzainqui A, Barreiro O, Vazquez J, Sanchez-Madrid F. Cutting edge: association of the motor protein nonmuscle myosin heavy chain-IIA with the C terminus of the chemokine receptor CXCR4 in T lymphocytes. J Immunol 2002;169:5410-4.

162. Morin NA, Oakes PW, Hyun YM, Lee D, Chin YE, King MR, Springer TA, Shimaoka M, Tang JX, Reichner JS, Kim M. Nonmuscle myosin heavy chain IIA mediates integrin LFA-1 de-adhesion during T lymphocyte migration. J Exp Med 2008;205:195-205.

163. Gomez TS, Billadeau DD. T cell activation and the cytoskeleton: you can't have one without the other. Adv Immunol 2008;97:1-64.

164. Ilani T, Vasiliver-Shamis G, Vardhana S, Bretscher A, Dustin ML. T cell antigen receptor signaling and immunological synapse stability require myosin IIA. Nat Immunol 2009;10:531-9.

165. Jacobelli J, Chmura SA, Buxton DB, Davis MM, Krummel MF. A single class II myosin modulates T cell motility and stopping, but not synapse formation. Nat Immunol 2004;5:531-8.

166. Chabaud M, Heuze ML, Bretou M, Vargas P, Maiuri P, Solanes P, Maurin M, Terriac E, Le Berre M, Lankar D, Piolot T, Adelstein RS, Zhang Y, Sixt M, Jacobelli J, Benichou O, Voituriez R, Piel M, Lennon-Dumenil AM. Cell migration and antigen capture are antagonistic processes coupled by myosin II in dendritic cells. Nat Commun 2015;6:7526.

167. Leon C, Eckly A, Hechler B, Aleil B, Freund M, Ravanat C, Jourdain M, Nonne C, Weber J, Tiedt R, Gratacap MP, Severin S, Cazenave JP, Lanza F, Skoda R, Gachet C. Megakaryocyte-restricted MYH9 inactivation dramatically affects hemostasis while preserving platelet aggregation and secretion. Blood 2007;110:3183-91.

168. Gaertner F, Ahmad Z, Rosenberger G, Fan S, Nicolai L, Busch B, Yavuz G, Luckner M, Ishikawa-Ankerhold H, Hennel R, Benechet A, Lorenz M, Chandraratne S, Schubert I, Helmer S, Striednig B, Stark K, Janko M, Bottcher RT, Verschoor A, Leon C, Gachet C, Gudermann T, Mederos YSM, Pincus Z, Iannacone M, Haas R, Wanner G, Lauber K, Sixt M, Massberg S. Migrating Platelets Are Mechano-scavengers that Collect and Bundle Bacteria. Cell 2017;171:1368-82.e23.

169. Vascotto F, Lankar D, Faure-Andre G, Vargas P, Diaz J, Le Roux D, Yuseff MI, Sibarita JB, Boes M, Raposo G, Mougneau E, Glaichenhaus N, Bonnerot C, Manoury B, Lennon-Dumenil AM. The actin-based motor protein myosin II regulates MHC class II trafficking and BCR-driven antigen presentation. J Cell Biol 2007;176:1007-19.

170. Andzelm MM, Chen X, Krzewski K, Orange JS, Strominger JL. Myosin IIA is required for cytolytic granule exocytosis in human NK cells. J Exp Med 2007;204:2285-91.

171. Sanborn KB, Rak GD, Maru SY, Demers K, Difeo A, Martignetti JA, Betts MR, Favier R, Banerjee PP, Orange JS. Myosin IIA associates with NK cell lytic granules to enable their interaction with F-actin and function at the immunological synapse. J Immunol 2009;182:6969-84.

172. Marigo V, Nigro A, Pecci A, Montanaro D, Di Stazio M, Balduini CL, Savoia A. Correlation between the clinical phenotype of MYH9-related disease and tissue distribution of class II nonmuscle myosin heavy chains. Genomics 2004;83:1125-33.

173. Kepiro M, Varkuti BH, Vegner L, Voros G, Hegyi G, Varga M, Malnasi-Csizmadia A. para-Nitroblebbistatin, the non-cytotoxic and photostable myosin II inhibitor. Angew Chem Int Ed Engl 2014;53:8211-5.

174. Kolega J. Phototoxicity and photoinactivation of blebbistatin in UV and visible light. Biochem Biophys Res Commun 2004;320:1020-5.

175. Ostap EM. 2,3-Butanedione monoxime (BDM) as a myosin inhibitor. J Muscle Res Cell Motil 2002;23:305-8.

176. Allingham JS, Smith R, Rayment I. The structural basis of blebbistatin inhibition and specificity for myosin II. Nat Struct Mol Biol 2005;12:378-9.

177. Houk AR, Jilkine A, Mejean CO, Boltyanskiy R, Dufresne ER, Angenent SB, Altschuler SJ, Wu LF, Weiner OD. Membrane tension maintains cell polarity by confining signals to the leading edge during neutrophil migration. Cell 2012;148:175-88.

178. Eddy RJ, Pierini LM, Matsumura F, Maxfield FR. Ca2+-dependent myosin II activation is required for uropod retraction during neutrophil migration. J Cell Sci 2000;113 (Pt 7):1287-98.

179. de Boer J, Williams A, Skavdis G, Harker N, Coles M, Tolaini M, Norton T, Williams K, Roderick K, Potocnik AJ, Kioussis D. Transgenic mice with hematopoietic and lymphoid specific expression of Cre. Eur J Immunol 2003;33:314-25.

180. Zehrer A, Pick R, Salvermoser M, Boda A, Miller M, Stark K, Weckbach LT, Walzog B, Begandt D. A Fundamental Role of Myh9 for Neutrophil Migration in Innate Immunity. J Immunol 2018;201:1748-64.

181. Schymeinsky J, Sindrilaru A, Frommhold D, Sperandio M, Gerstl R, Then C, Mocsai A, Scharffetter-Kochanek K, Walzog B. The Vav binding site of the non-receptor tyrosine kinase Syk at Tyr 348 is critical for beta2 integrin (CD11/CD18)-mediated neutrophil migration. Blood 2006;108:3919-27.

182. Park J, Throop AL, LaBaer J. Site-specific recombinational cloning using gateway and in-fusion cloning schemes. Curr Protoc Mol Biol 2015;110:3.20.1-3.

183. Southgate EL, He RL, Gao JL, Murphy PM, Nanamori M, Ye RD. Identification of formyl peptides from Listeria monocytogenes and Staphylococcus aureus as potent chemoattractants for mouse neutrophils. J Immunol 2008;181:1429-37.

184. Shivanandan A, Radenovic A, Sbalzarini IF. MosaicIA: an ImageJ/Fiji plugin for spatial pattern and interaction analysis. BMC Bioinformatics 2013;14:349.

185. Helmuth JA, Paul G, Sbalzarini IF. Beyond co-localization: inferring spatial interactions between sub-cellular structures from microscopy images. BMC Bioinformatics 2010;11:372.

186. Pick R, Begandt D, Stocker TJ, Salvermoser M, Thome S, Bottcher RT, Montanez E, Harrison U, Forne I, Khandoga AG, Coletti R, Weckbach LT, Brechtefeld D, Haas R, Imhof A, Massberg S, Sperandio M, Walzog B. Coronin 1A, a novel player in integrin biology, controls neutrophil trafficking in innate immunity. Blood 2017;130:847-58.

187. Salvermoser M, Pick R, Weckbach LT, Zehrer A, Lohr P, Drechsler M, Sperandio M, Soehnlein O, Walzog B. Myosin 1f is specifically required for neutrophil migration in 3D environments during acute inflammation. Blood 2018;131:1887-98.

188. Weckbach LT, Gola A, Winkelmann M, Jakob SM, Groesser L, Borgolte J, Pogoda F, Pick R, Pruenster M, Muller-Hocker J, Deindl E, Sperandio M, Walzog B. The cytokine midkine supports neutrophil trafficking during acute inflammation by promoting adhesion via beta2 integrins (CD11/CD18). Blood 2014;123:1887-96.

189. Zigmond SH. Ability of polymorphonuclear leukocytes to orient in gradients of chemotactic factors. J Cell Biol 1977;75:606-16.

190. Kurz AR, Pruenster M, Rohwedder I, Ramadass M, Schafer K, Harrison U, Gouveia G, Nussbaum C, Immler R, Wiessner JR, Margraf A, Lim DS, Walzog B, Dietzel S, Moser M, Klein C, Vestweber D, Haas R, Catz SD, Sperandio M. MST1-dependent vesicle trafficking regulates neutrophil transmigration through the vascular basement membrane. J Clin Invest 2016;126:4125-39.

191. Ng LG, Hsu A, Mandell MA, Roediger B, Hoeller C, Mrass P, Iparraguirre A, Cavanagh LL, Triccas JA, Beverley SM, Scott P, Weninger W. Migratory dermal dendritic cells act as rapid sensors of protozoan parasites. PLoS Pathog 2008;4:e1000222.

192. Stark K, Eckart A, Haidari S, Tirniceriu A, Lorenz M, von Bruhl ML, Gartner F, Khandoga AG, Legate KR, Pless R, Hepper I, Lauber K, Walzog B, Massberg S. Capillary and arteriolar pericytes attract innate leukocytes exiting through venules and 'instruct' them with pattern-recognition and motility programs. Nat Immunol 2013;14:41-51.

193. Khandoga AG, Khandoga A, Reichel CA, Bihari P, Rehberg M, Krombach F. In vivo imaging and quantitative analysis of leukocyte directional migration and polarization in inflamed tissue. PLoS One 2009;4:e4693.

194. Basu S, Ray A, Dittel BN. Differential representation of B cell subsets in mixed bone marrow chimera mice due to expression of allelic variants of CD45 (CD45.1/CD45.2). J Immunol Methods 2013;396:163-7.

195. Koporc Z, Bigenzahn S, Blaha P, Fariborz E, Selzer E, Sykes M, Muehlbacher F, Wekerle T. Induction of mixed chimerism through transplantation of CD45-congenic mobilized peripheral blood stem cells after nonmyeloablative irradiation. Biol Blood Marrow Transplant 2006;12:284-92.

196. Nakayama M, Amano M, Katsumi A, Kaneko T, Kawabata S, Takefuji M, Kaibuchi K. Rho-kinase and myosin II activities are required for cell type and environment specific migration. Genes Cells 2005;10:107-17.

197. Wang GG, Calvo KR, Pasillas MP, Sykes DB, Hacker H, Kamps MP. Quantitative production of macrophages or neutrophils ex vivo using conditional Hoxb8. Nat Methods 2006;3:287-93.

198. Redecke V, Wu R, Zhou J, Finkelstein D, Chaturvedi V, High AA, Hacker H. Hematopoietic progenitor cell lines with myeloid and lymphoid potential. Nat Methods 2013;10:795-803.

199. Huang J, Zhang J, Pathak A, Li J, Stouffer GA. Perivascular delivery of blebbistatin reduces neointimal hyperplasia after carotid injury in the mouse. J Pharmacol Exp Ther 2011;336:116-26.

200. Mortensen M, Ferguson DJ, Edelmann M, Kessler B, Morten KJ, Komatsu M, Simon AK. Loss of autophagy in erythroid cells leads to defective removal of mitochondria and severe anemia in vivo. Proc Natl Acad Sci U S A 2010;107:832-7.

201. Finney BA, Schweighoffer E, Navarro-Nunez L, Benezech C, Barone F, Hughes CE, Langan SA, Lowe KL, Pollitt AY, Mourao-Sa D, Sheardown S, Nash GB, Smithers N, Reis e Sousa C, Tybulewicz VL, Watson SP. CLEC-2 and Syk in the megakaryocytic/platelet lineage are essential for development. Blood 2012;119:1747-56.

202. Klapproth S, Moretti FA, Zeiler M, Ruppert R, Breithaupt U, Mueller S, Haas R, Mann M, Sperandio M, Fassler R, Moser M. Minimal amounts of kindlin-3 suffice for basal platelet and leukocyte functions in mice. Blood 2015;126:2592-600.

203. Valerius NH, Stendahl O, Hartwig JH, Stossel TP. Distribution of actin-binding protein and myosin in polymorphonuclear leukocytes during locomotion and phagocytosis. Cell 1981;24:195-202.

204. Varkuti BH, Kepiro M, Horvath IA, Vegner L, Rati S, Zsigmond A, Hegyi G, Lenkei Z, Varga M, Malnasi-Csizmadia A. A highly soluble, non-phototoxic, non-fluorescent blebbistatin derivative. Sci Rep 2016;6:26141.

205. Kovacs M, Nemeth T, Jakus Z, Sitaru C, Simon E, Futosi K, Botz B, Helyes Z, Lowell CA, Mocsai A. The Src family kinases Hck, Fgr, and Lyn are critical for the generation of the in vivo inflammatory environment without a direct role in leukocyte recruitment. J Exp Med 2014;211:1993-2011.

206. Nemeth T, Virtic O, Sitaru C, Mocsai A. The Syk Tyrosine Kinase Is Required for Skin Inflammation in an In Vivo Mouse Model of Epidermolysis Bullosa Acquisita. J Invest Dermatol 2017;137:2131-9.

207. Shin JW, Swift J, Spinler KR, Discher DE. Myosin-II inhibition and soft 2D matrix maximize multinucleation and cellular projections typical of platelet-producing megakaryocytes. Proc Natl Acad Sci U S A 2011;108:11458-63.

6 Acknowledgements

Completion of this doctoral dissertation was only possible as a result of the support from several people. I would like to express my sincere gratitude to each of them. Firstly, I would like to express my special appreciation and thanks to my advisor Professor Dr. Barbara Walzog. I acknowledge all her contributions of time and advice. Her continuous support of my work made my doctoral experience productive and allowed me to grow as a research scientist.
Also, I would like to thank Prof. Dr. Markus Sperandio and PD. Dr. Markus Moser for serving as my TAC committee members. I highly value their advice and encouraging feedback for my research.

Furthermore, I am grateful to Dr. Robert Pick for his help with spinning disk microscopy and STED nanaoscopy, as well as the fruitful discussions and splendid ideas on advanced analysis methods. My gratitude also goes to Dr. Ludwig Weckbach for his advice regarding animal experiment applications. I also thank my collaborators Dr. Konstantin Stark and especially, Annegred Boda and Dr. Meike Miller, for their advice and commitment in the realisation of the laser-induced injury model and the generation of bone marrow chimeras.

I gratefully acknowledge the SFB 914 for the funding sources that made my doctoral work possible and for providing excellent professional training possibilities. In particular, I want to thank Dr. Tobias Kemme and Dr. Verena Kochan for facilitating organizational matters.

A huge thank-you goes to my fellow lab mates of the Walzog group for their loyalty during these intense times. Their experience, invaluable advice, and motivation helped me through any kind of crisis on the way to completion of this dissertation. I want to particularly thank Dr. Melanie Salvermoser, Ann-Cathrin Werner, Jennifer Truong and Severin Gylsdorff for their unlimited support, on both professional and personal levels.

This phase of my life wouldn’t have been possible without the love and encouragement of my family, whom have supported me in all my pursuits. I am forever thankful to my parents for inspiring me to seek my own direction in life and to make experiences, which have made me who I am. I also appreciate the patience, understanding and help of my local and overseas friends throughout this journey.
Finally, I want to thank Mathias for his unwavering love and faith in me.

7 Appendix

7.1 Affidavit

Zehrer, Annette
……...
Surname, first name

……...
Street

……...
Zip code, town

Germany
……...
Country

I hereby declare, that the submitted thesis entitled

The non-muscle myosin heavy chain Myh9 is essential for neutrophil migration during acute inflammation

is my own work. I have only used the sources indicated and have not made unauthorized use of services of a third party. Where the work of others has been quoted or reproduced, the source is always given.

I further declare that the submitted thesis or parts thereof have not been presented as part of an examination degree to any other university.

Stockdorf, 24.02.2020
Ort, Datum

Annette Zehrer
Unterschrift, Doktorandin

7.2 Publications

Major parts of the present work have been published in *The Journal of Immunology:*

Zehrer A., Pick R., Salvermoser M., Boda A., Miller M., Stark K., Weckbach L., Walzog B., and Begandt D.; A fundamental role of Myh9 for neutrophil migration in innate immunity; J Immunol. 2018 Sep 15;201(6):1748-1764[180].

Additional publications

Weckbach LT., Grabmaier U., Uhl A., Gess S., Boehm F., **Zehrer A.**, Pick R., Salvermoser M., Czermak T., Pircher J., Sorrelle N., Migliorini M., Strickland DK., Klingel K., Brinkmann V., Abu Abed U., Eriksson U., Massberg S., Brunner S, Walzog B.; Midkine drives cardiac inflammation by promoting neutrophil trafficking and NETosis in myocarditis. J Exp Med. 2019 Feb 4;216(2):350-368.

Salvermoser M, Pick R, Weckbach LT, **Zehrer A,** Löhr P, Drechsler M, Sperandio M, Soehnlein O, Walzog B.; Myosin 1f is specifically required for neutrophil migration in 3D environments during acute inflammation. Blood. 2018 Apr 26;131(17):1887-1898.

Lee AYS, Reimer D, **Zehrer A**, Lu M, Mielenz D, Körner H.; Expression of Membrane-Bound CC Chemokine Ligand 20 on Follicular T Helper Cells in T-B-Cell Conjugates. Front Immunol. 2017 Dec 21;8:1871.

Scientific presentations & Conference attendances

03.2018	2nd International Conference on Leukocyte Trafficking, Munich, Germany
10.2017	39th Annual Meeting of the German Society for Microcirculation and Vascular Biology (GfMVB), Grainau/Garmisch, Germany (poster presentation)
09.2016	Scientific Retreat of the SFB 914, Lochau, Austria (poster presentation)
07.2016	Annual Retreat of the IRTG of the SFB 914, Schöntal, Germany (poster presentation)
04.2016	50th Annual Meeting of the European Society for Clinical Investigation (ESCI), Paris, France (oral presentation)
09.2015	Symposium of the SFB 914, Villa Vigoni, Italy (oral and poster presentation)
09.2015	37th Annual Meeting of the German Society for Microcirculation and Vascular Biology (GfMVB), Hannover, Germany (poster presentation)
06.2015	Joint Meeting of the European Society for Microcirculation (ESM) and the

European Vascular Biology Organization (EVBO), Pisa, Italy

11.2014 Annual Retreat of the IRTG of the SFB 914, Günzburg, Germany (oral presentation)